

**Chaotic and Chaotic Based Frequency Modulated
Signals for Radar Imaging**

by

Emmanuel Arturo Solis Nepote

A Thesis

**Submitted to the Faculty of Graduate Studies
In Partial Fulfillment of the Requirements for the Degree of**

Master of Science

**Department of Electrical and Computer Engineering
University of Manitoba
Winnipeg, Manitoba**

© Emmanuel Arturo Solis Nepote, October 2003.

THE UNIVERSITY OF MANITOBA
FACULTY OF GRADUATE STUDIES

COPYRIGHT PERMISSION

**Chaotic and Chaotic Based Frequency Modulated
Signals for Radar Imaging**

BY

Emmanuel Arturo Solis Nepote

**A Thesis/Practicum submitted to the Faculty of Graduate Studies of The University of
Manitoba in partial fulfillment of the requirement of the degree
Of
MASTER OF SCIENCE**

Emmanuel Arturo Solis Nepote © 2003

Permission has been granted to the Library of the University of Manitoba to lend or sell copies of this thesis/practicum, to the National Library of Canada to microfilm this thesis and to lend or sell copies of the film, and to University Microfilms Inc. to publish an abstract of this thesis/practicum.

This reproduction or copy of this thesis has been made available by authority of the copyright owner solely for the purpose of private study and research, and may only be reproduced and copied as permitted by copyright laws or with express written authorization from the copyright owner.

Abstract

This thesis presents an analysis of a chaotic and chaotic-based frequency-modulated signals, and demonstrates the possibility of their use in wideband radar imaging systems. The signals resolution capability and sidelobe distribution on the range-Doppler plane are assessed by the inspection of their ambiguity surface. Four deterministic, bounded, non-linear, iterated maps are considered. Statistically independent samples with invariant probability density function are obtained by randomizing the initial condition of each map. The resulting sequences, which have broadband frequency representations, are also used to construct wideband, stochastic frequency-modulated signals. These chaotic and chaotic-based frequency-modulated signals are ergodic and stationary. The autocorrelation, spectrum, and the ambiguity surface associated with the signals are characterized, as well as their chaotic behaviour using the Lyapunov exponent and correlation dimension. The ambiguity surface of an FM signal generated via a chaotic map with uniform sample distribution is demonstrated to be comparable to the ambiguity function of a random FM signal and superior to that of a linear frequency-modulated chirp. Finally the proposed new radar signals are compared to other traditional waveforms used in radar systems in terms of resolution, electronic counter-countermeasures and multipath performance.

Index Terms— Ambiguity function, chaos, frequency modulation, iterated maps, multipath effect, radar resolution, radar signal analysis, radar signal processing.

Acknowledgements

The author wants to gratefully thank his advisor, Professor Gabriel Thomas, for his encouragement, support and guidance during all the time this research was conducted. In addition, many thanks are given to Professor Benjamin Flores for his criticism and suggestions; without his help this project would have never been completed. Special thanks are also given to Professor Zahra Moussavi for her interest in this thesis; her suggestions and feedback were really important and appreciated by the author.

Table of contents

Abstract	3
Acknowledgments	4
Table of contents	5
List of tables	8
List of figures	9
1. Introduction	12
2. Overview	16
2.1 Radar	16
2.2 Radar signals	19
2.2.1 Linear FM chirp.....	20
2.2.2 Random and noise modulation.....	21
2.3 Ambiguity function	23
2.4 Chaos	26
2.4.1 Chaos in iterated maps.....	27
2.4.2 Lyapunov exponents.....	29
2.4.3 Fractal dimensions.....	32
2.4.3.1 <i>Correlation dimension</i>	33
2.5 Investigated chaotic maps	34
2.5.1 Logistic map.....	35
2.5.2 Bernoulli map.....	37
2.5.3 The tent map.....	38
2.5.4 Quadratic map.....	40

3. Signal analysis.....	42
3.1 Analysis of chaotic signals.....	42
3.1.1 Ergodicity of chaotic signals.....	42
3.1.2 Autocorrelation and power spectrum of chaotic signals.....	44
3.1.3 Chaos quantification.....	46
3.1.3.1 Lyapunov exponent of chaotic signals.....	47
3.1.3.2 Correlation dimension of chaotic signals.....	48
3.2 Analysis of CBFM signals.....	50
3.2.1 Ergodicity of CBFM signals.....	52
3.2.2 Autocorrelation and power spectrum of CBFM signals.....	54
3.2.3 Chaos quantification in CBFM signals.....	60
3.2.3.1 Lyapunov exponent of CBFM signals.....	63
3.2.3.2 Correlation dimension of CBFM signals.....	64
3.3 Analysis of random FM signal.....	65
3.3.1 Autocorrelation and power spectrum of random FM signal.....	65
3.3.2 Chaos quantification in random FM signal.....	67
3.3.2.1 Lyapunov exponent of random FM signal.....	67
3.3.2.2 Correlation dimension of random FM signal.....	68
4. Results and evaluation.....	69
4.1 Ambiguity functions.....	69
4.1.1 Ambiguity function of chaotic signals.....	70
4.1.2 Ambiguity function of CBFM signals.....	71
4.2 Multipath performance of Bernoulli CBFM.....	73
4.3 ECCM and noise performance of Bernoulli CBFM.....	80
4.4 Comparative study against FM chirp and random FM signals.....	85
4.4.1 Ambiguity functions of FM chirp and random FM signal.....	85
4.4.2 Multipath performance of FM chirp and random FM signal.....	88
4.4.3 ECCM and noise performance of FM chirp and random FM signal.....	91
5. Conclusion.....	94

References.....	96
Appendix A (List of acronyms)	101
Appendix B (List of symbols)	102
Appendix C (Matlab© simulations code)	105

List of tables

Table 2.1	Chaotic maps and respective control parameter value.....	35
Table 3.1	Statistical and spectral properties of selected maps.....	46
Table 3.2	Chaos quantification in selected maps.....	48
Table 3.3	Statistical properties of CBFM signals.....	54
Table 3.4	Chaos quantification for CBFM signals.....	64
Table 3.5	Chaos quantification for GFM signals.....	68
Table 4.1	Interference-induced difference percentage for various SNR and distributions in received Bernoulli CBFM signal.....	84
Table 4.2	Interference-induced difference percentage for various distributions in received Bernoulli CBFM, linear FM chirp and Gaussian FM signal.....	92

List of figures

Fig. 2.1	Basic radar system.....	17
Fig. 2.2	Linear frequency modulation pulse compression waveforms.....	21
Fig. 2.3	Basic noise modulated radar system.....	22
Fig. 2.4	Partial bifurcation diagram of chaotic map.....	28
Fig. 2.5	Divergence of close trajectories in chaotic map.....	29
Fig. 2.6	Bifurcation diagram of logistic map.....	36
Fig. 2.7	Chaotic trajectory of logistic map for $D = 4$	36
Fig. 2.8	Bifurcation diagram of Bernoulli map.....	37
Fig. 2.9	Chaotic trajectory of Bernoulli map for $D = 2$	38
Fig. 2.10	Bifurcation diagram of tent map.....	39
Fig. 2.11	Chaotic trajectory of tent map for $D = 2$	39
Fig. 2.12	Bifurcation diagram of quadratic map.....	40
Fig. 2.13	Chaotic trajectory of quadratic map for $D = \frac{1}{2}$	41
Fig. 3.1	Ergodicity in selected chaotic maps.....	43
Fig. 3.2	Averaged autocorrelation of chaotic sequences.....	45
Fig. 3.3	Power spectra of selected chaotic maps.....	46
Fig. 3.4	Pseudo-phase space of chaotic sequences.....	47
Fig. 3.5	Correlation dimension plots for selected chaotic sequences.....	49
Fig. 3.6	CBFM signals.....	52
Fig. 3.7	Ergodicity of CBFM signals.....	53
Fig. 3.8	Averaged autocorrelation of CBFM signals.....	59
Fig. 3.9	Power spectra of CBFM signals.....	60

Fig. 3.10	Two-dimensional pseudo-phase space representation of CBFM signals.....	61
Fig. 3.11	Three-dimensional pseudo-phase space representations of CBFM signals.....	62
Fig. 3.12	Logarithmic plot of the divergence of close trajectories and Lyapunov exponent estimation in Bernoulli based FM signal.....	63
Fig. 3.13	Average autocorrelation of GFM signal.....	66
Fig. 3.14	Calculated power spectral density of GFM signal.....	66
Fig. 3.15	Three-dimensional pseudo-phase space representations of GFM signal.....	67
Fig. 3.16	Correlation dimension plot of GFM.....	68
Fig. 4.1	Ambiguity surfaces of chaotic signals.....	70
Fig. 4.2	Ambiguity surfaces of CBFM signals.....	71
Fig. 4.3	Multipath scenarios.....	73
Fig. 4.4	Performance of Bernoulli CBFM signal in multipath environments	77
Fig. 4.5	Performance of Bernoulli CBFM in multipath environments at several reflection coefficients.....	78
Fig. 4.6	Performance of different bandlimited Bernoulli CBFM signals in multipath environments.....	79
Fig. 4.7	Sample correlation between noise contaminated Bernoulli CBFM and original transmitted signal, compared with autocorrelation of original transmitted signal.....	82
Fig. 4.8	Simulated radar images generated by ideal and noise contaminated Bernoulli CBFM signals.....	83
Fig. 4.9	Interference-induced difference percentage in the received Bernoulli CBFM signal contaminated by Gaussian noise at various SNR.....	84
Fig. 4.10	Contour of the ambiguity surface of a linear chirp.....	86
Fig. 4.11	Ambiguity surface of LFM chirp.....	86

Fig. 4.12	Ambiguity surface of Gaussian FM waveform.....	87
Fig. 4.13	Comparison of Bernoulli CBFM (BFM), linear FM (LFM) and Gaussian FM (GFM) performance in multipath environments.....	88
Fig. 4.14	Comparison of Bernoulli CBFM (BFM), linear FM (LFM) and Gaussian FM (GFM) performance in multipath environment with several reflection coefficients.....	89
Fig. 4.15	Comparison of Bernoulli CBFM (BFM), linear FM (LFM) and Gaussian FM (GFM) performance when bandwidth is reduced.....	90
Fig. 4.16	Interference-induced difference percentage in received waveforms contaminated by Gaussian noise for various SNR.....	93

Chapter 1

Introduction

The work presented in this thesis offers a novel exploration in the area of radar signal design. Historically, the search for new signals that in some way can improve the radar performance has never stopped. Since the introduction of radar systems, developers had tried to come up with new techniques and concepts to improve the performance of these systems. Independently, the field of chaos has had a tremendous explosion during the last hundred years. The exploration of chaos and its comprehension has resulted in many new ideas and has brought new enrichments to numerous applications. Surprisingly, until recently, very little research had been done in order to use the suitable characteristic of chaos into the field of radar imaging. The research presented in this thesis attempts to assist in a novel quest for the combination of the fantastic world of chaos and the exciting world of radar.

Radar or radio detection and ranging, is an electronic device used for the detection and location of objects of interest. All radar systems obtain information about a target by processing the received echo of the signal that was transmitted. The features of the transmitted signal vary depending on the application requirements, and they have an effect on target detection, measurement accuracy, resolution, ambiguities, and clutter rejection [1].

In the design of radar systems, one of the most important goals is the achievement of *high resolution*, that is the ability to resolve closely located targets. In this aspect it is well known that the range resolution of a system is directly related to the transmitted *signal bandwidth* [1;p.496], [2].

Chaotic signals generated by iterated non-linear maps are characteristically *wideband* [3]. This special feature has brought interest into the application of chaotic signals in a variety of areas. In the context of communication theory, the main interest is in exploiting the aperiodic nature of chaos for the transmission of information via broadband chaotic signals [4]. Given that the power spectral density of chaotic signals is broadband they can also be used to achieve high-resolution radar sensing and imaging.

The term *chaos* is utilized in classical articles to describe the statistical nature of physical phenomena in which ergodicity applies [5], such as in the case of Brownian motion. When observed over a finite or infinite interval of time, chaos phenomena vary significantly for small initial condition fluctuations and appear unpredictable [6]. More recently, chaos has been used to describe nonlinear deterministic phenomena and has been extendedly studied in dynamical systems [7].

Chaos can be generated via non-linear functions that produce statistically independent samples with invariant probability density functions. Several chaotic expressions can be considered to generate a radar signal. Among some of the well know discrete maps that have been studied are the logistic, Bernoulli, congruent, circular, exponent, tent, quadratic, Hénon and sine maps. In principle, these chaotic wideband signals generated by such maps can be synthesized via low-order electronic oscillators and circuits [8].

For a given energy level, high resolution is typically achieved by either decreasing the pulse duration of the transmitted signal or by modulation of a relatively long duration transmitted signal [1;p.493], [9;p.22]. By feeding chaotic signals to the input of a voltage-controlled oscillator [10], a stochastic frequency-modulated (FM) signal with fractal features is generated. This chaotic-based FM (CBFM) signal is an ergodic and stationary process with initial random phase. Recent work in the area of radar signal design demonstrated the feasibility of two-dimensional imaging using an FM signal with normal phase distribution [11], pseudo-noise with normal amplitude and uniform phase distribution [12], and chaotic binary phase coding [13].

Chaotic and CBFM signals also present advantages in the field of electronic counter-countermeasures (ECCM). The transmitted signals possess low probability of interception (LPI) and low probability of identification (LPID) due to their random appearance, converting the radar into a masked, hard to detect system. At the same time, the complexity of the signals allow the radar to perform well in unfriendly environments and are robust against interference from noise, jamming, or another radar source. Undesired multipath effects resulting from ground reflections and other reflections from neighbouring objects can be reduced by the exploitation of the inherent wideband nature of CBFM signals as well. Phase errors, caused by echoes following different paths, can be reduced by increasing the bandwidth of the transmitted FM signal [14].

In actual radar applications the target moves such that its echo signal has both time-delay and Doppler-frequency shifts. One of the most important characteristics of a radar system is the ability to estimate these shift values. The ambiguity function describes the response of a radar particular range-velocity resolution cell to a point target, as the range and velocity vary. The ambiguity function and its relationship to resolution were originally introduced by Woodward [15] and since then, it has become a basic tool for signal design and analysis. It can provide a measure of the radar system ability to accurately estimate the range and velocity of a single target. The ambiguity function provides the basis for a systematic search of the best waveform in a particular radar application.

This thesis proposes the use of chaotic and CBFM signals for range-Doppler imaging and uses the ambiguity function to qualitatively investigate the potential of such waveform in a radar system. Chaotic and CBFM signals are of interest in synthetic aperture radar applications for their inherent high range and Doppler resolution capability, potential ease of synthesis, transmission, and electronic counter-countermeasurements performance.

The following chapters offer a detailed research of the topics presented in this introduction. The objective is to demonstrate the feasibility of the use of chaotic signals as a new tool for high-resolution radar imaging. Chapter 2 presents a short review of key concepts in the topic of radar imaging and chaos. Four chaotic maps selected for this thesis are introduced. Theoretical aspects of chaos generation and evaluation are also

presented in Chapter 2. Chapter 3 sets the bases for the signals further simulation and testing and provides the analysis of the signals under study. In Chapter 4, the ambiguity surfaces of the signals are obtained and the results are discussed and examined for range-Doppler resolution. The evaluation of the multipath operation and ECCM capabilities of one of the CBFM signals are estimated, discussed and compared to traditional radar signals. Finally, Chapter 5 provides conclusive remarks, discusses the possible impact that the results can have in radar imaging and outlines further possible research topics.

Chapter 2

Overview

2.1 Radar

Since the early beginnings of history, mankind has always dreamed of the possibility of extending the capabilities of the human senses. Men have often thought about the idea of seeing beyond the eyesight or through the dark. Nowadays, radar systems allow us to accomplish part of this dream. Although it cannot act as a substitute for the human eye, a radar can extend the vision by not only sensing through conditions that are beyond human capabilities, but also by measuring the distance of objects far beyond the human eyesight. These characteristics have made radar systems a very important tool in many modern applications in sea, earth, air and space. Either being used as a navigation, surveillance or meteorological tool, radars find applications in the civilian, military or scientific field.

Basically, radar is used for the detection and location of objects of interest. All radar systems obtain information about an object or target by processing a received echo of the signal that was transmitted. A simplified radar system is shown in Figure 2.1. The system consists of a transmitting antenna emitting electromagnetic radiation generated by a signal transmitter, a receiving antenna and an energy receiver. A portion of the transmitted energy hits the target and is re-radiated in all directions. Part of this energy is usually captured by the radar's receiving antenna and in this manner the target is detected. The returned signal, or echo from a target, is a modified version of the transmitted waveform. Changes in the waveform are caused in part by the parameters of the target, which ideally and in the absence of noise, can be deduced by comparing the

received and transmitted signals. The echo is collected by the antenna and is processed in the receiver with the object to estimate the target parameters.

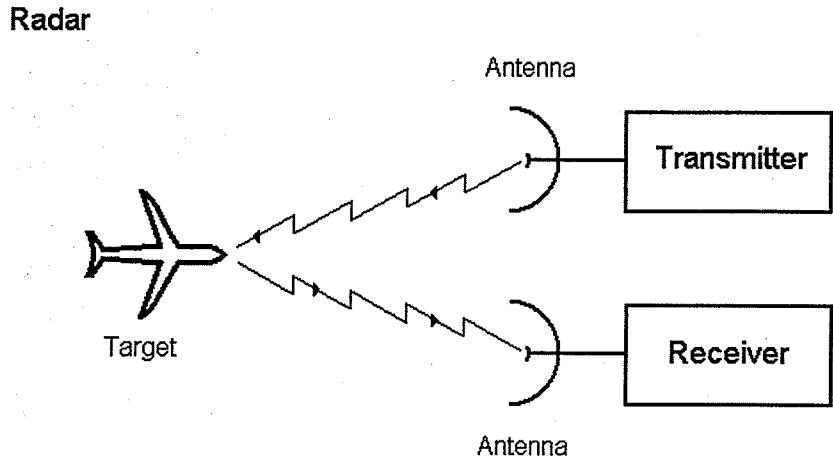


Fig. 2.1. Basic radar system.

The time difference between the transmitted and received signal is denoted by the delay τ . The object of the radar receiver is to determine the value τ from the received signal $r(t)$, given that

$$r(t) = s(t - \tau) + \eta \quad (2-1)$$

where $s(t)$ represents the transmitted signal and η is the noise added to the signal through the total travel time. Noisy is usually assumed to be Gaussian. A copy of $s(t)$ should be available for comparison with $r(t)$ at the receiver. A constant frequency shift or Doppler offset of the whole signal spectrum, proportional to the target radial velocity can also be present in the received signal.

The distance or range from the radar to the target is determined by measuring the time taken by the waveform to travel to and from the target. Given that the electromagnetic energy travels at the speed of light c (299,792,458 m/s), the range is

$$R = \frac{c\tau}{2}, \quad (2-2)$$

The Doppler effect can be described as the frequency shift of the signal reflected by a moving target. The shift ν is given by

$$\nu = \frac{2v_r}{\lambda} \quad (2-3)$$

where v_r is the velocity between the radar and the target and λ is the wavelength of the transmitted signal carrier.

In the design of radar systems, one of the most important goals is the achievement of *high resolution*, that is the ability to resolve closely located targets, both, in the range and in Doppler dimensions. The ability of the measurement system to perform target discrimination is related to the type of transmitted waveform and the detection process implemented at the receiver. In this regard, it is well known that the system's range resolution, ΔR , is directly related to the transmitted *signal bandwidth*, β , [16] by the equation

$$\Delta R = \frac{c}{2\beta} \quad (2-4)$$

At the same time the Doppler resolution can be improved by increasing the carrier frequency c/λ in equation (2-3), and the duration of the transmitted signal [17,p.7].

2.2 Radar signals

The features of the transmitted signal vary depending on application requirements and have an effect on target detection, measurement accuracy, resolution, ambiguities, and clutter rejection. Since the appearance of radar systems, many signals have been proposed for a variety of applications presenting different advantages and drawbacks. Single pulse, constant frequency pulses, linear frequency modulation, hyperbolic frequency modulation, stepped frequency modulation, random frequency modulation, quasi-random phase modulation, random phase-shift modulation, and pure random signal are examples of the different waveforms that have been used in radar systems over the last fifty years.

If different ranges or time-shifts are to be distinguishable at the receiver, the transmitted signal must have the property of being as different as possible from its time-shifted received version. Similarly, this property should be present when the received signal has a frequency shift due to targets motion.

Notwithstanding, the sensitivity of the radar can be made to depend only on the total energy of the received signal provided that an optimum detection procedure is selected. The *matched filter* receiver provides an optimum signal to noise ratio output for radar signals in the presence of noise [18,p.1]. The receiver cross-correlates the received waveform with a suitable time-delayed version of the transmitted signal as described by

$$s_M(t) = \int_{-\infty}^{\infty} r(\tau) s^*(\tau - t) d\tau. \quad (2-5)$$

The output of the radar receiver $s_M(t)$, will peak to a maximum when $t = T_t$ if a target is present at $R = c \cdot T_t / 2$. If a threshold level is established at the output of the receiver, a target is said to be detected whenever a peak in $S_M(t)$ is large enough to cross the threshold. This threshold level usually helps to reduce false alarms created when spurious peaks caused by noise appear in the signal, but at the same time, it may mask true responses from weak targets.

2.2.1 Linear FM chirp

One of the most common waveform used in today's radar systems is the linear FM chirp. The signal allows the operation of the radar with the detection capability of a long pulse but the resolution and accuracy of a short pulse. The transmitted signal consists of a rectangular pulse of constant amplitude A and duration T . The frequency of the transmitted pulse increases linearly from f_1 to f_2 over the duration of the pulse. The received pulses have the same linear increase in frequency. The echoes are passed through a compression filter at the receiver. The filter introduces a time lag that decreases linearly with frequency at the same rate as the frequency of the echoes increases. When the echoes emerge from the filter, they have been compressed in a shorter length, approximately $\frac{1}{\beta}$, where $\beta = f_2 - f_1$, but with greater amplitude $\sqrt{\beta T}$ [1,p.496]. The shape of the compressed pulse is proportional to

$$\frac{\sin(\pi\beta t)}{\pi\beta t} \quad (2-6)$$

Unfortunately the compressed output waveform contains additional *sidelobes* other than the main peak which corresponds to the true target position. These sidelobes are usually small compared to the mainlobe, but they may mask the mainlobe of another weak target reflection present in the received signal.

Linear FM compression is a mean of improving the range accuracy of a long band-limited pulse by a certain amount, at the expense of a loss in Doppler accuracy of the same order. The time and frequency characteristics of the compression waveform is shown in Figure 2.2

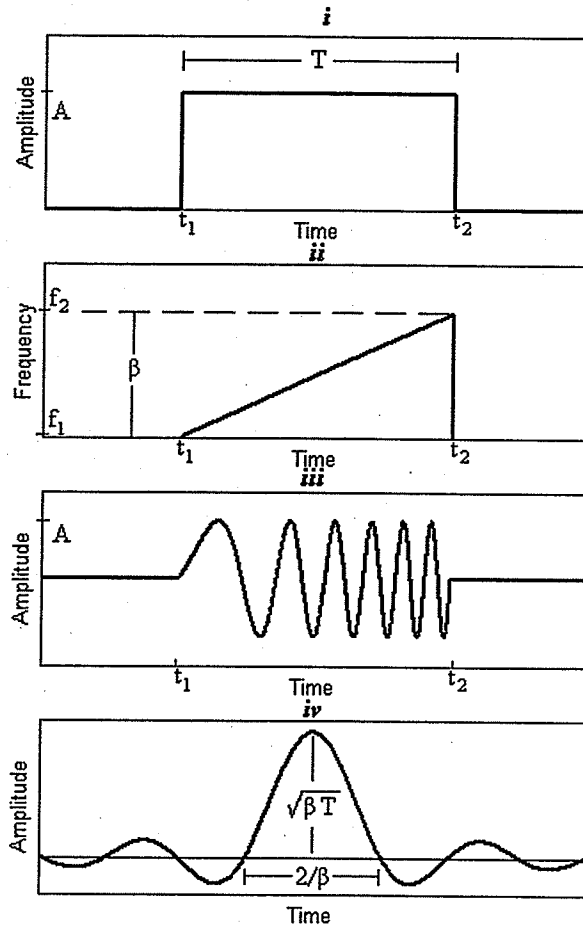


Fig. 2.2. Linear frequency modulation pulse compression waveforms.
i) Amplitude of transmitted waveform; *ii)* Frequency of transmitted waveform; *iii)* Time waveform described by *i)* and *ii)*; Output of the pulse-compression filter at receiver.

2.2.2 Random and noise modulation

Noise modulation radar systems operate by transmitting a signal modulated by a lower frequency noise source. Because of the inherent bandwidth of this type of systems, good resolution, accuracy and unambiguous measurements of target range and velocity can be achieved.

Most noise modulated radars operate under the principle of anticorrelation [19]

$$1-R(\tau) = 1 - \lim_{T \rightarrow \infty} \frac{1}{T} \int_0^T s(t) \cdot s(t-\tau) dt \quad (2-7)$$

to estimate the target range, while the output of a Doppler filters bank yields the target velocity. A typical anticorrelation block diagram is shown in Figure 2.3. The system radiates energy that is modulated in frequency by a random function. If a target is close to the antenna, the transmitted and echoed signals will have a high correlation because the transmitter does not have sufficient time to make a great change in frequency. As a result, the received waveform has approximately the same frequency characteristics of the signal being generated at the transmitter. For a target located at a longer range, the time delay of the echo is longer and there is a higher probability of a large change in the transmitted signal. Usually a sample of the transmitted signal is used as the local oscillator input in a conventional mixer. The mixer output has an instantaneous frequency (IF) equal to the instantaneous frequency difference of the transmitted and returned signals.

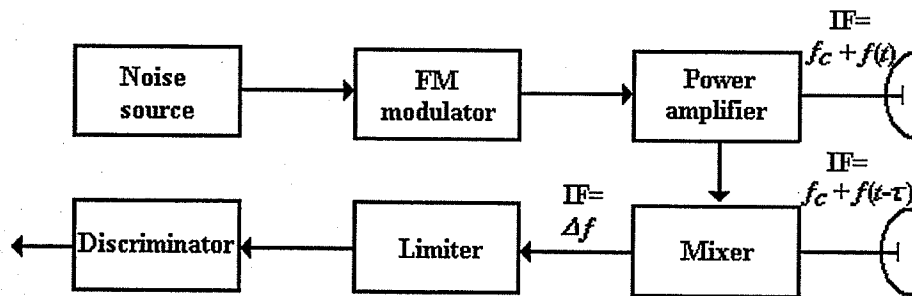


Fig. 2.3. Basic noise modulated radar system.

As described by Horton [19], if the random noise function $N(t)$ is assumed to have a Gaussian probability distribution and the frequency deviation characteristic of the transmitter is linear, the transmitted signal will have a Gaussian probability with the same mean value. The instantaneous frequency of the frequency-modulated signal is $f_c + f(t) = f_c + K \cdot N(t)$, where f_c is the carrier frequency and K is the modulation index. Consequently, the echo signal has an instantaneous frequency $f_c + f(t-\tau) = f_c + K \cdot N(t-\tau)$ and the instantaneous frequency difference is

$$\Delta f = f(t) - f(t - \tau) = K \cdot N(t) - K \cdot N(t - \tau). \quad (2-8)$$

It is assumed that Δf has a Gaussian probability distribution with zero mean. Because the mixer does not preserve the algebraic sign of the frequency difference, the output is a one-sided Gaussian distribution with maximum at zero. The target range is then determined by measuring the mean $|\overline{\Delta f}|$, which is directly related to the anticorrelation function [19]

$$|\overline{\Delta f}|^2 = \frac{4}{\pi} f(t)_{rms}^2 \{1 - R(\tau)\}. \quad (2-9)$$

Systems that are modulated with a periodic signal are subject to ambiguities for targets whose delays are larger than the repetition period of the sensing signal. In random and noise modulation radars, the spectrum of the transmitted signal is not a harmonic series; consequently they are less prone to the ambiguity problem. For military purposes, noise modulation presents excellent ECCM capabilities including LPI and LPId, which are needed in order to select the proper ECM jamming. Civilian applications benefit of the strong electromagnetic compatibility (EMC) of random and noise radars to discriminate against other contaminating radar signals.

2.3 Ambiguity function

The echo from a target is a modified version of the transmitted waveform. These modifications are due to the parameters of the target, which ideally and in the absence of noise, can be deduced by comparing the returned and transmitted signals. The radar return is assumed to be different from the transmitted signal in only:

- The time delay, which is proportional to the radial range of the target.
- A spectral Doppler offset proportional to the target radial velocity. This offset is positive for a target travelling towards the radar and negative if the target is travelling away from the radar.

Strictly speaking, the assumption of constant Doppler shift is only an approximation that is valid for radial velocities that are small compared to the propagation speed of the transmitted energy. Additionally, the received signal is usually contaminated by noise and the reflection is attenuated by a variety of reasons.

The ambiguity function describes the response of a system to a point target echo as the target range and velocity vary. The ambiguity function and its relationship to resolution were originally introduced by Woodward [20]. Since then it has become a basic tool for signal design and analysis. In terms of the Doppler frequency ν and time-delay τ of the signal $s(t)$, the ambiguity function surface is defined by,

$$|\chi(\tau, \nu)|^2 = \left| \int_{-\infty}^{\infty} s(t) \cdot s^*(t + \tau) \cdot e^{-j2\pi\nu t} dt \right|^2 \quad (2-10)$$

where $s^*(t)$ is the complex conjugate of the transmitted signal. The ambiguity surface can be viewed as a time-frequency correlation function of the signal, similar to equation (2-5). It graphically indicates the accuracy and ambiguity afforded by the transmitted signal in the time (i.e. target range) and Doppler (i.e. target velocity) domains. The peak value of the function occurs at $\tau = 0$, $\nu = 0$, where signals are matched, and its value is equal to twice the signal energy. The volume under the function is also constant and equal to the squared value of twice the signal energy. It is important to understand that τ and ν represent differences in range and velocity of points to be resolved, rather than actual ranges and velocities.

The ideal ambiguity function would consist of a single two-dimensional delta function centered at the origin. This single spike eliminates any ambiguities, and its infinitesimal thickness at the origin permits the echo delay and frequency shift to be determined simultaneously with complete accuracy. It would also discriminate two or more targets, no matter how closely together they are. Naturally the achievement of such an ideal ambiguity function diagram is not possible. Feasible ambiguity surfaces are wider in their mainlobe than a Dirac delta. This gives rise to resolution problems because the response from two close targets can result in the inseparable fusion of their two mainlobes. Similarly an ambiguity function with more sidelobes can result in ambiguities in

detection and masking of weaker target responses. In general there are only three types of ambiguity functions: the ridge, the 'bed of nails', and the thumbtack. The ridge is used when the target velocity is unknown and is generated by processing a constant frequency rate signal. The bed of nails is used when a specific area of the ambiguity surface is to be free of sidelobes and is obtained by processing pulse trains. The inherent periodicity of these signals causes the ambiguity function to present a series of peaks in the delay-Doppler plane. The thumbtack ambiguity function is produced by processing noise-like signals. In this case there are no ambiguities since there is only one peak in the delay-Doppler plane, but the single peak may be too broad to satisfy the requirements of high accuracy and resolution.

The ambiguity surface provides the basis for a systematic search for the best waveform for a particular radar application. Radar performance in terms of the capability to resolve target and clutter scatterers in range and velocity dimensions can be assessed by directly examining the ambiguity surface in the range-velocity plane. Because of its paramount importance in the assessment of signal performance in radar systems, the ambiguity surface has become one of the main tools for radar analysis, and its magnitude has been calculated for a variety of radar waveforms, including periodic pulse trains [1,p.487], single frequency modulated pulses [21], linear FM chirp [17,p34], [22], step frequency radar [23], Gaussian random noise [24], phase coded signals [25], and Chaotic phase coded signals [26].

2.4 Chaos

Chaos is a term used to describe very complex behaviour observed on otherwise simple systems. Chaotic behaviour appears random and unpredictable, even though the system in which the chaos is observed is perfectly described by a simple set of equations and no noise is present. The apparent contradiction between randomness and determinism has made chaos a fascinating field and one of the fastest growing areas of study in recent years.

Chaotic behaviour seems to be universal. It is present in mechanical oscillators, electrical circuits, chemical reactions, lasers, heat fluids and nerve cells, to mention a few. Even more importantly, the chaotic behaviour shows universal characteristics independent of the particular system [27], [28]. In the field of mathematics, chaos refers to the apparent randomness and unpredictability that occurs in *non-linear deterministic dynamical systems*.

Non-linear dynamics is concerned with the study of systems whose time evolution equations are not linear. In general, almost all real systems are strictly non-linear, which is one key reason why this branch of mathematics is important. The apparent randomness in chaotic behaviour is in reality not random at all because its nature is dictated by the set of equation describing the system. The non-linearity is the critical requirement for a system to present chaos. Albeit all chaotic systems are non-linear, this does not guarantee that all non-linear systems are chaotic. A non-linear system may have a stable response to a certain input, but a slight variation on the input may cause an oscillatory or even aperiodic response in the same system. This sensitivity to a control parameter and the initial conditions are characteristic of chaotic systems. A prediction of the future state of the system is impossible because a small error in the exact value of the current condition will have a great impact in future states. For some parameters, the aperiodic dynamics are independent of the initial condition and all input or initial values introduced to the system will lead to an aperiodic but bounded behaviour. A dynamical system that is sensitive *dependent to initial conditions*, *topologically dense* set of periodic points, and *topologically transitive* is said to be chaotic [3], [29].

2.4.1 Chaos in iterated maps

An iterated map is the simplest display of discrete non-linear systems that can present chaotic behaviour. The idea of using iterated maps to study chaotic phenomena was first proposed by Henri Poincaré at the beginning of the 20th century [27].

A map associates a unique object to every point in a set. Therefore a map $f: A \rightarrow B$ from A to B is a function, f , such that for every $a \in A$, there is a unique object $f(a) \in B$. An iterated map gives the value of a future state x_{n+1} as a function of the current state x_n

$$x_{n+1} = f(x_n, D) \quad (2-11)$$

where the value x_n is a real or complex number, the time step $n=0,1,2,\dots,N$ is an integer number, and D is a control parameter. The set of values $\{x_0, x_1, \dots, x_N\}$ is called *orbit* or *trajectory* of the map. In order for an iterated map to display a chaotic behaviour, the mapping function f has to be non-linear. In a chaotic iterated map, the behaviour of the orbit will be extremely sensitive to the control parameter D and the initial condition x_0 . For some values of D in equation 2-11, the orbit may either diverge or converge to 0 or any other value as the number of iteration iterations grows. As the parameter value varies, the behaviour of the orbit may present interesting characteristics, namely the manifestation of oscillatory behaviour as the orbit is iterated. The appearance of *period doubling* [30,p.168] as the parameter D changes can be easily observed in a *bifurcation diagram* like the one shown in Figure 2.4. The bifurcation diagram of a chaotic map is obtained by selecting a random initial condition, iterating the map from a specific control parameter and plotting the value of the trajectory points generated by the iteration process. If the trajectory settles in a single point, the bifurcation diagram will show only one value at that specific control parameter value. If for another parameter value the trajectory oscillates between two points, the bifurcation diagram will show 2 points at that parameter value. The presence of chaos in a map can be appreciated by analysing the bifurcation diagram of the iterate map.

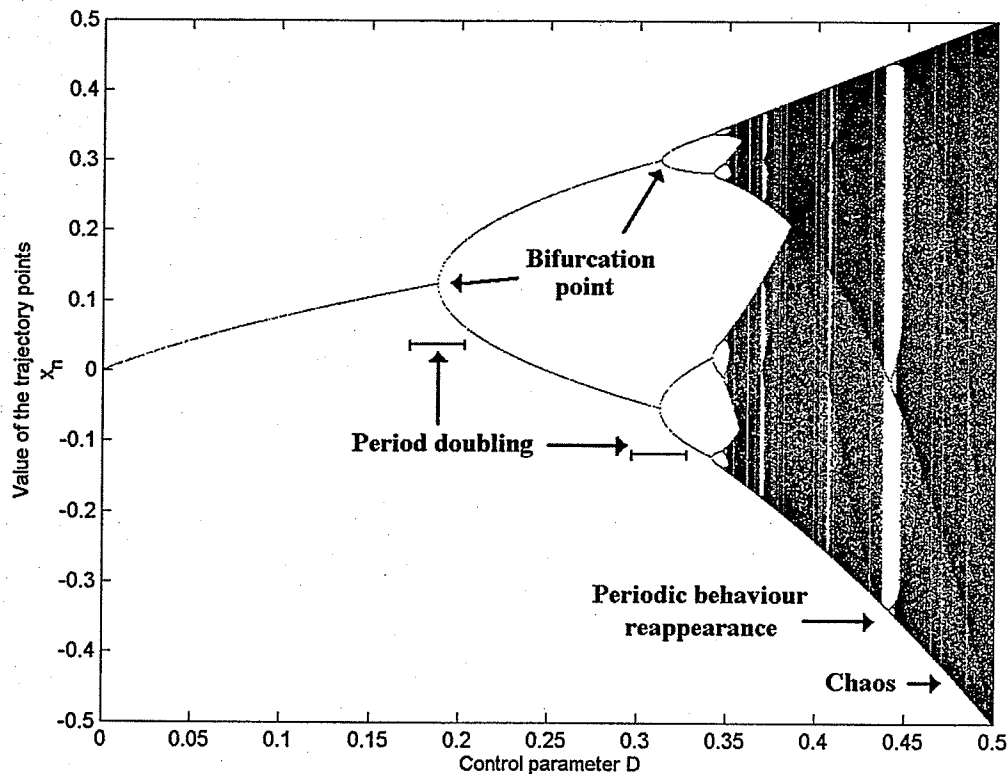


Fig. 2.4. Partial bifurcation diagram of chaotic map.

The bifurcation diagram shows the succession of period doubling produced in the map trajectory as the control parameter D increases. If this behaviour of doubling continues, chaos will occur in the bands where the period is infinite, resulting in a uniform distribution of points on the vertical axis. At this point, the aperiodic nature of the orbit is independent of the initial condition and any initial value (except for fixed points) will lead to the chaotic behaviour. It is important to note that chaotic behaviour does not imply an unstable response. A chaotic orbit is always bounded, even though no point will ever be repeated on the orbit. This kind of stability is sometimes called *chaotic stability*.

The analysis of the bifurcation diagram easily reveals the appearance of chaos in a map or any other system for which such a diagram can be computed. However, chaos can arise in systems for which the calculation of the bifurcation diagram is not known, or from a data series for which the generating equation is not known. Several statistics can be used to indicate the possible presence of chaos and how chaotic a system is. The most

important quantitative measures are the Lyapunov exponent and fractal dimensions. These statistics can be helpful in distinguishing chaos from noise [7],[29].

2.4.2 Lyapunov exponent

One of the main characteristics of chaotic behaviour is the great dependence on initial conditions. A small difference in two close initial conditions, will give raise to a large trajectory difference after a few iterations. This condition can be easily appreciated in the trajectories of the chaotic map presented in Figure 2.5.

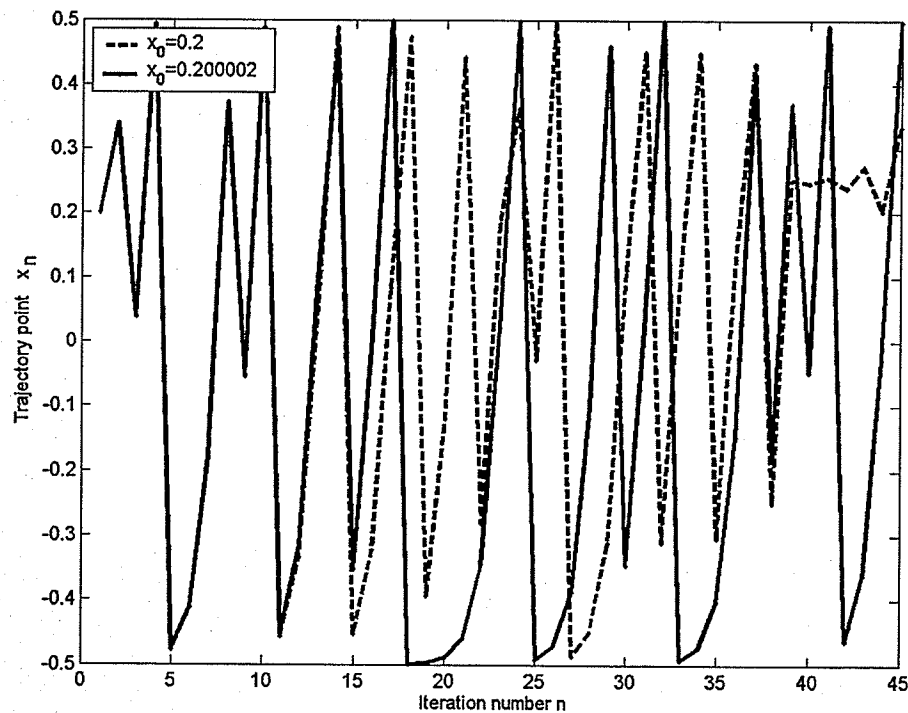


Fig. 2.5. Divergence of close trajectories in chaotic map.

The Lyapunov exponent is a number that describes the dynamics of the orbit; it gives a notion of the divergence of nearby trajectories, presenting a method to quantify chaotic behaviour. If two trajectories start off with a separation d_0 at time $t=0$, and the system is assumed to be chaotic, then the trajectories are expected to diverge so that their

separation at time t satisfies the expression

$$d(t) = d_0 e^{\lambda_1 t}. \quad (2-12)$$

The parameter λ_1 in equation (2-12) is called the largest Lyapunov exponent, first Lyapunov exponent, Lyapunov number or simply, Lyapunov exponent. More specifically, for an iterated map the separation d_n grows as a function of the iteration number n . For a starting point x_0 in the trajectory and another neighboring point $x_0 + \varepsilon$ the difference between the evolving trajectories when the map is iterated n times is

$$d_n \equiv |f^{(n)}(x_0 + \varepsilon) - f^{(n)}(x_0)|. \quad (2-13)$$

If the behaviour is chaotic the difference is expected to grow exponentially with n . Then, equation (2-13) can be written as,

$$\frac{d_n}{\varepsilon} = \frac{|f^{(n)}(x_0 + \varepsilon) - f^{(n)}(x_0)|}{\varepsilon} \equiv e^{\lambda_1 n} \quad (2-14)$$

or taking the logarithms of equation (2-14);

$$\lambda_1 = \frac{1}{n} \log \left(\frac{|f^{(n)}(x_0 + \varepsilon) - f^{(n)}(x_0)|}{\varepsilon} \right). \quad (2-15)$$

Letting $\varepsilon \rightarrow 0$, the ratio on the right-hand side of equation (2-15) becomes the derivative of $f(n)$ with respect to x . Additionally, by the chain rule, the derivative of $f^{(n)}$ can be written as a product of n derivatives of $f(x)$ evaluated at the successive trajectory points $x_0, x_1, x_2, \dots, x_{n-1}$ and therefore the Lyapunov exponent can be now written as,

$$\lambda_1 = \frac{1}{n} \ln(|f'(x_0)| |f'(x_1)| \dots |f'(x_{n-1})|) \quad (2-16)$$

where $f'(x)=df/ dx$. Equation (2-16) can finally be rewritten as

$$\lambda_1 = \frac{1}{n} (\ln|f'(x_0)| + \ln|f'(x_1)| + \dots + \ln|f'(x_{n-1})|). \quad (2-17).$$

Hence, according to equation (2-17), the Lyapunov exponent can be calculated as the average of the absolute value of the derivatives of the map function evaluated at the trajectory points. If the Lyapunov exponent cannot be obtained analytically, and instead is numerically calculated for a set of different trajectories starting from different initial points x_0 , the average is called the *average Lyapunov exponent* [7]. In cases where only measured data is available, the average Lyapunov exponent can be approximated from the slope of a semi-logarithmic plot showing the logarithm of the separation of two close values x_i and x_j in the data series with respect to the iteration value n

$$d_0 = |x_j - x_i|, d_1 = |x_{j+1} - x_{i+1}|, \dots, d_n = |x_{j+n} - x_{i+n}| \quad (2-18)$$

If λ_1 is found to be positive, either analytically or numerically, the trajectories in the map diverge, and the map is said to be sensitive to the initial conditions. In contrast, if the value of λ_1 is zero or negative the trajectories do not diverge or converge respectively. A positive Lyapunov exponent quantifies the sensitive dependence to initial conditions and is one of the most important indicators of chaos. A one-dimensional iterated map function has chaotic trajectories for a particular parameter if the average Lyapunov exponent is positive for that specific parameter value.

2.4.3 Fractal dimensions

Unlike the measure of the embedding or Euclidean dimension of an object (i.e. the minimum number of coordinates needed to describe the points on an object), the fractal dimension is a non-integer quantity. It is a quantitative numerical way of evaluating or comparing the geometric and/or probabilistic complexity of objects. The fractal dimension can be interpreted as the degree of irregularity of an object [29,ch.2,pp.29]. Fractal dimensions remain constant over a range of measuring scales and are often used to quantify chaos. There are many fractal dimensions that can be used to quantify chaos; the most commonly mentioned are the similarity, capacity, Minkowski, Gyration, Hausdorff-Besicovich, information, correlation, variance and Renyi dimensions [7,p.341], [29,ch.2],[30,p.289].

Most of these fractal dimensions are related in some way and they may even have the same numerical value for certain conditions. Most dimensions can be organized into categories. The first category measures only the geometry of the chaotic attractor. Examples of these morphological dimensions are the *similarity dimension* and the *Hausdorff-Besicovich dimension*. The second category not only considers geometry, but also probabilistic and informational aspects of the object or set. They take into account that a trajectory may visit a neighborhood more often than others. Examples of this category are the *information* and *correlation dimensions*. Other fractal dimensions are *spectral* [29,ch.2,pp.99] or *variance-based* [29,ch.2,pp.103] and can be classified into separated categories.

2.4.3.1 Correlation dimension

The correlation dimension D_C [7,p.354] is a fractal dimension based on the behaviour of the *correlation sum*. It has been used to characterize chaotic attractors and has a computational advantage because it uses the trajectory point to directly calculate the dimension value. Like all the fractal dimensions, the correlation sum involves measurements at different scales. It is calculated by placing the multi-scale measuring instrument in each point in the set. For each scale, the number of points inside the scaling area are counted and these values are normalized by the total amount of points in the data set. The procedure is repeated at all different scales for all points. For a N points trajectory $\{x_0, x_1, \dots, x_{N-1}\}$, the correlation sum is defined by,

$$C(R_k) = \frac{1}{N(N-1)} \sum_{i=1}^N \sum_{j=1, j \neq i}^N \Theta(R_k - |x_i - x_j|) \quad (2-19)$$

where Θ represents the Heaviside step function and defines the number of points within the distance R_k of the i^{th} point. The sum can also be written in terms of relative frequency P_i of pairs within the distance R_k [27,p.192],

$$C(R_k) = \sum_{i=1}^N P_i^2 \quad (2-20)$$

The correlation dimension D_C is then defined to as number that satisfies

$$C(R_k) = \lim_{R_k \rightarrow 0} R_k^{D_C} \quad (2-21)$$

or

$$D_C = \lim_{R_k \rightarrow 0} \frac{\log C(R_k)}{\log R_k}. \quad (2-22)$$

In view of the fact that it is not possible to take the limit $R_k \rightarrow 0$, in practice $C(R_k)$ is computed for some range of R_k values and the points plotted in a log-log plot. The slope of such plot is then considered to be the correlation dimension of the object.

2.5 Investigated chaotic maps

There are many known non-linear equations or systems that can present chaos. However, besides non-linearity, the complete list of requirements that guarantee chaos has not been discovered. The four non-linear maps studied in this project are the logistic, Bernoulli, tent, and quadratic maps. All four maps can be considered classic in the area of chaos and have been studied in the last couple of decades.

Figures 2.6, 2.8, 2.10 and 2.12 show the bifurcation diagrams of the logistic, Bernoulli, tent and quadratic maps respectively. The diagrams show the succession of period-doubling produced as the control parameter D increases in each map. Chaos occurs in the bands where the points seem to be distributed at random (i.e. infinite periodicity). For each value of D , the system is first iterated 2000 times in order to avoid any transitory conditions and then the successive values of x are plotted for a few hundred iterations. Notice that for several values of D , periodic behaviour reappears within the chaotic range for the quadratic maps.

Figures 2.7, 2.9, 2.11 and 2.13 show the time series of the iterated maps in the chaotic region. The samples were generated using an arbitrary initial condition x_0 . Notice that the samples look unsystematic, similar to noise, but never exceed the appropriate bounded range.

Table 2.1 summarizes the parameters used in the bifurcation diagram of each of the four maps and indicates the selected parameter value for operation in the chaotic range. The values of the control parameter D will be held constant throughout this thesis.

TABLE 2.1
Chaotic maps and respective control parameter value.

Map	Range	Control parameter D
Logistic	[1,4]	4
Bernoulli	[1,2]	2
Tent	[1,2]	2
Quadratic	[0,½]	½

2.5.1 Logistic map

Probably the best known iterated map that presents chaotic behaviour is the logistic equation. Originally intended to model population growth in discrete time intervals, it has been widely studied because of its simplicity and parametric control. The logistic equation is fully described by

$$x_{n+1} = D x_n (1 - x_n) \tag{2-23}$$

where $x_0 \in [0,1]$ and D represents the growth constant which at the same time acts as the bifurcation control parameter. Notice that the quadratic term introduces the non-linear element required for chaotic behaviour.

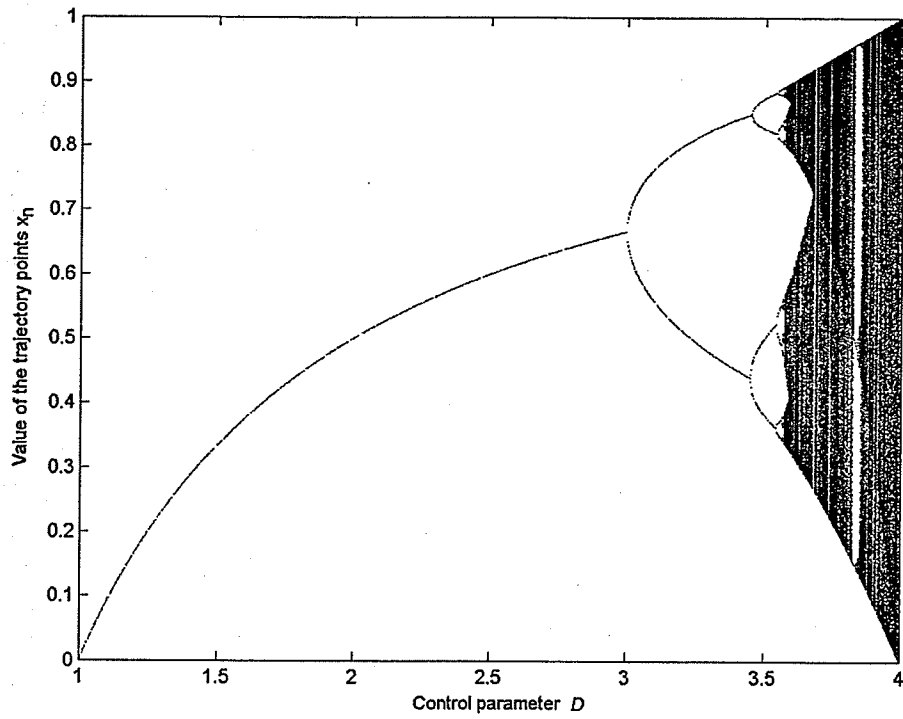


Fig. 2.6. Bifurcation diagram of logistic map.

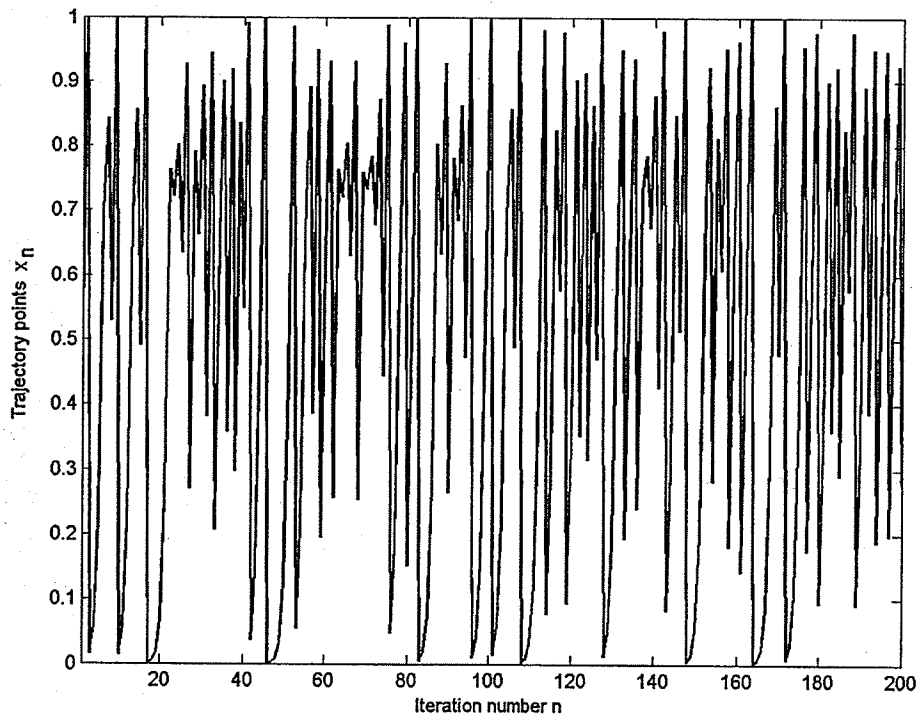


Fig. 2.7. Chaotic trajectory of logistic map for $D=4$.

2.5.2 Bernoulli map

The Bernoulli shift map or modulo 2 map is given by

$$x_{n+1} = \begin{cases} Dx_n + 1/2 & \text{for } x_n < 0 \\ Dx_n - 1/2 & \text{for } x_n > 0 \end{cases} \quad (2-24)$$

where $x_0 \in [-1/2, 1/2]$. The map presents a discontinuity at 0, and the conditional term introduces the non-linearity in the system.

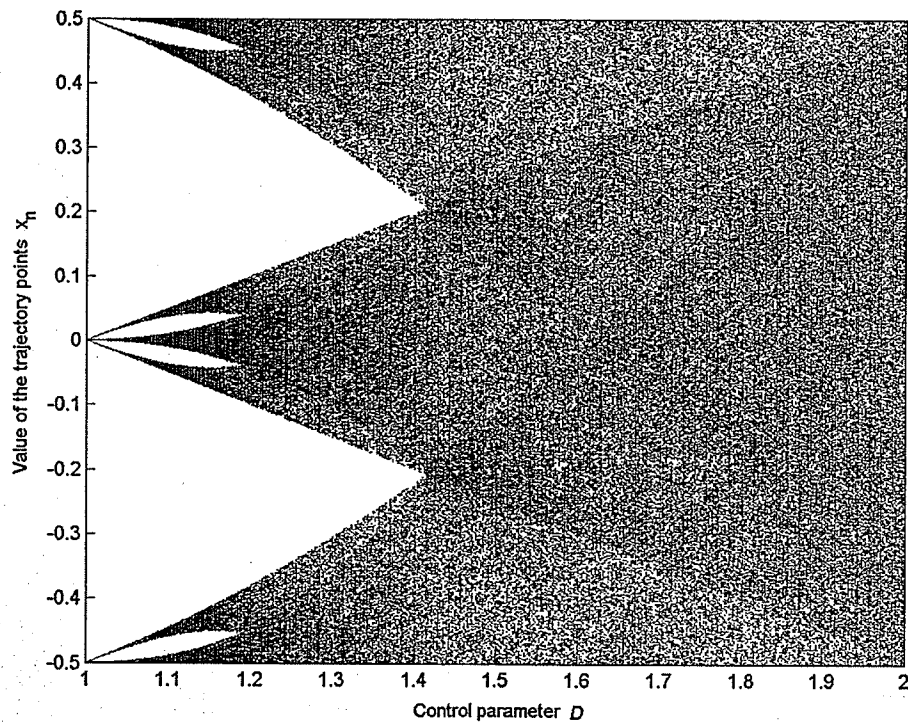


Fig. 2.8. Bifurcation diagram of Bernoulli map.

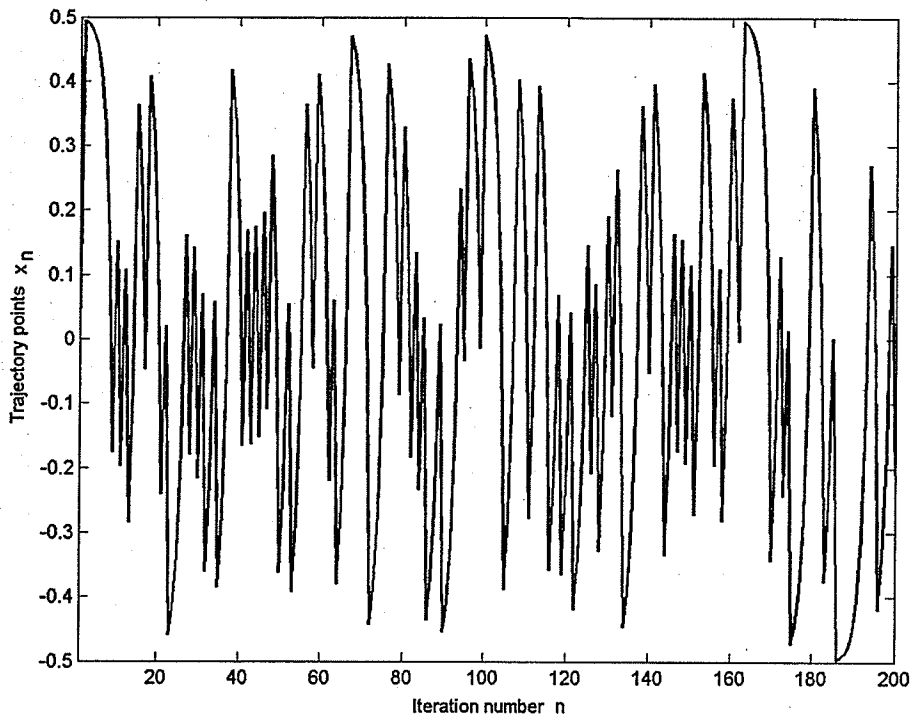


Fig. 2.9. Chaotic trajectory of Bernoulli map for $D=2$.

2.5.3 Tent map

The tent map has similar properties to the closely related Bernoulli map, and is defined as

$$x_{n+1} = 1/2 - D |x_n| \quad (2-25)$$

for $x_0 \in [-1/2, 1/2]$. In the tent map, the non-linearity is introduced by the absolute value operator.

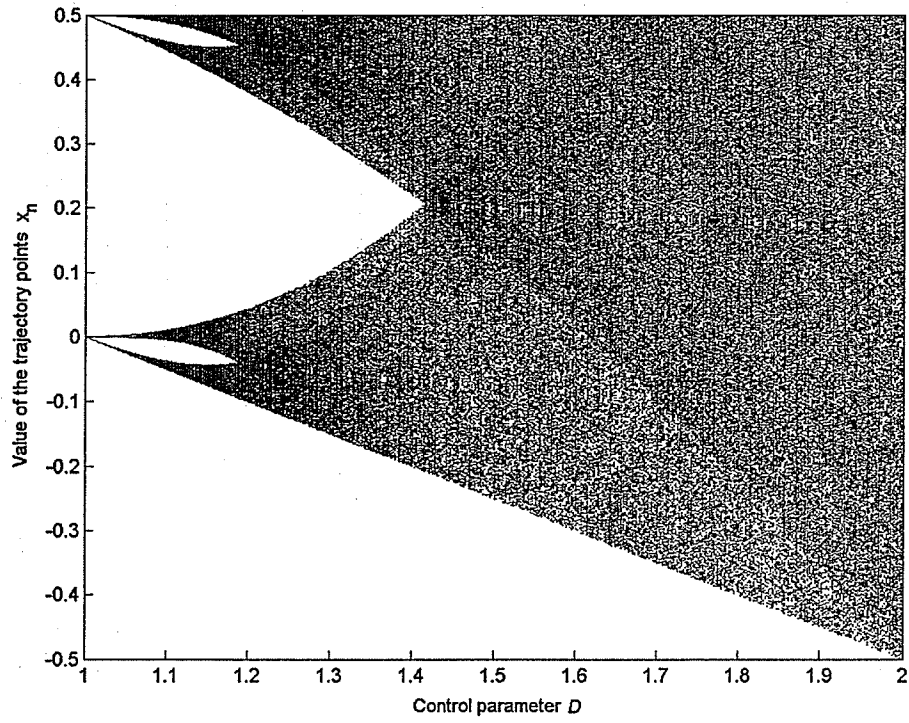


Fig. 2.10. Bifurcation diagram of tent map.

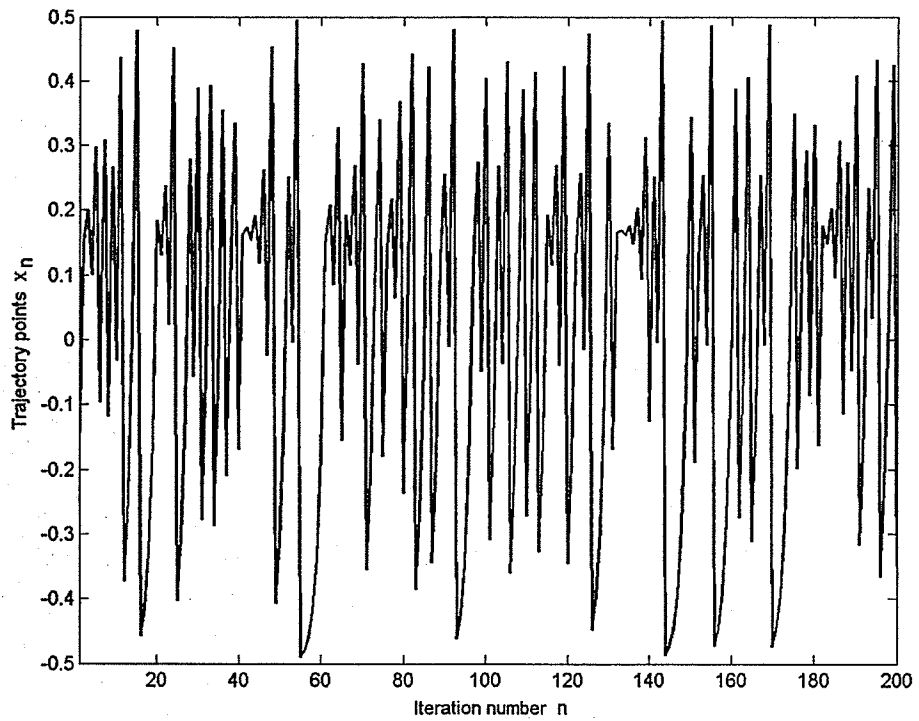


Fig. 2.11. Chaotic trajectory of tent map for $D=2$.

2.5.4 Quadratic map

The quadratic map is given by

$$x_{n+1} = D - 4(x_n)^2 \quad (2-26)$$

where $x_0 \in [-\frac{1}{2}, \frac{1}{2}]$. The name quadratic obeys to the nature of the non-linearity in equation (2-26). However the map presented in this thesis is only a special case of many quadratic maps known to present chaotic behaviour.

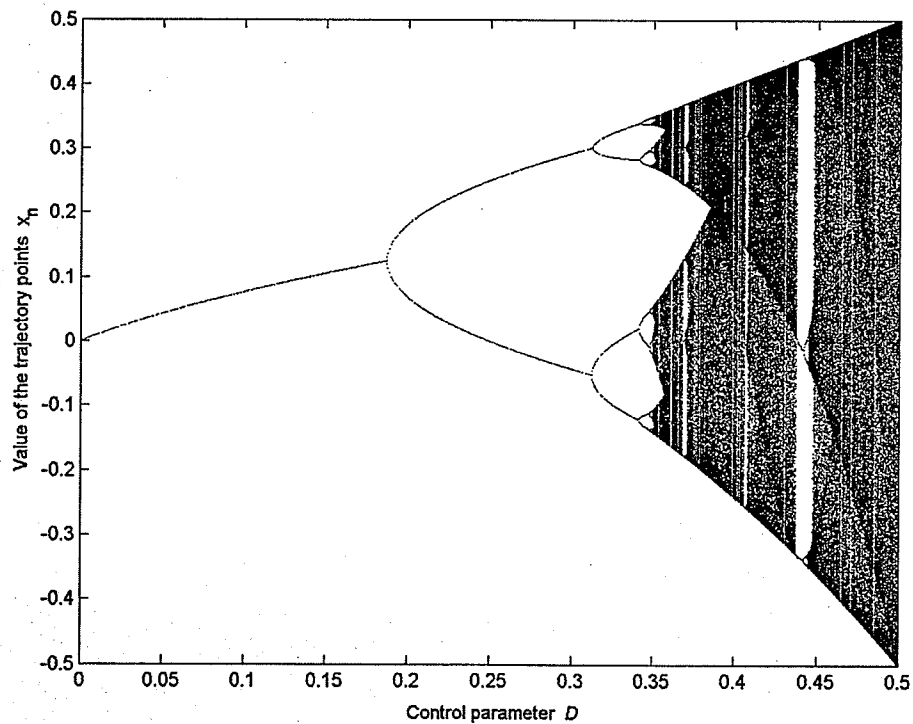


Fig. 2.12. Bifurcation diagram of quadratic map.

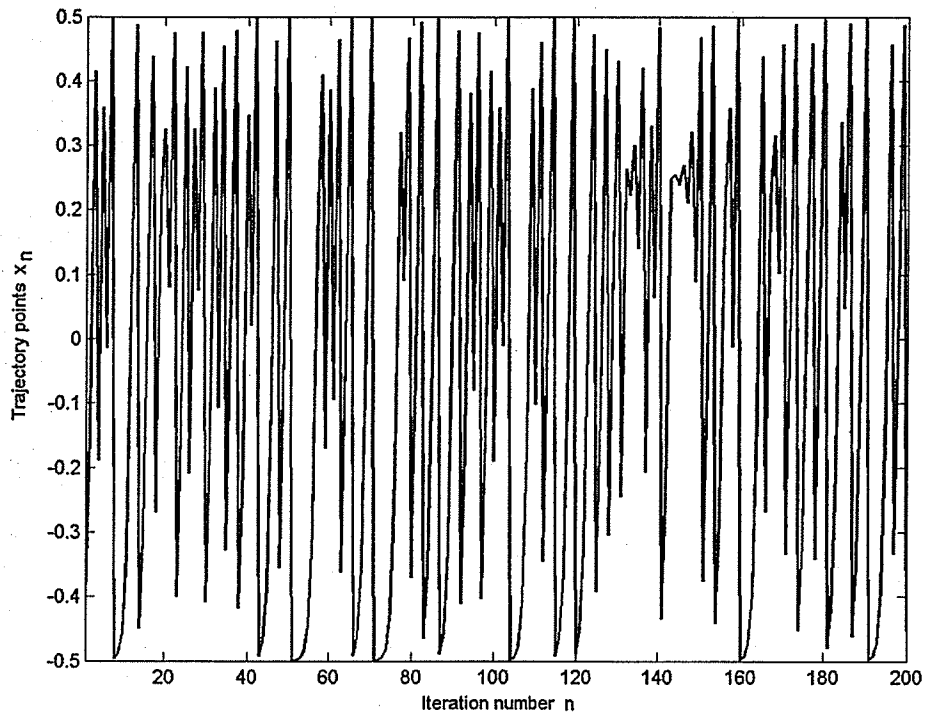


Fig. 2.13. Chaotic trajectory of quadratic map for $D=1/2$.

Chapter 3

Signal analysis

3.1 Analysis of chaotic signals

3.1.1 Ergodicity of chaotic signals

For any discrete signal $d(n)$ to be ergodic in the mean, the following equality must be satisfied:

$$E\{d(n)\} = \langle d(n) \rangle \quad (3-1)$$

where $\langle \cdot \rangle$ denotes a time average over the interval $0 \leq n \leq N$ as $N \rightarrow \infty$. The signal $d(n)$ is ergodic in the autocorrelation if both the ensemble mean and the time mean of the product $d(n) \cdot d^*(n+m)$ are the same, i.e.

$$R(m,n) = E \{d(n) \cdot d^*(n+m)\} = \langle d(n) \cdot d^*(n+m) \rangle. \quad (3-2)$$

When a formal verification of (3-1) and (3-2) cannot be achieved, an experimental study of the signal distribution can be utilized [31]. Figure 3.1 shows that the histograms of the chaotic signals described in section 2.5 approach their density regardless of whether the histogram is obtained from either a single realization of N samples or from the n^{th} sample of an experimental ensemble. The histograms on the right side of Figure 3.1 were obtained by processing 100,000 samples of a single realization of $x(n)$ with random initial value x_0 using equations (2-23), (2-24), (2-25), and (2-26). The histograms on the left

were obtained from the 1,000th sample of 100,000 realizations of $x(n)$ with an arbitrary initial condition x_0 drawn from a uniform distribution in the appropriate range. Each initial condition was used to generate a signal $x(n)$ of length 1,100 where the first 100 values of $x(n)$ were dropped in order to avoid transients and to assure that the chaotic model had evolved on its attractor.

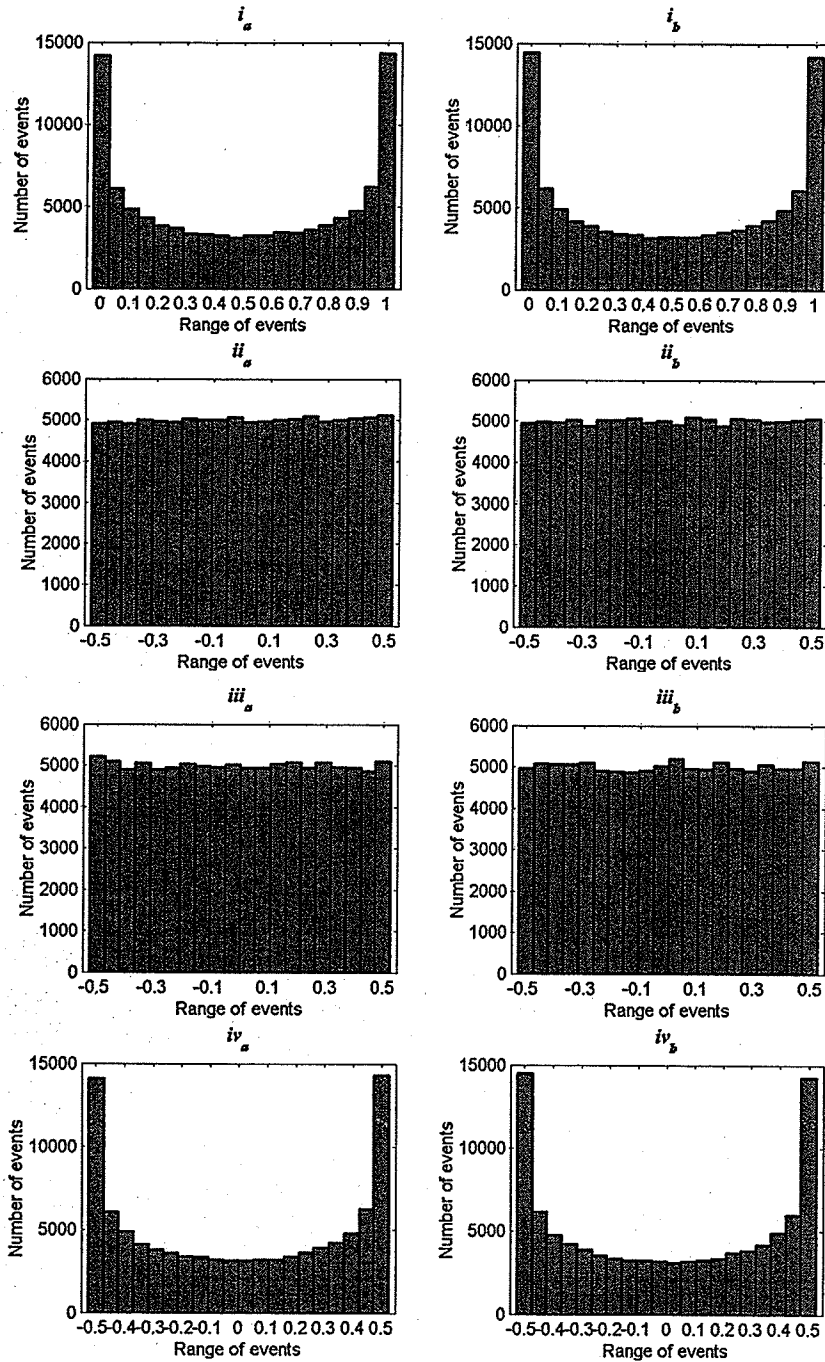


Fig. 3.1. Ergodicity in selected chaotic maps.
 Time (a) and ensemble (b) distributions of the *i*) logistic; *ii*) Bernoulli; *iii*) tent; *iv*) and quadratic map.

The ergodicity in the mean of x is apparent in these examples. The experimental form of the distributions, and the total error between histograms are summarized in Table 3.1.

Ergodicity in iterated chaotic maps is a characteristic derived from the *transitive property* [29] of chaos. In a chaotic map, an initial point x_0 after a sufficiently long number of iterations will produce points within the map interval that will be arbitrarily close to any other point. As a consequence, sequences obtained from different initial conditions are not very different statistically from each other in a long run. The assumption of stationarity is also valid for chaotic sequences and can be easily verified experimentally by comparing the ensemble distribution of samples for different iteration times (e.g. the histograms in the left side of figure 3.1 are identical to histograms generated with the 350th sample of 100,000 realization).

3.1.2 Autocorrelation and power spectrum of chaotic signals

When dealing with wide sense stationary signals, the power spectral density $S(f)$ of the chaotic signal is merely the Fourier Transform of the signal autocorrelation $R(m)$. It is possible to roughly estimate both the autocorrelation and the spectrum of the signal from a single realization of the chaotic signal [13]. However, it is preferable to lower the variance of the autocorrelation or spectrum by utilizing traditional approaches such as the correlogram or periodogram [32], [33].

For this analysis, M signal realizations of each chaotic map were generated with uniform random initial condition x_0 . The biased time autocorrelation $R_i(m)$ was then computed for each realization and the average bin by bin autocorrelation calculated. Subsequently the discrete-time Fourier Transform (DFT) was performed for the resulting average to obtain the spectral estimate

$$D(f) \approx \text{DFT} \left\{ \frac{1}{M} \sum_{i=1}^M R_i(m) \right\}. \quad (3-3)$$

Figure 3.2 shows the averaged autocorrelations of the chaotic maps on a decibel scale. The rapid decorrelation of the chaotic signal x is evident. In all instances, the autocorrelation estimate approaches a delta with normalized sidelobe level (SLL) of the order of $N^{1/2}$.

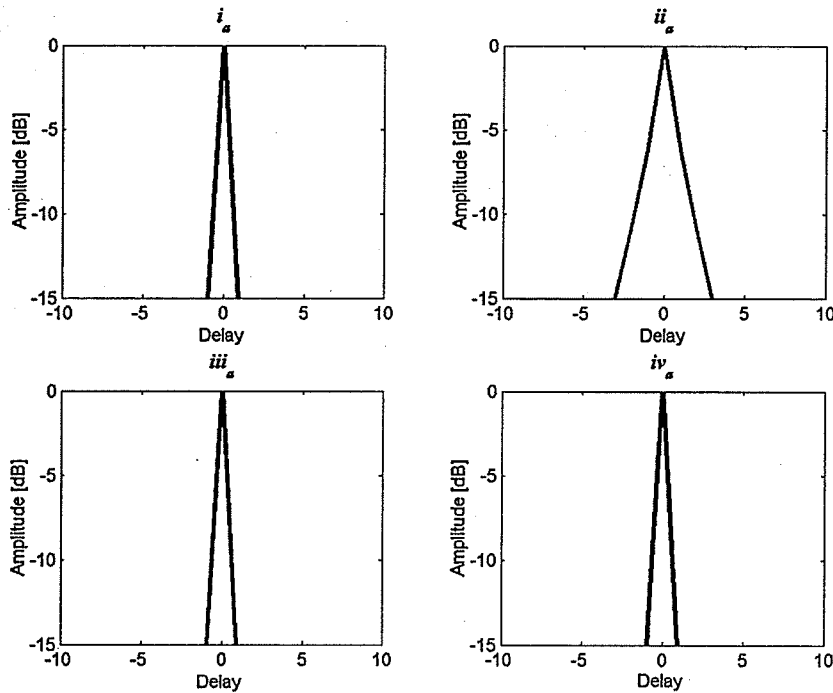


Fig. 3.2. Averaged autocorrelation of chaotic sequences.
i) logistic map; *ii)* Bernoulli map; *iii)* tent map; *iv)* quadratic map.

The power spectra obtained using equation (3-3) are depicted in Figure 3.3. The spectra are not surprisingly wideband, similar to those generated by white noise. Notice that the Bernoulli map is the only sequence that does not present a completely flat spectrum, instead the density resembles a low pass signal with a slope of $1/f$ characteristic of pinkish noise [29] at higher frequencies. The results shown in Figures 3.2 and 3.3 are summarized in Table 3.1.

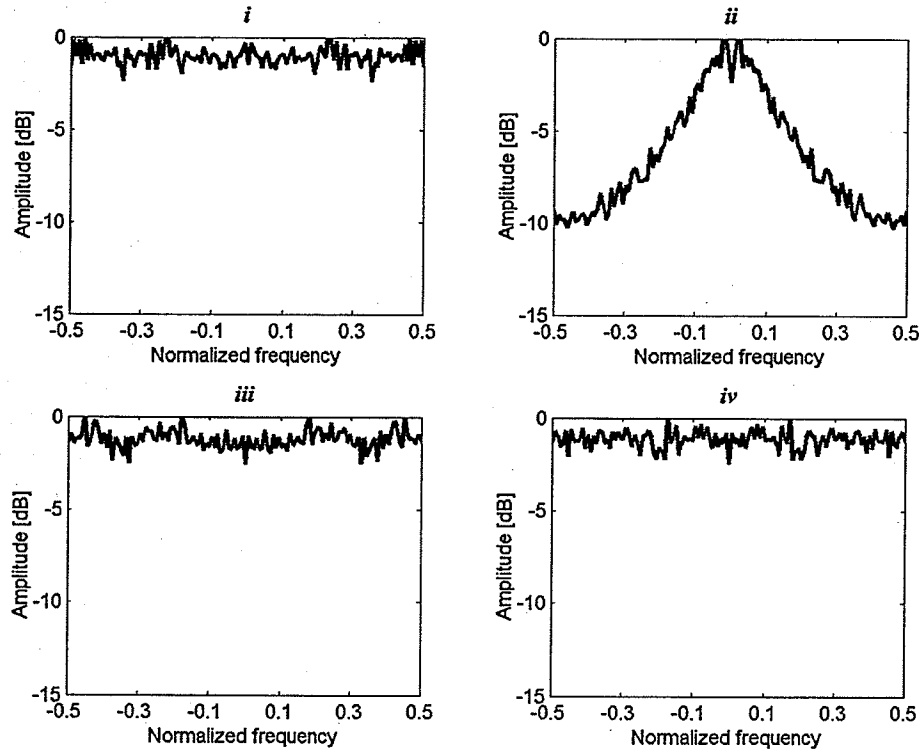


Fig. 3.3. Power spectra of selected chaotic maps.
i) logistic map; *ii)* Bernoulli map; *iii)* tent map; *iv)* quadratic map.

TABLE 3.1
Statistical and spectral properties of selected maps.

Map	Distribution	Histogram error	Sideline level	Power spectral density
Logistic	Arc Sine	1.8 %	$N^{-1/2}$	Uniform (White)
Bernoulli	Uniform	1.85 %	$N^{-1/2}$	Low pass (White-Pink)
Tent	Uniform	1.11 %	$N^{-1/2}$	Uniform (White)
Quadratic	Arc Sine	1.9 %	$N^{-1/2}$	Uniform (White)

3.1.3 Chaos quantification

In order to have a measurement of the “*amount of chaos*” generated with the iterated maps, a series of calculations were performed to obtain an insight on the signal’s complexity. These measurements can be used latter to classify the signals in terms of their chaotic properties. Figure 3.4 presents the *pseudo phase space* plots for the chaotic signals. The plots are obtained by plotting adjacent points x_n and x_{n+1} in a two-

dimensional space. The plot is not a true phase space representation because only one variable is described in the two axes. These plots show the deterministic nature of the signals by revealing their inner structure. No random signal will ever present a defined pattern in a phase space plot.

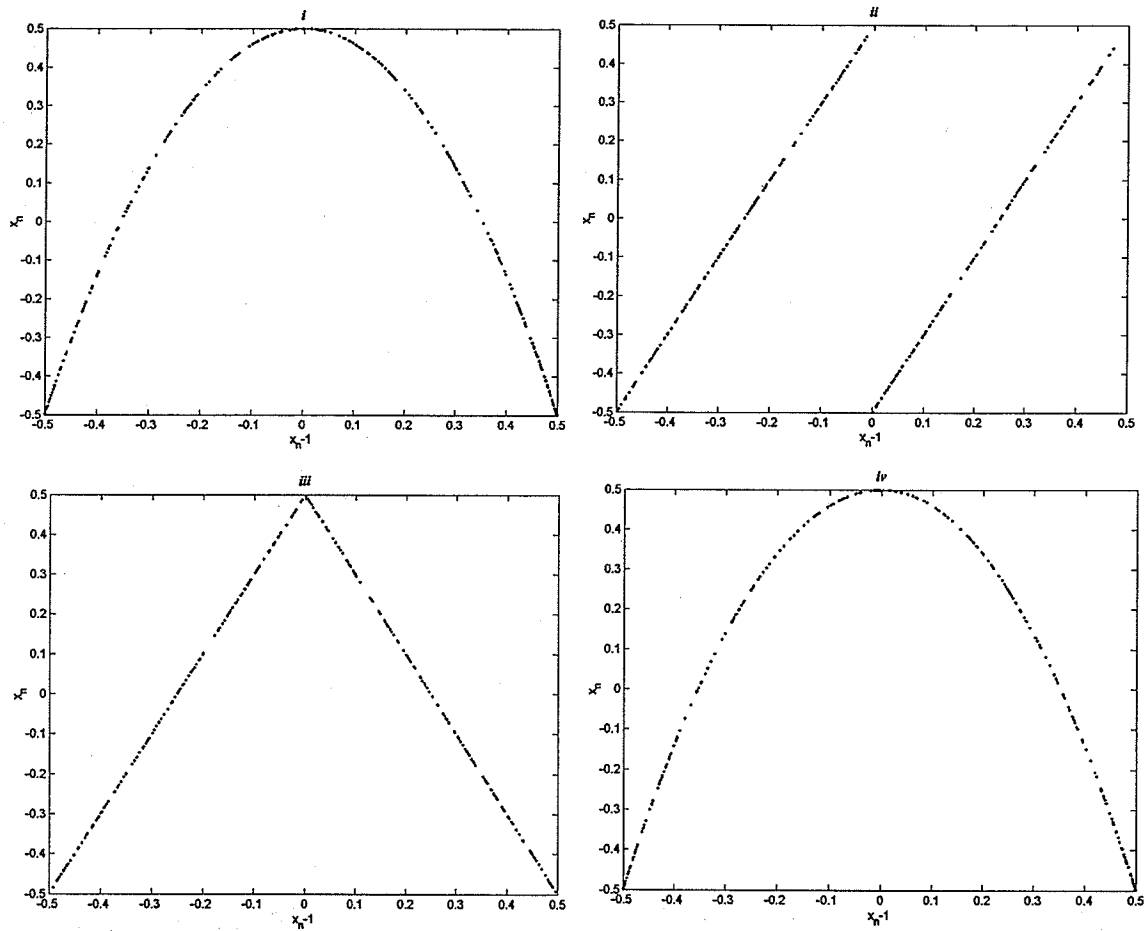


Fig. 3.4. Pseudo-phase space of chaotic sequences.
i) logistic map; ii) Bernoulli map; iii) tent map; iv) quadratic map.

3.1.3.1 Lyapunov exponent of chaotic signals

To characterize the signal's sensitivity to initial conditions, the Lyapunov exponent was calculated using equation (2-17). It is possible to obtain explicitly the value of the exponent for all maps. For the parameters selected in Table 2.1 all maps present a

divergence of close trajectories described by a Lyapunov exponent of $\ln(2)$ [7,p.192]. The result is obvious in the case of the Bernoulli and tent map, where the derivative of the map function is a constant equal to 2 (except for the discontinuity at 0), as confirmed by the plots in Figure 3.4. The same result is not so obvious for the logistic and quadratic maps; however it can be verified numerically by implementing equation (2-17).

3.1.3.2 Correlation dimension of chaotic signals

For completeness the signals were tested from an information perspective by comparing their fractal correlation dimension D_C . By using the definition of correlation dimension given in equation (2-22), it was found that realizations of the Bernoulli and tent maps had essentially the same correlation dimension. The logistic and quadratic maps had similar values, which are shown in Table 3.2. Notice that maps with uniform distribution have higher D_C dimensionality than maps that follow an arcsine distribution. This indicates that the distribution of the points in the map is the determining factor when computing the correlation dimension, rather than the spectral characteristics of the sequence. Figure 3.5 illustrates the log-log plots from which the correlation dimensions were obtained. The plots present the relation between the correlation sum C_k and radial size R_k , also known as *volume element* (VEL) [29,pp.29]. The slope m of such relation is the correlation dimension for that object. The largest the value of D_C is, the more complex the signal is. A random signal with uniform probability density function would have a correlation dimension close to 2 (i.e. similar to those values obtained for the Bernoulli and tent maps). This would indicate the signal is almost as complex as a surface [7], [29,Ch.2].

TABLE 3.2
Chaos quantification in selected maps.

Map	Correlation dimension	Lyapunov exponent
Logistic	1.8421	$\ln(2)$
Bernoulli	1.9594	$\ln(2)$
Tent	1.9519	$\ln(2)$
Quadratic	1.8427	$\ln(2)$

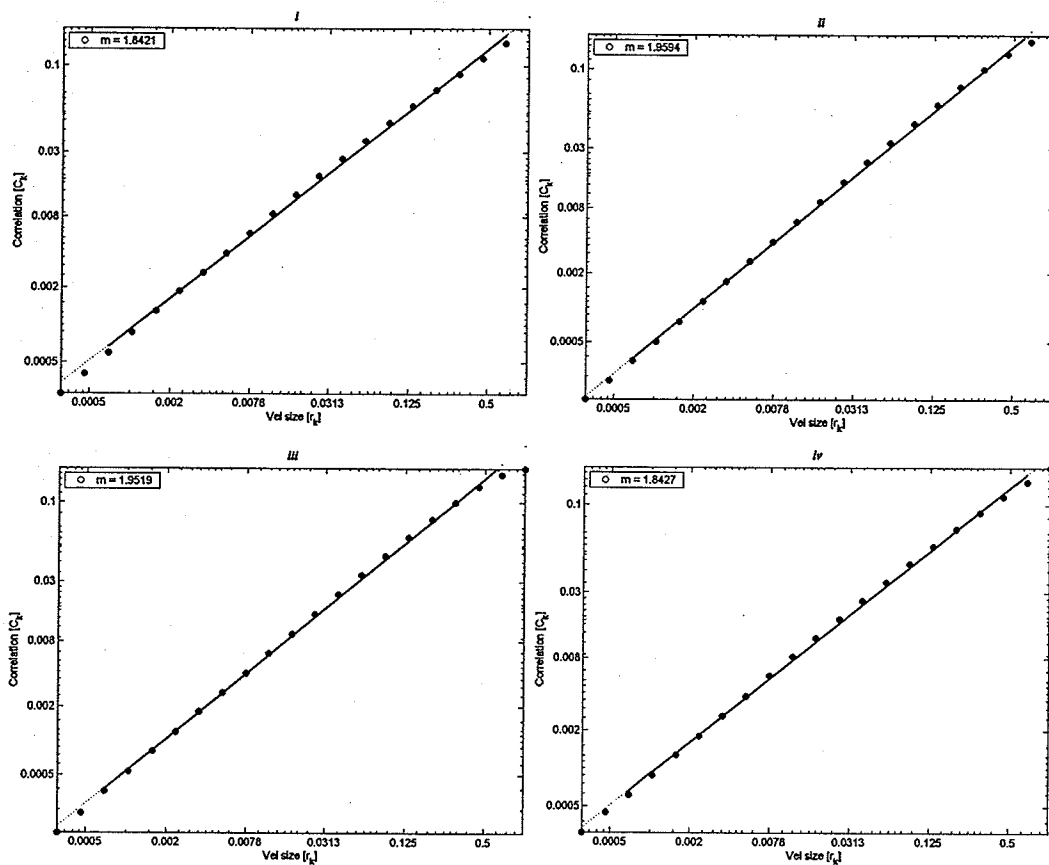


Fig. 3.5. Correlation dimension plots for selected chaotic sequences.
i) logistic map; *ii)* Bernoulli map; *iii)* tent map; *iv)* quadratic map.
 The slope m of the relation is considered the correlation dimension.

Table 3.2 presents chaos quantification based on the Lyapunov exponent and correlation dimension. From these results, as well as those presented in Table 3.1, is clear that the chaotic maps can be classified based on the probability density function of their trajectories and the correlation dimension. This division however does not prevent the four chaotic maps from having identical sensitivity to initial conditions. At the same time, the level of chaos does not seem to be affected by the spectral shape of the data sequence.

3.2 Analysis of CBFM signals

Let $x(n\Delta t)$ be the discrete version of a chaotic function $x(t)$ such that

$$x[(n+1)\Delta t] = x_{n+1} = g[x(n\Delta t)] \quad (3-4)$$

for $n = 0, 1, \dots$ where Δt represents the sampling interval and $g(\cdot)$ is a nonlinear map with range $[-1/2, 1/2]$. The sequence of samples $\{x_0, x_1, \dots, x_n\}$ generated by equation (3-4) exhibits fractal behavior, as shown in section 3.1.3.2. The initial condition x_0 is a random variable with probability density function $p(x_0)$, range $[-1/2, 1/2]$, zero mean, and variance σ_x^2 . Randomizing x_0 ensures that x_n is a stochastic process with stationary mean. The immediate objective is to produce an ergodic baseband FM signal with complex envelope

$$s(t) = A \exp [j2\pi KX(t)] \quad (3-5)$$

where A is the amplitude of the signal, K is its modulation index, and

$$X(t) = \int_0^{T_1} x(t) dt \quad (3-6)$$

Notice that $K \cdot x(t)$ is the instantaneous (i.e. momentary) frequency $f(t)$ of the signal $s(t)$. Given that the power of the FM signal is constant, the energy contained in the observation interval is $A^2 T_1$, spread over the frequency band

$$K x_{min} \leq f \leq K x_{max} \quad (3-7)$$

Consequently, applying equation (2-4) the range resolution is given by

$$\Delta R = \frac{C}{2\beta} = \frac{C}{2K} \quad (3-8)$$

The discrete version of the FM signal $s(t)$ is given by

$$\begin{aligned} s(n\Delta t) &= A \exp [j2\pi K X(n\Delta t)] \\ &= A \exp (j2\pi K \sum_{k=1}^n x_k \Delta t + j2\pi K x_0 \Delta t) . \end{aligned} \quad (3-9)$$

In order to avoid undersampling (i.e. aliasing) of the expression in equation (3-9), the sampling rate must satisfy the Nyquist criterion

$$f_s \geq 2K x_{max}. \quad (3-10)$$

Substituting $f_s = 2K x_{max}$ and $x_{max} = 1/2$ in equation (3-9) yields

$$s(n) = A \exp (j2\pi \sum_{k=1}^n x_k + j2\pi x_0). \quad (3-11)$$

According to the central limit theorem [34], $X(n)$ evolves into a Gaussian variable with zero mean and variance $(n+1)\Delta t \sigma_x^2$ for increasing n . The density function of $\cos[2\pi X(n)]$ converges to the arc-sine density [35]. Therefore, the density function of subsequent samples $\{\text{Re}[s(n+1)], \dots, \text{Re}[s(n+m)]\}$ will have the same density form and differ only in the variance.

Figure 3.6 presents the chaotic-based FM (CBFM) signals generated using equation (3-11). All sequences appear erratic, as expected due to the chaotic nature of the modulated signal (i.e. the message signal).

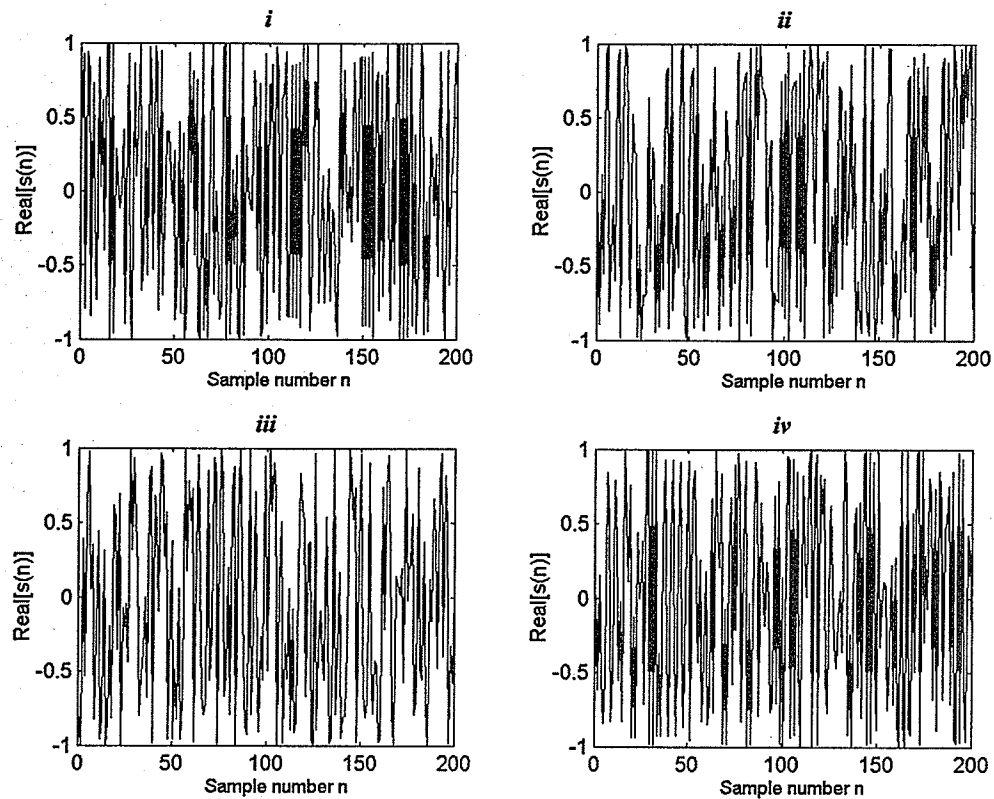


Fig. 3.6. CBFM signals.
i) logistic-based FM signal; *ii)* Bernoulli-based FM signal; *iii)* tent-based FM signal;
iv) quadratic -based FM signal.

3.2.1 Ergodicity of CBFM signals

The generated signals $\text{Re}\{s(t)\}$ were tested for ergodicity by comparing the histograms of single and multiple signal realizations as was done for the chaotic signals in section 3.1.1. Figure 3-7 illustrates the histograms of CBFM signals. The right plot shows the histogram of 100,000 values of a single realization of $\text{Re}\{s(n)\}$. Notice that the histogram takes on the shape of an arc-sine density. The left plots in Figure 3-7 presents the histogram of the 100th sample of 100,000 realizations of $\text{Re}\{s(n)\}$.

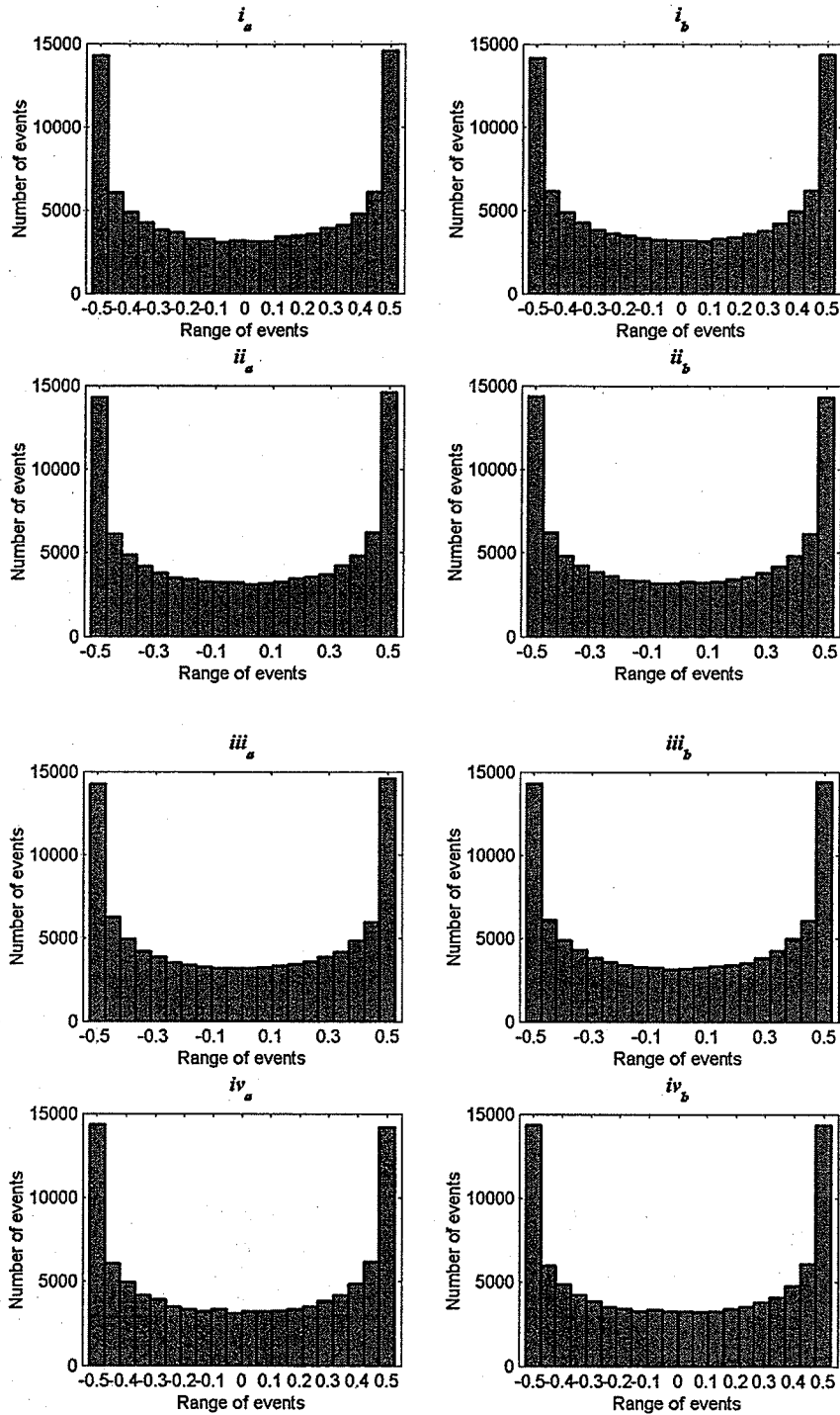


Fig. 3.7. Ergodicity on CBFM signals.
 Time (a) and ensemble (b) distributions of *i*) logistic-based FM signal; *ii*) Bernoulli-based FM signal; *iii*) tent-based FM signal; *iv*) quadratic-based FM signal.

Clearly, the time and ensemble sample distributions are similar, indicative of the ergodicity of the signals. Table 3.3 summarizes the statistical properties of the generated CBFM signals.

TABLE 3.3
Statistical properties of CBFM signals.

Map	Points distribution	Histogram error
Logistic-based FM	Arc Sine	1.59 %
Bernoulli-based FM	Arc Sine	1.42 %
Tent-based FM	Arc Sine	1.31 %
Quadratic-based FM	Arc Sine	1.46 %

3.2.2 Autocorrelation and power spectrum of CBFM signals

Let consider algebraic expressions of equation (3-4) that yield statistically independent samples with ergodic behavior and probability density function $p(x_n) = p(x_{n-1})$ for $n \geq 1$ [31]. The ergodic theorem guarantees that the sequence $s(n)$ is a stationary stochastic process [35]. Let $p(x_0, \dots, x_n)$ denote the multivariate density of the set (x_0, \dots, x_n) . Then the autocorrelation function of the CBFM signals is given by

$$\begin{aligned}
 R(m,n) &= E \{ s(n) \cdot s^*(n+m) \} \\
 &= E \{ A \cdot \exp[j2\pi(x_0 + \dots + x_n)] \cdot A \cdot \exp[-j2\pi(x_0 + \dots + x_{n+m})] \} \\
 &= A^2 E \{ \exp[j2\pi(x_0 + \dots + x_n) - j2\pi(x_0 + \dots + x_{n+m})] \} \\
 &= A^2 E \{ \exp[-j2\pi(x_{n+1} + \dots + x_{n+m})] \} \\
 &= A^2 \int p(x_0, \dots, x_{n+m}) \cdot \exp[-j2\pi(x_{n+1} + \dots + x_{n+m})] dx_0 \dots dx_{n+m} \quad (3-12)
 \end{aligned}$$

for $m > 0$.

Assuming that the samples are statistically independent,

$$p(x_0, x_1, \dots, x_{n+m-1}, x_{n+m}) = p(x_0) p(x_1) \dots p(x_{n+m-1}) p(x_{n+m}) \quad (3-13)$$

and equation (3-12) can be written as

$$R(m, n) = A^2 \int p(x_0) \dots p(x_{n+m}) \cdot \exp[-j2\pi(x_{n+1} + \dots + x_{n+m})] dx_0 \dots dx_{n+m}, \quad (3-14)$$

which further simplifies to

$$R(m, n) = A^2 \int p(x_{n+1}) \dots p(x_{n+m}) \cdot \exp[-j2\pi(x_{n+1} + \dots + x_{n+m})] dx_{n+1} \dots dx_{n+m}. \quad (3-15)$$

The above expression can be written in terms of the characteristic function

$$C_k(\alpha) = \int p(x_k) \cdot \exp[-j2\pi x_k \alpha] dx_k. \quad (3-16)$$

Then by combining equations (3-15), and (3-16) evaluated at $\alpha = 1$,

$$R(m) = A^2 \prod_{k=1}^m C_k(1) = A^2 C^m(1) \quad (3-17)$$

for $m > 0$. It is clear that $R(0) = A^2$.

Equation (3-17) relates the autocorrelation function directly to the probability density function of the modulated signal. The autocorrelation function $R(m)$ can be calculated for the two probability density functions that apply to selected chaotic maps.

Case 1. Uniform density: $p(x_n) = 1$ for $-1/2 \leq x_n \leq 1/2$.

This type of chaos can be generated via the Bernoulli and tent map. The characteristic function $C_k(\alpha)$ at $\alpha = 1$, is obtained as

$$C_k(1) = \int \text{rect}[-1/2, 1/2] \cdot \exp[-j2\pi x_k \alpha] dx_k = \text{sinc}(1/2 2\pi\alpha) \quad (3-18)$$

Thus,

$$C^m(1) = \text{sinc}^m(\pi) = \sin^m(\pi) / \pi^m \quad (3-19)$$

Equation (3-19) becomes 0 for $m \geq 1$. Therefore, the autocorrelation function for the maps with uniform distribution is a weighted discrete delta

$$R(m) = A^2 \delta(m). \quad (3-20)$$

Notice that the discrete Fourier transform of (3-20) yields a white spectral density over the interval $[0, f_s]$.

Case 2. Arc sine density: $p(x_n) = \frac{1}{\pi \sqrt{(1/2 + x_n)(1/2 - x_n)}}$ for $-1/2 \leq x_n \leq 1/2$.

This represents a situation of chaos generated via a logistic or quadratic map. For this case, it can be shown that [37]

$$C_k(1) = J_0(\pi) \quad (3-21)$$

This yield an autocorrelation of $s(t)$ given by

$$R(m) = A^2 [J_0(\pi)]^{|m|} \quad (3-22)$$

where $J_0(\cdot)$ is the ordinary Bessel function of zeroth order. From equation (3-22) it follows that the first sidelobe has a relative magnitude of 0.3042 (-10.4 dB). Subsequent sidelobes decay rapidly as the lag number m increases.

The autocorrelation results obtained for cases I and II clearly showed that the behaviour of the autocorrelation is dependent upon the choice of $p(x_n)$, which is directly related to the selected chaotic map. In fact such selection will also affect the shape of the corresponding spectrum. According to Woodward's theorem [35],[38] the normalized power spectral density of a wideband FM signal (baseband representation) can be roughly approximated by

$$S(f) \approx 2\pi A^2 p_x(2\pi f). \quad (3-23)$$

An interesting corollary to (3-23) is that the autocorrelation of the wideband signal $s(t)$ has approximately the shape of the characteristic function of $p_x(x)$. For instance, assuming uniform x in the range $[-\frac{1}{2}, \frac{1}{2}]$, equation (3-23) predicts a uniform (white) FM spectrum

$$S(f) = 2\pi A^2 \quad (3-24)$$

for $-\frac{1}{2} \leq f \leq \frac{1}{2}$. The inverse discrete-time Fourier Transform (IDFT) of equation (3-23) is the delta given in expression (3-20), which is associated with an uncorrelated random variable.

From the previous analysis one may expect that in the case of the uniform distribution $p(x)$, the estimate of $S(f)$ is approximately white over the band of interest and that the corresponding autocorrelation estimate is characterized by a narrow mainlobe and extremely low sidelobes. For the arc sine distribution, the power spectral density is unbounded near the edges of the frequency range. This may cause the estimate of $S(f)$ to exhibit high frequency spillover, which makes it susceptible to alias as the bandwidth of the stochastic process approaches the sampling rate. This has the potential of impacting the sidelobe structure of the autocorrelation estimate for small $|m|$. It is preferable then to limit the range of x , and hence its variance, so that the normalized sidelobe level of the autocorrelation estimate approaches the theoretical calculated value $[J_0(\pi)]^{|m|}$.

To verify the previous results, the CBFM signals were simulated and the autocorrelation and power spectrum were calculated for each FM signal. To achieve high range resolution, the autocorrelation of the FM signal must be characterized by a sharp mainlobe at the origin. An additional desirable feature is for the sidelobes of the autocorrelation to be shallow and die out rapidly with increasing time lags. Figure 3.8 shows both the time autocorrelation and ensemble autocorrelation of $s(n)$ for the four maps. The time autocorrelation was obtained by dividing a single signal realization of $N=1500$ samples into $M=50$ segments, performing the unbiased time-autocorrelation of each segment, and averaging the response of each delay bin (Figure 3.8, left side). In contrast, the ensemble autocorrelation was calculated by generating the time-autocorrelation of 50 signal realizations of 30 samples each, and averaging the response for each delay bin (Figure 3.8, right side). The initial condition x_0 was uniformly distributed between $-\frac{1}{2}$ and $\frac{1}{2}$. For the Bernoulli CBFM, the first sidelobe of the autocorrelation estimate appeared at $20\log(N^{-1/2})$ dB. In contrast, for the tent CBFM the first sidelobe was quite high at -7.5 dB. In the case of the logistic and quadratic CBFM, the first sidelobe was at the theoretical value of -10.4 dB. For large $|m|$, all five chaotic signal had sidelobes of the order of $N^{-1/2}$.

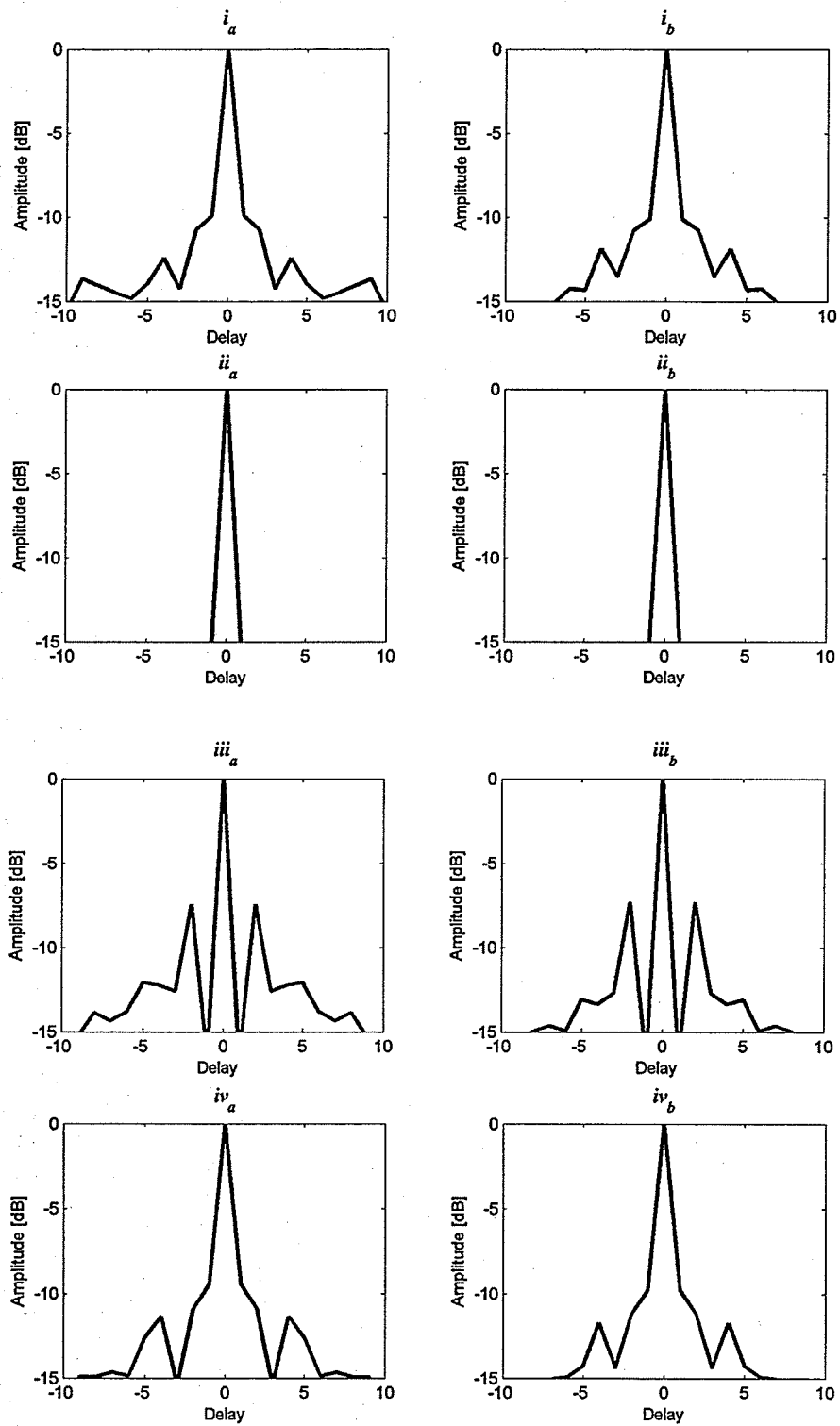


Fig. 3.8. Averaged autocorrelation of CBFM signals.

Time (a) and ensemble (b) autocorrelations of *i*) logistic-based FM signal; *ii*) Bernoulli-based FM signal; *iii*) tent-based FM signal; *iv*) quadratic-based FM signal.

Figure 3.9 shows the spectrum of $s(n)$ obtained via (3-3) for each map, averaging 100 realizations of the FM spectrum sampled at the Nyquist rate. As expected, the Bernoulli CBFM spectrum is close to the ideal white case. In contrast, the tent CBFM spectral density exhibits magnitude fluctuations over a 10 dB range. Figure 3.9 also shows that the logistic and quadratic CBFM spectra approximate an arc sine distribution near the centre of the spectral band. Similar behaviour was observed for the tent map.

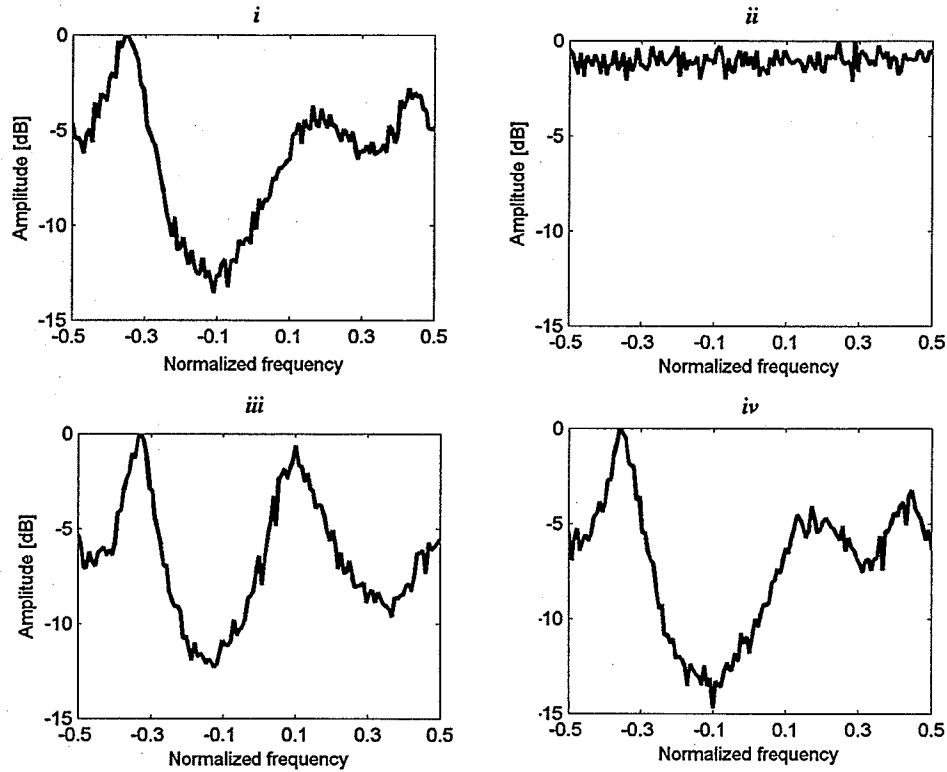


Fig. 3.9. Power spectra of CBFM signals.
i) logistic-based FM signal; *ii)* Bernoulli-based FM signal; *iii)* tent-based FM signal;
iv) quadratic -based FM signal.

3.2.3 Chaos quantification in CBFM signals

Similarly to the analysis done for the chaotic signals in section 3.1.3, the CBFM signals were tested to determine their chaotic behaviour. Figure 3.10 shows the two-dimensional phase-space reconstruction obtained for each FM signal. Contrary to the chaotic map signals, the CBFM signals do not present a clear pattern when reconstructed in this space,

except for the Bernoulli CBFM. Even though the lack of pattern is expected in the plots due to the complex relation between iterates S_n and S_{n+1} as given by equation (3-11), the result was expected to be consistent in all maps. The phase-space plot suggests that the Bernoulli CBFM trajectories may be those of a chaotic process projected to a low dimensional space.

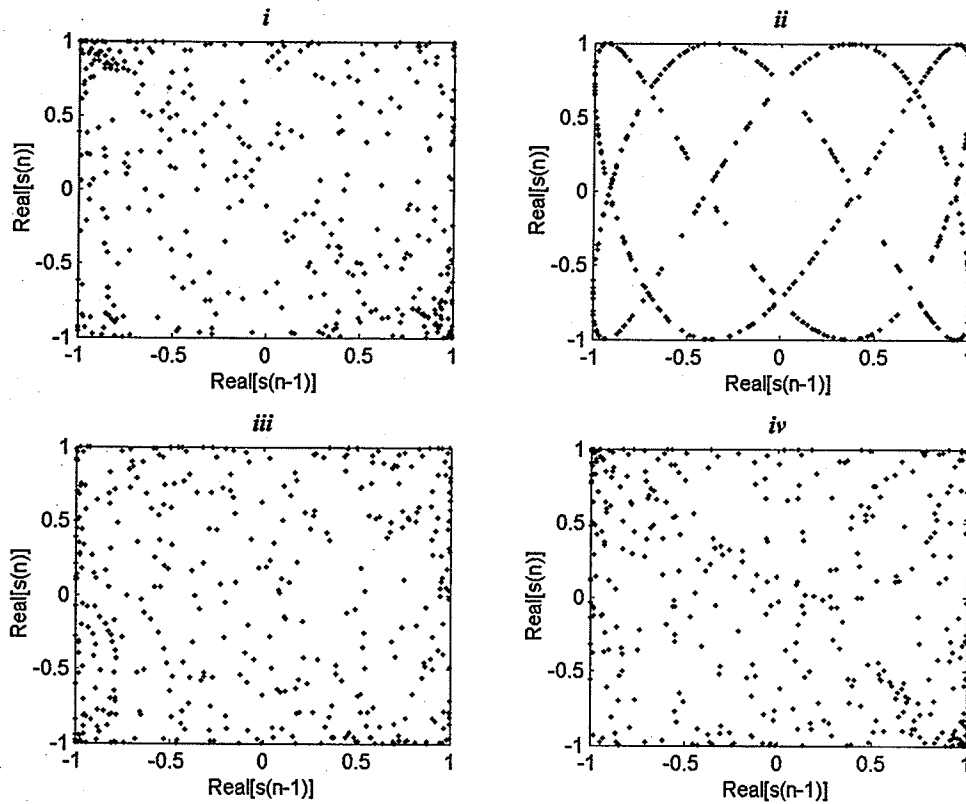


Fig. 3.10. Two-dimensional pseudo-phase space representation of CBFM signals.
i) logistic-based FM signal; *ii)* Bernoulli-based FM signal; *iii)* tent-based FM signal;
iv) quadratic -based FM signal.

To further investigate this possibility, a three-dimensional phase-space of the Bernoulli and tent maps is presented in Figure 3.11. It is clear that to perfectly reconstruct the trajectory of the CBFM, a higher dimensional space is required. By comparison, equations (2-23) – (2-26) present a clear relation between successive points x_n and x_{n+1} , whereas in the CBFM signal described by equation (3-11) this relationship has the form of

$$s_{n+1} = \exp(j2\pi x_{n+1})s_n \quad (3-25)$$

which suggests that the space spaces dimension is a function of the iteration number n . In any case the difference in the result obtained from the Bernoulli based FM signal, with respect to the rest of the CBFM signals is remarkable.

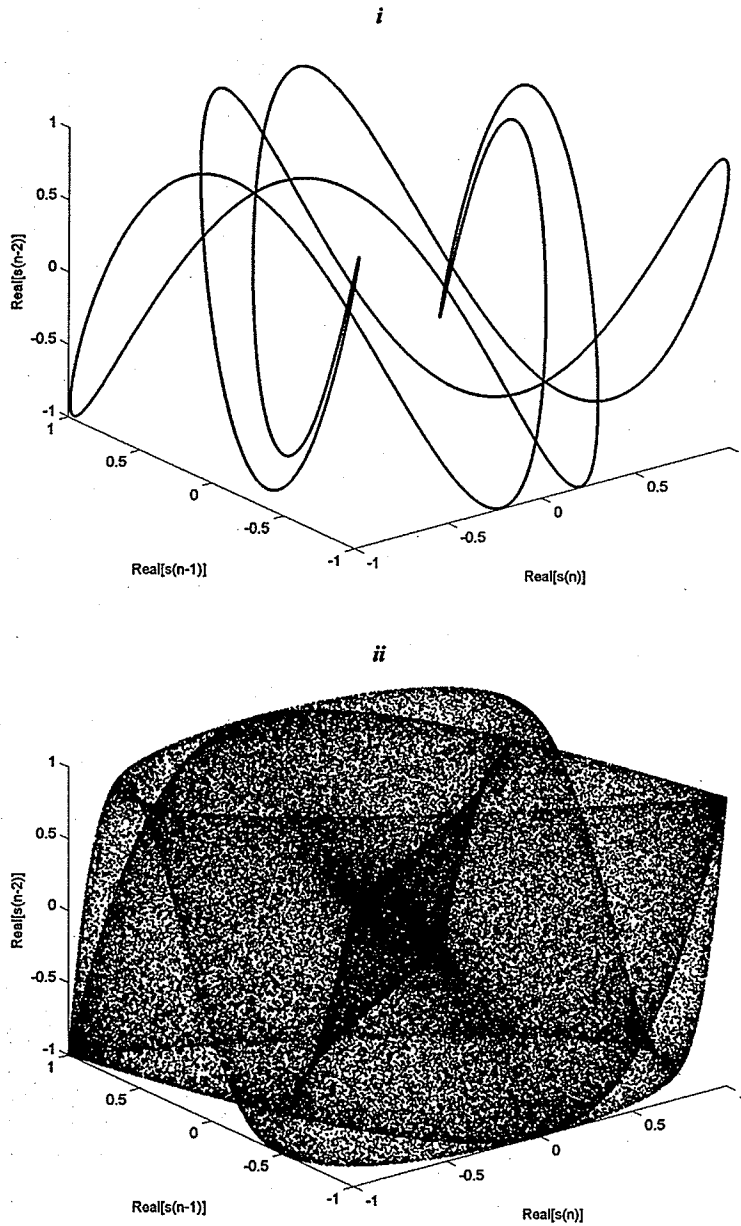


Fig. 3.11. Three-dimensional pseudo-phase-space representation of CBFM signals.
i) Bernoulli-based FM signal; *ii)* tent-based FM signal

3.2.3.1 Lyapunov exponent of CBFM signals

To characterize the divergence of close trajectories for each CBFM signal, the Lyapunov exponent was calculated numerically. The exponent was obtained from a logarithmic plot of the differences described by equation (2-18). The value for λ_1 can be estimated from the slope m of a semi-logarithm plot. The Bernoulli CBFM case is illustrated in Figure 3.12. The calculated Lyapunov exponent values are summarized in Table 3.4. The results suggest that the logistic, tent, and quadratic-based FM signals are random and not chaotic, because the Lyapunov exponent of such signals is 0 (i.e. pure random signals result in $\lambda_1=0$). This indicates that nearby trajectories does not diverge exponentially as the time index n increases, but it remains constant in average at any time. Yet again the Bernoulli-based FM signal presents a different behaviour, and a positive Lyapunov exponent, suggesting chaotic behaviour.

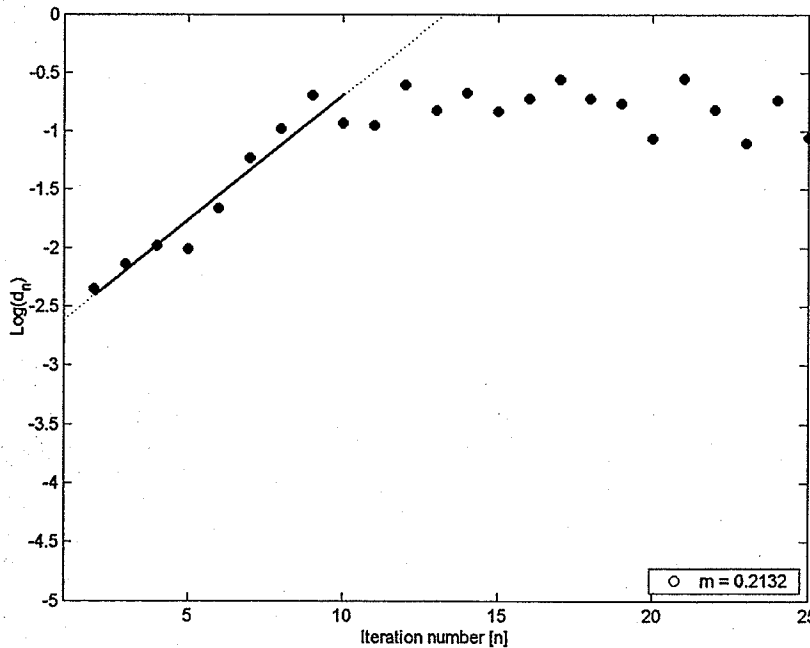


Fig. 3.12. Logarithmic plot of the divergence of close trajectories and Lyapunov exponent estimation in Bernoulli-based FM signal.

3.2.3.2 Correlation dimension of CBFM signals

For completeness and to further determine the level of complexity present in the CBFM signals, the corresponding correlation dimensions values were estimated. The results are shown in Table 3.4. All signals presented practically the same D_C value, which is accounted by a common probability density function common for all CBFM signals. Notice how the values are similar to those obtained for chaotic signals with an arc-sine distribution (i.e. logistic and quadratic maps) in Table 3.2.

TABLE 3.4
Chaos quantification for CBFM signals

Signal	Lyapunov exponent (app.)	D_C value (app.)
Logistic CBFM	0	1.832
Bernoulli CBFM	0.2132	1.829
Tent CBFM	0	1.831
Quadratic CBFM	0	1.828

3.3 Analysis of random FM signal

Because of the obvious similarity between chaotic signals and noise, a comparison between CBFM signals and a random FM signal is mandatory. The analysis in section 3.2 was also performed for a theoretical FM signal generated with random noise. In this case the input to the FM modulator is a random signal with Gaussian density function.

3.3.1 Autocorrelation and power spectrum of random FM signal

Let recall from equation (3-17) that the autocorrelation function is directly related to the probability density function of the message signal, and that for the Gaussian noise case the probability density function is given by

$$p(x_n) = \frac{1}{\sqrt{2\pi\sigma_x^2}} \exp\left[-\frac{x_n^2}{2\sigma_x^2}\right]. \quad (3-26)$$

The random variable x_n in equation (3-26) is not bounded, so $\sigma_x^2 < \frac{1}{2}$ is used to limit the spread of x and to avoid aliasing. The characteristic function (3-16) for $\alpha = 1$ is [35];

$$C(1) = \exp\left[-\frac{(2\pi\sigma_x)^2}{2}\right]. \quad (3-27)$$

From equation (3-17), it is easy to show that the autocorrelation of the Gaussian FM (GFM) signal is given by

$$R(m) = A^2 \exp\left[-\frac{(2\pi\sigma_x)^2 |m|}{2}\right] \quad (3-28)$$

which decays exponentially with m . Figure 3.1.3 shows and confirms equation (3-28). These plots are the time and ensemble autocorrelation of the GFM signal $s(n)$. The time

and ensemble autocorrelation were obtained with the same procedure used for the CBFM signals in section 3.2.2. Notice that the time and ensemble autocorrelations are almost identical for the GFM case; however the width of the mainlobes are wider than those of the CBFM signals. This will result in a poorer resolution capability for radar imaging.

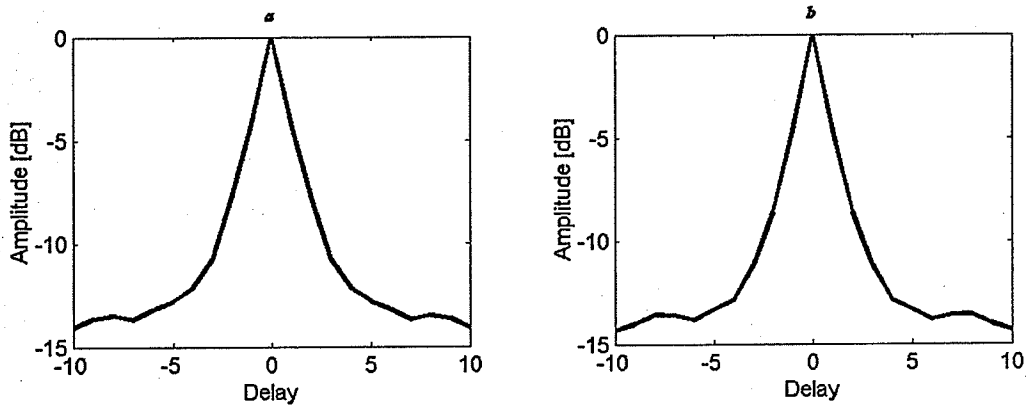


Fig. 3.13. Average autocorrelation of GFM signal.
Time (a) and ensemble (b) autocorrelations

In the case of GFM, the spectrum obeys Woodward's theorem and presents a Gaussian bell shape that tapers down at a rate that depends on σ_x^2 . The spectrum, calculated via equation (3-3), is shown in Figure 3.14.

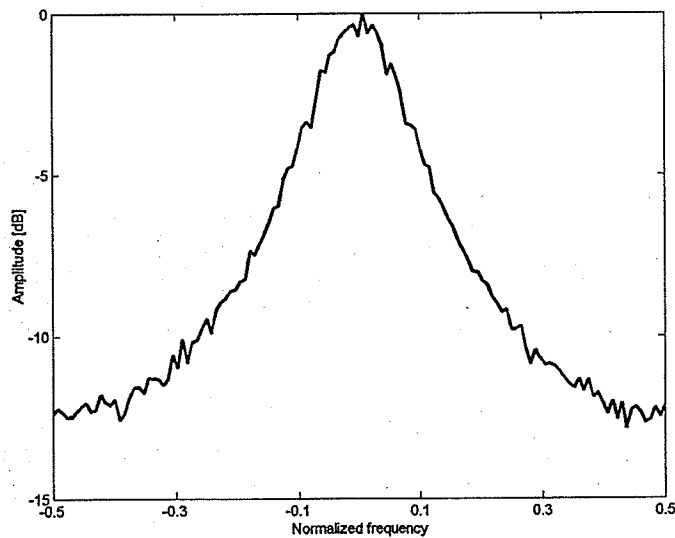


Fig. 3.14. Calculated power spectral density of GBFM signal.

3.3.2 Chaos quantification in random FM signal

It is a well known fact that the GFM signal is not a chaotic waveform, but a random signal. To further illustrate that property and in order to compare the results to those obtained with chaotic and chaotic-based signals, the plot in Figure 3.15 presents the pseudo-phase space reconstruction for the random FM signal. The random distribution of points is evident. Unlike the cases for chaotic and the Bernoulli-based FM signal, no pattern (other than an arcsine distribution characteristic of an FM signal) is present in the phase space plot.

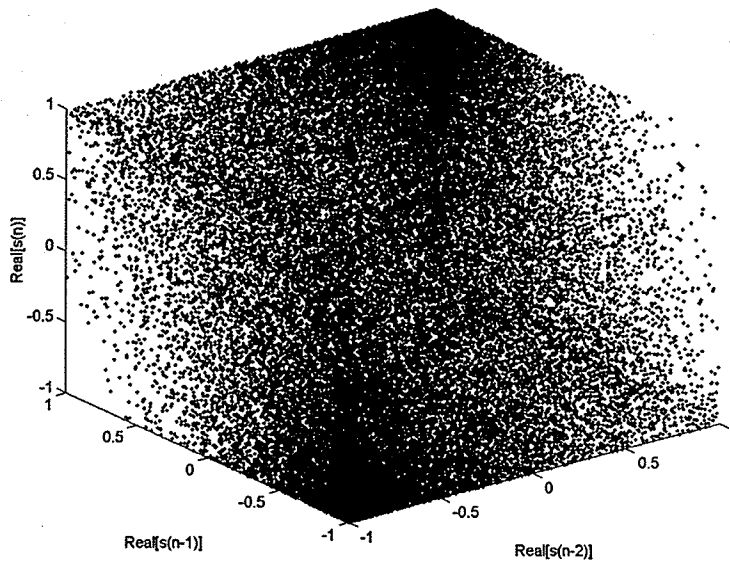


Fig. 3.15. Three-dimensional pseudo-phase space representation of GFM signal.

3.3.2.1 Lyapunov exponent of random FM signal

Similarly, the characteristic Lyapunov exponent of the random FM signal was estimated using equation (2-18). As it was expected, the resulting value is zero. This indicates that nearby trajectories do not diverge exponentially as the time index n increases, but it remains constant in average at any time. The absence of a positive Lyapunov exponent also indicates that the signal is not chaotic in the sense that it is not sensitive to initial conditions.

TABLE 3.5
Chaos quantification for GFM signal

Signal	Lyapunov exponent (app.)	D_C value (app.)
GFM	0	1.8375

3.3.2.2 Correlation dimension of random FM signal

Finally, a calculation of the correlation dimension gave an insight of the “level of complexity” of the random FM signal. The D_C value was calculated from the logarithm plot in Figure 3.16. The calculated value for the correlation dimension of the GFM signal was 1.8375, which is very close to the values obtained for the CBFM signal. This result indicates that all signals have the same amount of complexity, from an information point of view.

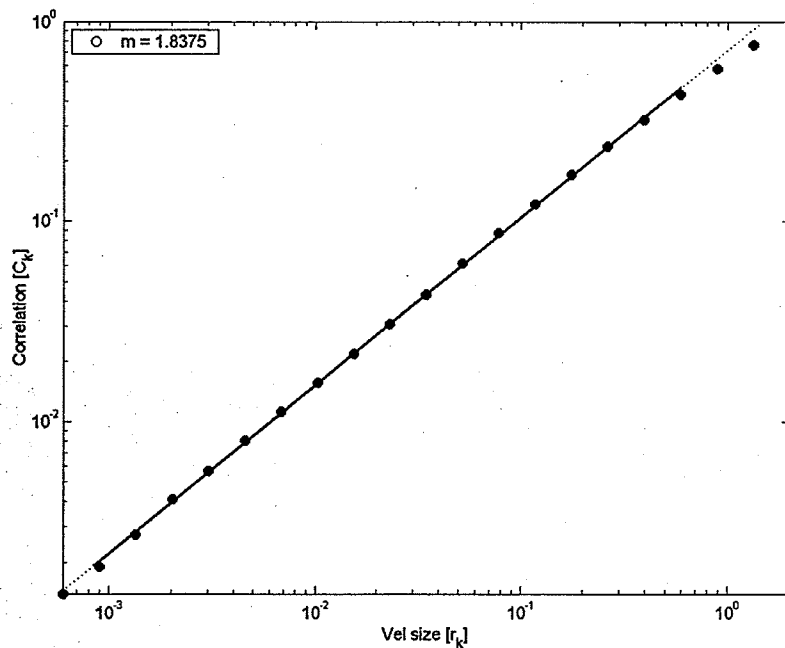


Figure 3.16. Correlation dimension plot of GFM.

Chapter 4

Results and evaluation

4.1 Ambiguity functions

The ambiguity function was used in this section as a tool to evaluate the performance of the chaotic and CBFM signals in terms of their capability to resolve target and clutter scatters in the range and velocity dimensions. In order to more precisely estimate the signals capabilities in terms of radar imaging resolution, an ensemble average of the discrete ambiguity function $\chi(m, \omega)$ [39] was calculated for all the chaotic and CBFM signals:

$$E \{ \chi(m, \omega) \} \approx 1/M \sum_{i=1}^M \sum_{n=0}^N [s_i(n) \cdot s_i^*(n+m) \cdot e^{j\omega n}] \quad (4-1)$$

where m is the lag index, N is the total number of samples in the signal, M is the number of signal realizations, ω is the Doppler angular frequency stepped in increments $\Delta\omega =$

$$\frac{2\pi}{N}$$

4.1.1 Ambiguity functions of chaotic signals

Figure 4.1 shows the ambiguity functions of the chaotic maps listed in section 2.5. In each instance, the result presented is the average of the ambiguity surface obtained by processing $M=100$ signal realizations. The ambiguity surface of each chaotic map resembles the ideal discrete delta except for a plateau of self-noise. Notice that each surface has a prominent peak emerging from the plateau with minor sidelobes off the main axes. For all cases, except the Bernoulli map, the sidelobes in the range direction are non-existent. The Bernoulli case presents higher sidelobes attributed to the spectral characteristic illustrated in Figure 3-3.

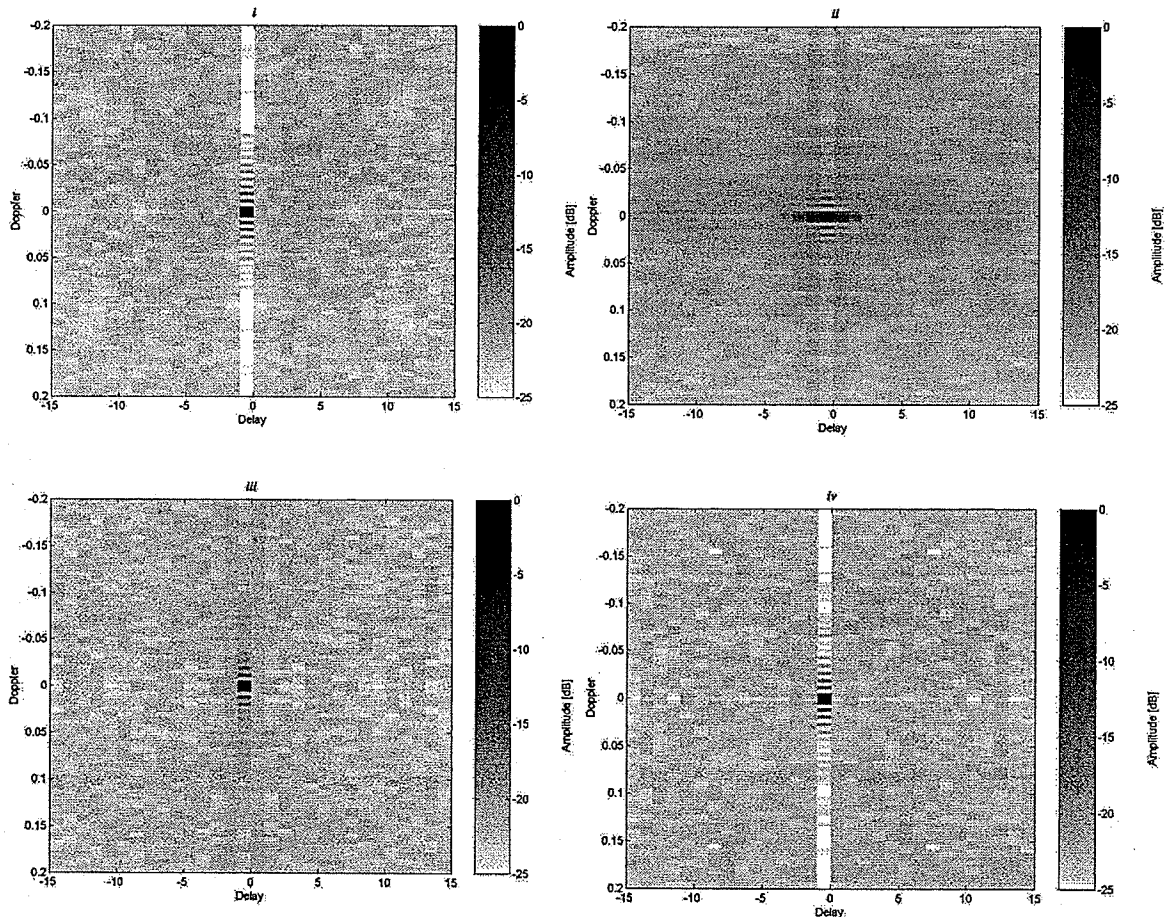


Fig. 4.1. Ambiguity surfaces of chaotic signals.
i) logistic map; *ii)* Bernoulli map; *iii)* tent map; *iv)* quadratic map.

4.1.2 Ambiguity function of CBFM signals

The ambiguity surface of each of the four CBFM also resembles the discrete delta except for a plateau of self-noise on which it rests. Figure 4.2 shows the resulting ambiguity surfaces. The location of the spurious sidelobes depends on the initial random phase of the chosen map. On average, sidelobes on the range-Doppler plane have a relative magnitude of $10\log_{10}(1/N)$ with respect to the main peak. For the Bernoulli CBFM signal, the sidelobes along the range delay axis are practically nonexistent. In the case of the tent CBFM, the highest range delay sidelobes occur at -7.5 dB. For all cases, including the logistic and quadratic CBFM signals, the behaviour of the sidelobes on the range delay axis near the origin is that of $|R(m)|^2$.

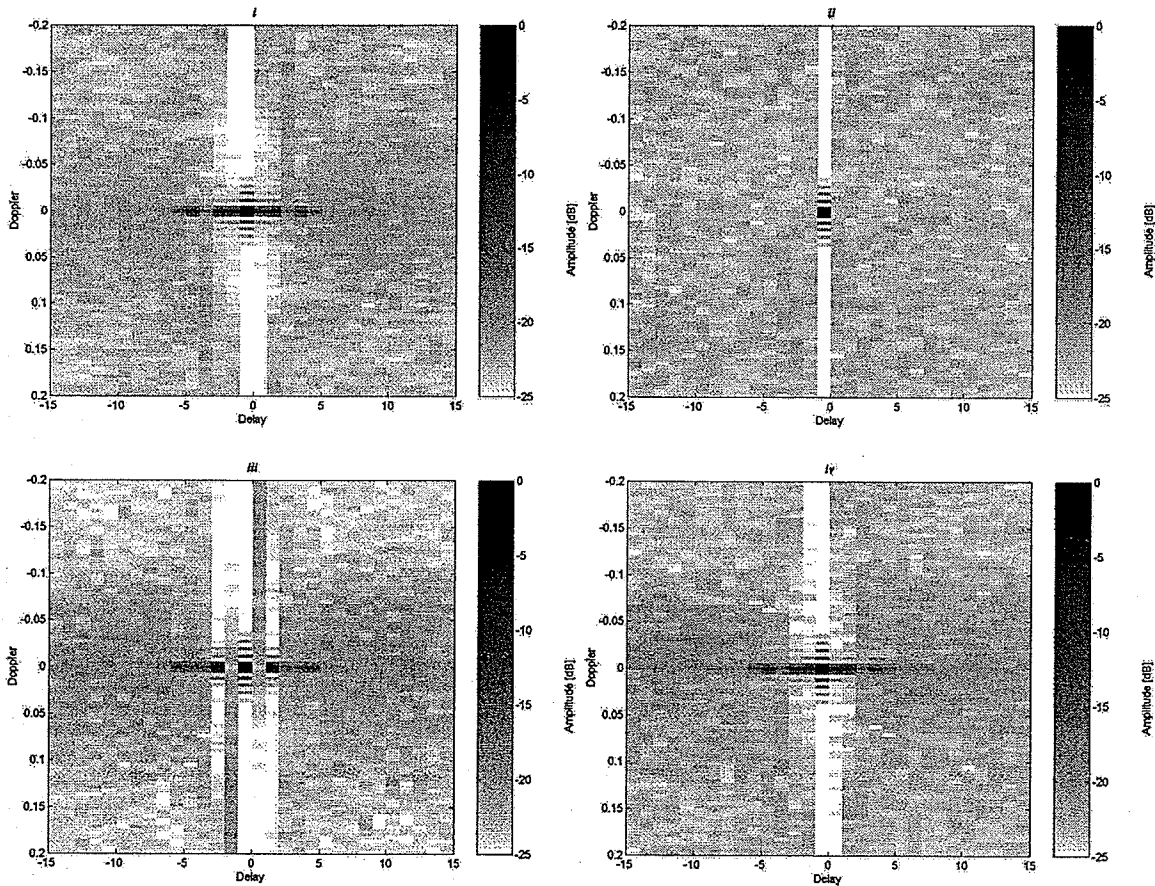


Fig. 4.2. Ambiguity surfaces of CBFM signals.
i) logistic-based FM signal; *ii)* Bernoulli-based FM signal; *iii)* tent-based FM signal;
iv) quadratic-based FM signal.

Along the Doppler axis, all the surfaces showed in Figures 4.1 and 4.2 feature sidelobes that match the spectrum of a boxcar window envelope. The sidelobes adjacent to the main response peak at -13dB can be easily lowered via windowing. However this would result in a wider mainlobe that decreases the Doppler precision.

From the analysis and results presented in Chapter 3 and section 4.1, it can be said that the use of chaotic and CBFM signal for radar imaging is feasible and even advantageous. An ideal signal for radar imaging is a signal with infinite bandwidth and whose ambiguity function is the delta function in the delay-Doppler plane. The chaotic and CBFM signals were proven to closely approximate these ideal characteristics. When dealing with the chaotic signals, it was demonstrated that the maps generate wideband spectrums and delta-like autocorrelation functions that also result in a delta-like ambiguity function. From the results in this project, it was clear that the sequence generated from the logistic, tent, and quadratic maps present near-optimal characteristic for radar imaging. The results obtained by using the Bernoulli map were not as remarkable as the ones obtained from the rest of the maps. The analysis in this investigation showed that the Bernoulli map has a pink noise (e.g $P(f) = 1/f$) frequency representation that makes it unique among the rest of the studied maps, even though the chaotic parameters (e.g. correlation dimension and Lyapunov exponent) were similar to the ones obtained for the rest of the maps.

The analysis and experimentation in this thesis proved that the CBFM signals also produced nearly ideal results in the spectral, autocorrelation and ambiguity function context. For a practical radar signal generation, it was preferred to work with FM signals because of their ease of generation and transmission. An FM signal allows an easier bandwidth control and in consequence, antenna design and power conservation. To convert the discrete time chaotic maps into a more suitable way of radar imaging without loosing the ideal characteristic presented by the chaotic signals, the chaotic sequences can be input to an FM modulator and a chaotic-based FM signal with chaotic instantaneous frequency can be created.

Comparative results of the CBFM signals proved that the Bernoulli-based signal, outperformed the logistic, tent, and quadratic cases, and was the only waveform that preserved the chaotic nature of the un-modulated chaotic signal. In other words, the

signal, although modulated, shows as pattern in the phase space and has a positive Lyapunov exponent confirming the chaotic behaviour of the Bernoulli CBFM signal. Because of the uniqueness of the Bernoulli CBFM signal, and its closeness to the ideal properties desired in a radar imaging context, a more detailed characterization was performed and the results are presented in the next sections.

4.2 Multipath performance of Bernoulli CBFM

Radar systems often suffer the adverse effects of multipath propagation. This phenomenon occurs when the received echo contains components which have traveled from the transmitter to the target and back to the receiver via multiple propagation paths with different delay times. The reflection of radar signals from the ground can have a number of effects on target detection and tracking accuracy. Multipath propagation can be specially destructive in cases like ground penetrating radar (GPR), where the antenna is very close to the ground and the arriving signal can be sensed by the antenna after it has been reflected several times by the ground or nearby rocks. Figure 4.3 illustrates two simplified scenarios of multipath propagation in radar and GPR.

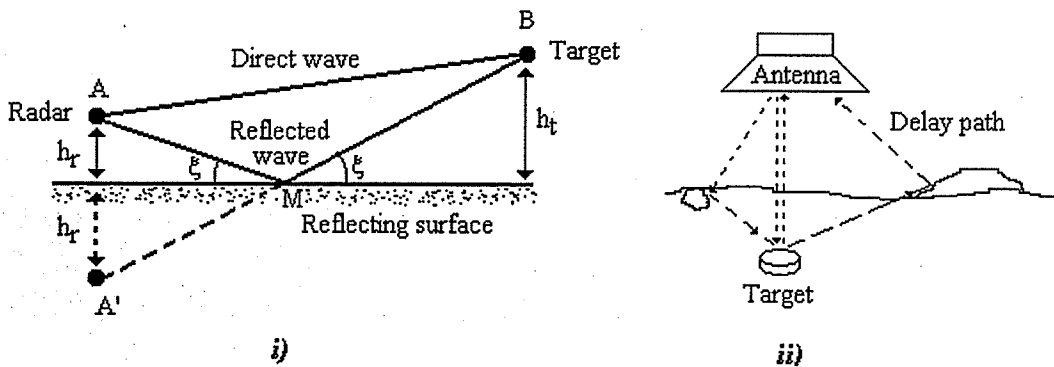


Fig. 4.3. Multipath scenarios.
i) Radar system; ii) Ground penetrating radar.

Diagram *i)* in Figure 4.3 shows that the energy radiating from the antenna reaches the target via two separate paths. One is the direct line-of-sight path from points A to B in the diagram and the other is the path reflected from the surface of the ground traveling points A-M-B. An echo arrives at the radar along the same two paths. The magnitude of the resultant echo signal will depend on the amplitudes and relative phase differences

between the direct and the reflected path. The reflection coefficient from the surface may be considered as a complex quantity $\rho e^{j\psi}$. The real part ρ describes the change in amplitude, while argument ψ describes the phase change in the reflected signal.

The direct method to avoid multipath errors is to use an antenna with a sufficiently narrow beam width that it does not illuminate the surface or any other object except the target of interest. This requires a very large antenna that can generate a directional beam. For very short pulses it is possible to separate the direct return and the delayed multipath return. However, this is often not practical, as the range resolution needed to separate the returns requires the use of a few nanoseconds pulse width. The pulse echo at the shorter range is the direct signal and corresponds to the true target range. The echo at a longer range is the scattered signal and appears as a ghost target. In some applications the appearance of these false targets is a serious problem, but in others, the time separation between the two signals can be used to measure the altitude of the target [1,p.502]. A more practical solution is the use of a signal that presents frequency agility. A fast change in frequency alters the phase relationship between the direct and the reflected signals. The constant change in frequency avoids the signal spectrum to be cancelled.

For wideband signals, multipath propagation results in a rapid fading of the received signal envelope and a spread in Doppler shift in the received spectrum [40,p.535]. The effect of multipath propagation can be estimated if there is a characterization of the impulse response of the transmission channel. If the multipath channel is assumed to be a bandpass channel, the received complex envelope of the signal $\tilde{r}(t)$ can be expressed as,

$$\tilde{r}(t) = \frac{1}{2} \int_{-\infty}^{\infty} \tilde{s}(t-\tau) \tilde{h}(\tau;t) d\tau \quad (4-2)$$

where $\tilde{s}(t)$ and $\tilde{h}(\tau;t)$ are the complex envelopes of the transmitted signals and the channel impulse response, respectively. For analytical purposes, and because the received signal in a multipath channel consists of a series of attenuated, time-delayed phase shifted replicas of the transmitted signal, the baseband impulse response of a multipath channel can be expressed as

$$\tilde{h}(\tau; t) = \sum_{i=0}^{N-1} a_i(\tau; t) \cdot \exp[j (2\pi f_c \tau_i(t) + \phi_i(\tau; t))] \cdot \delta(\tau - \tau_i(t)) \quad (4-3)$$

where $a_i(\tau; t)$ and $\tau_i(t)$ are the real amplitudes and excess delays of the i^{th} multipath component at time t , respectively. The phase term ϕ_i in equation (4-3) represents the phase shift due to free space propagation of the i^{th} multipath component plus additional phase shifts encountered in the channel. For short periods of time (at least the duration of the signal transmission and reception) the channel h can be model as a linear time invariant system or at least considered wide sense stationary over this scale. Then the channel impulse response may be simplified as

$$\tilde{h}(\tau) = \sum_{i=0}^{N-1} a_i \cdot \exp[j \theta_i] \cdot \delta(\tau - \tau_i). \quad (4-4)$$

The impulse response $\tilde{h}(\tau)$ may be modeled as a zero-mean complex Gaussian process. Because the envelope $|\tilde{h}(\tau)|$ is Rayleigh distributed, the channel is referred as a *Rayleigh fading channel* [41,p.172]. The Rician distribution is observed when, in addition to the multipath components, there exists a direct path between the transmitter, the target and the receiver (i.e., a term without any random phase needs to be added to equation (4-4)). In such case the channel is referred as a *Rician fading channel* [41,p.173].

To evaluate the multipath performance of the Bernoulli CBFM signal, a Rician fading channel was used to characterize radar environments like the ones shown in Figure 4.3. In those cases it is assumed that there is a direct line of sight from the radar to the target and additional multipath propagations with longer delays superimpose to the direct signal. Several parameters were considered during the multipath analysis. The effect of the bandwidth of the transmitted signal, the number of extra paths in the transmission and the amplitude of the directly reflected signal were varied during the simulations. Figure 4.4 presents the averaged cross-correlation functions of the transmitted and received signal, when the originally transmitted signal is a Bernoulli CBFM signal bandpass filtered at cut-off normalized frequencies of 0.05 and 0.45 times the sampling frequency, and transmitted through a Rician fading channel. The signal was bandpass filtered to

represent a more realistic situation in which it is not possible to occupy the complete signal spectrum. This limitation is evident because any electronic equipment will be affected by interference at the moment a radar survey is performed. The filtration also allows controlling the bandwidth of the signal and will facilitate an unbiased comparison with other bandlimited signals (e.g. linear FM chirp). The cross-correlation function was obtained by first transmitting 100 different Bernoulli CBFM signals over 100 different Rician fading channels, calculating the cross-correlation with the received signals and then calculating the average of these correlations bin by bin. Figure 4.4 shows the averaged cross-correlations results for different length fading channels. The distinct lengths represent the different number of multiple paths present in the channel.

The effect caused by the signal traveling longer paths is clearly shown by the correlations in Figures 4.4. The delayed replicas of the signal cause the correlation to present a main peak at zero delay and a constant value during the extended time the replicas are arriving to the receiver. Even though multipath propagation causes the level of the sidelobe to rise, the main peak is perfectly detectable and no ambiguities appear in the waveform correlation.

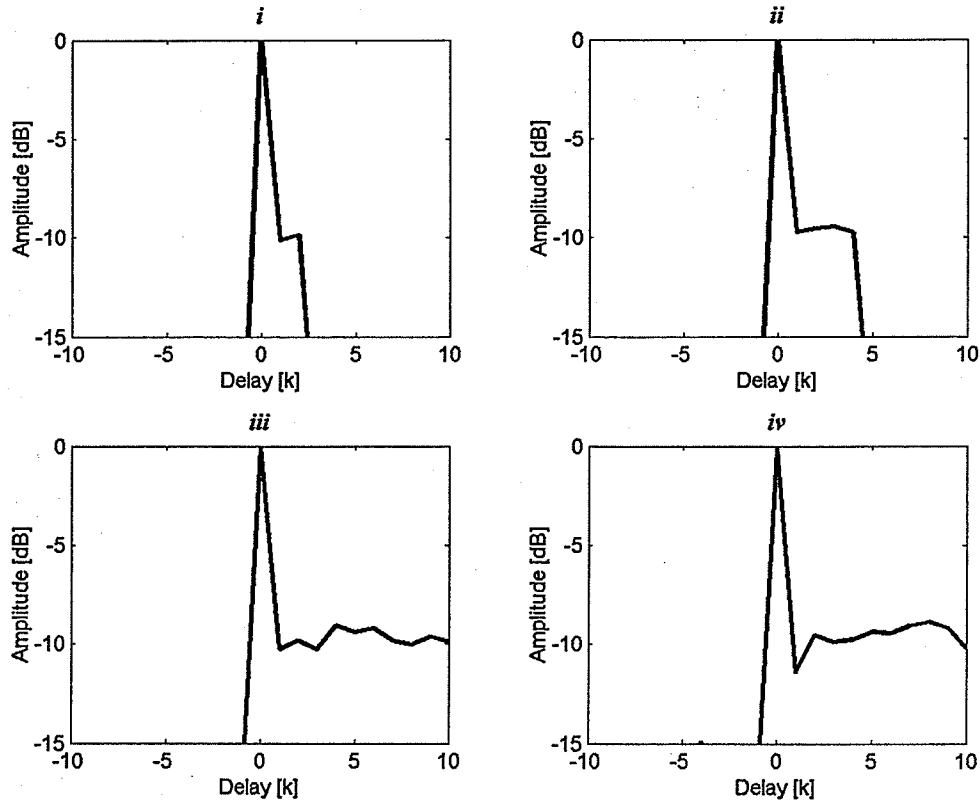


Fig. 4.4. Performance of Bernoulli CBFM in multipath environment.
 Averaged correlations between transmitted and received bandlimited CBFM signal
 in a *i*) two paths; *ii*) four paths; *iii*) twelve paths; *iv*) twenty five paths scenario.
 Cut-off frequencies: [0.05 0.45] of f_s , Direct reflection coefficient: 0.7.

Figure 4.5 illustrate the effect of the direct reflection coefficient in a radar detector operating in a four paths environment. The direct reflection coefficients accounts for the percentage of the signal received through the direct path between the radar antenna and the target. The remaining percentage is distributed among the 4 indirect paths. The averaged cross-correlations in Figure 4.5 were obtained applying the same methodology used in Figure 4.4, but un this case the varying paramater been the reflection coefficient.

The variation of the reflection coefficient has a great impact in the received signal detection and information extraction. From the plots in Figure 4.5, it can be seen that when the value of the coefficient is lowered, the main peak becomes less distinguishable until it reaches a point where the delayed signal that traveled through other paths can mask the direct wave. This effect can be observed in Figure 4.5.

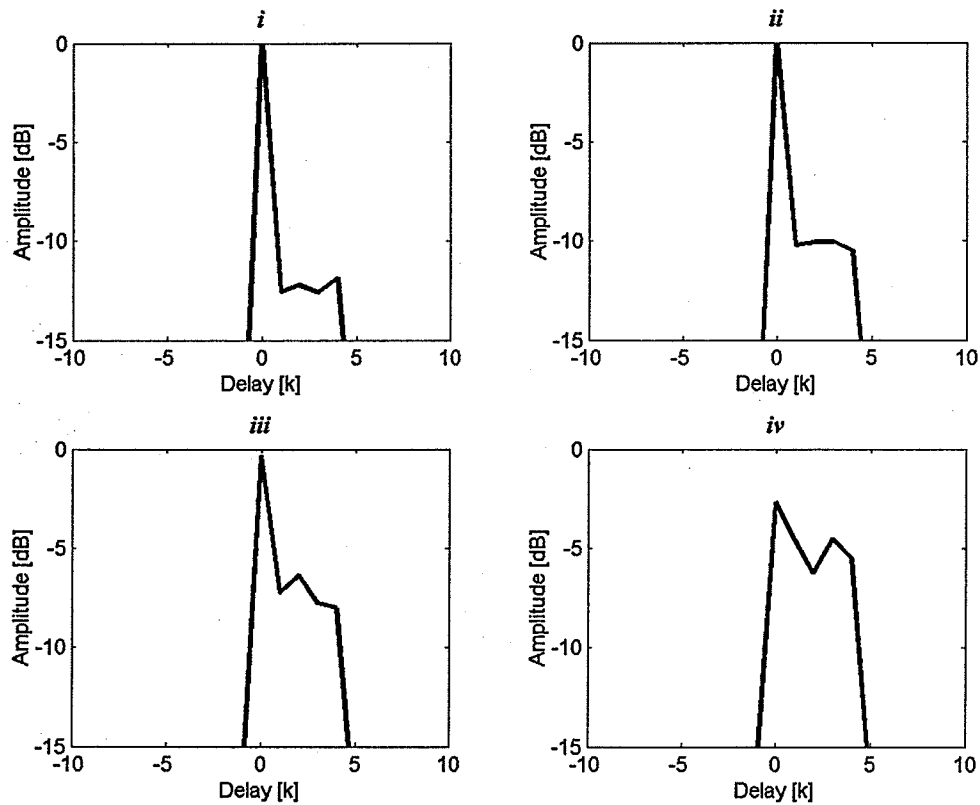


Fig. 4.5. Performance of Bernoulli CBFM in multipath environment at several direct reflection coefficients.

Averaged correlations between the transmitted and received bandlimited CBFM signal in a four paths environment with direct reflection coefficient of *i*) 1; *ii*) 0.7; *iii*) 0.5; *iv*) 0.3.

Cut-off frequencies: [0.05 0.45] of f_s .

Finally, a characterization on the effect of the bandwidth of the transmitted signal in the multipath environment was obtained simulating the transition of signals with different baseband support. The Bernoulli CBFM signals were filtered before transition over the Rician fading channel, and the received signal cross-correlated with the replica stored in the receiver. Figure 4.6 presents the results obtained by setting bandwidths of 80%, 60%, 40% and 20% of the sampling frequency.

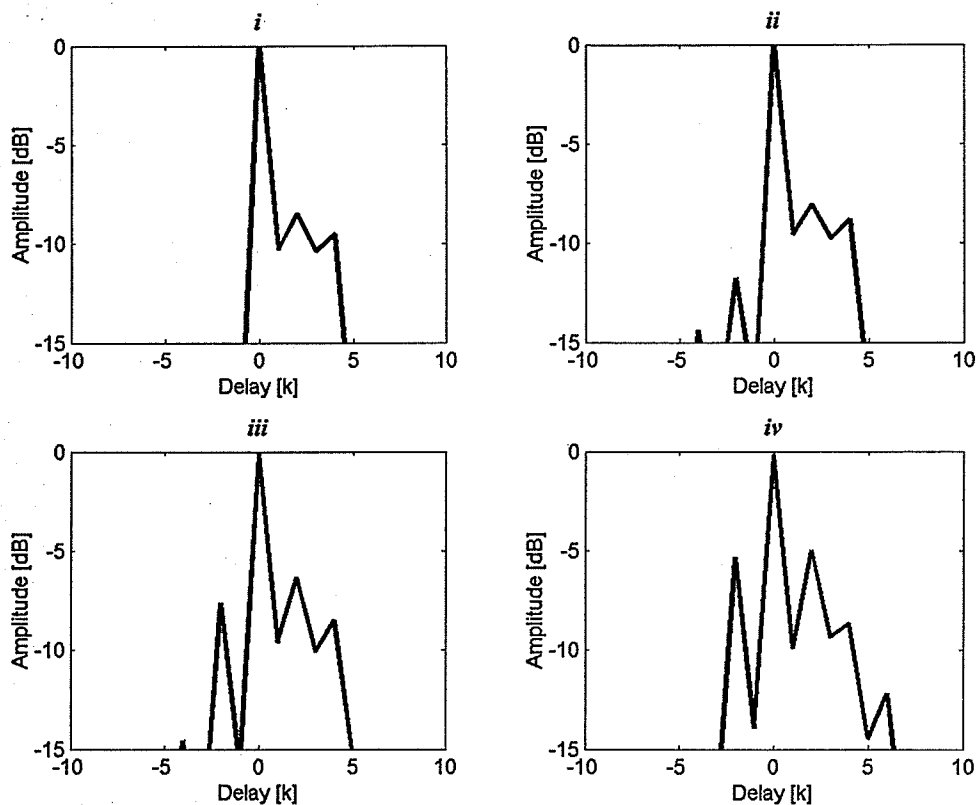


Fig. 4.6. Performance of different bandlimited Bernoulli CBFM signals in multipath environment.

Averaged correlations between transmitted and received different bandlimited CBFM signal in a four paths environment *i*) [0.05 0.45] of f_s ; *ii*) [0.10 0.40] of f_s ; *iii*) [0.15 0.35] of f_s ; *iv*) [0.20 0.30] of f_s cut-off frequencies.
Direct reflection coefficient: 0.7.

Figure 4.6 shows that the reduction of the bandwidth in the transmitted signals results in noisier and even ambiguous target detection. As the frequency content of the signal is reduced, the interaction of delayed replicas causes a stronger deformation. From the results shown in Figure 4.4 – 4.6 it is clear that the Bernoulli CBFM signal performs well over multipath environments, in the sense that the presence of the target can be detected clearly in all but the extreme cases of the figures. It is obvious that a signal with the wider frequency spectrum is preferred in a multipath environment. Optimal performance over multipath propagation will be obtained when there is a direct line of sight between the radar source and the target, and when the reflection from the targets is large compared with the indirect reflection form signals traveling different indirect paths.

4.3 ECCM and noise performance of Bernoulli CBFM

In a real life environment, radar systems must operate under non-ideal circumstances. The presence of noise contamination is a guaranteed condition that cannot be avoided, or reduced completely. In military applications, or in any other hostile environment, the radar may be even subjected to deliberate interference or jamming by the enemy. These interferences may appear as extraneous responses in the radar receiver that may resemble real targets, or even saturate a part of the radar display [42]. The purpose of jamming is to deteriorate the operation of the radar by electronic countermeasures (ECM) of confusion. A repeater jammer operates by first identifying the radar signal and successfully predicting and replicating such a signal. Any repetitive or periodic signal is especially susceptible to jamming because of its ease of identification. Thus the enemy can construct a good estimate of the parameters of the signals and use it to jam the radar with replicas [43]. Some methods used to alleviate enemy interference rely in filtering of the jamming signal or in a simple dilution of the enemy signal by increasing the transition power. However, the risk of radar jamming is always present and imposes the use of electronic counter-countermeasures (ECCM) during system design. An efficient method to combat ECM is the use of a complex radar waveform that is not easily detected and/or identified, making it impossible for the jammer to duplicate and retransmit.

The chaotic nature of the Bernoulli CBFM signal clearly suggests its good capabilities as an ECCM. Bernoulli CBFM signals appear random, their noise-like nature makes them hard to detect and predict. Even in the case the enemy is able to detect the presence of a radar signal, the characterization of the waveform is a very complex task that will require extensive recourses to be implemented in real time. The sensitive dependence to initial conditions, characteristic of chaotic systems, guarantees that any replica produced by the jammer will differ from the transmitted signal. As the original signal propagates, and even during interception by the jammer, many noise sources modify the signal. These changes, as small as they are, will lead to tremendous errors if the signal is to be reconstructed by iteration. In addition, if the initial condition used to generate the chaotic series is changed at the transmitter, every CBFM signal will be completely different to the previous one. In the case a recorded waveform is re-transmitted by the jammer, the

radar will suffer little interference, because CBFM signals with different initial condition have no correlation.

Lacking detailed information concerning the signal characteristics of the radar, the best jamming signal is white Gaussian noise covering the bandwidth of the radar receiver to be interfered. The effect is the same as an increase in the receiver noise figure. If the jammer power is sufficiently large, the entire display can be filled with noise. In real applications not only deliberate interference occurs, but also inherent natural interference caused by ambient noise and background radiation. In order to demonstrate the performance of the Bernoulli CBFM signal under intentional (ECM) or fortuitous interference, simulated echoed returns degraded by noise were generated using three different random variables distribution functions: normal, Rayleigh and uniform.

The simulations were performed for several signal-to-noise (signal-to-interference) ratios (SNR), which were calculated as the ratio between the power of the transmitted signal and the power of the interfering signal. The analysis was done by correlating the corrupted received signals with replicas of the transmitted waveform stored as reference. An example is shown in Figure 4.7. The image shows the correlation of a noise-free echo, and the effect noise causes in the correlation plot when the received signal is affected by Gaussian noise at a SNR of -10 dB.

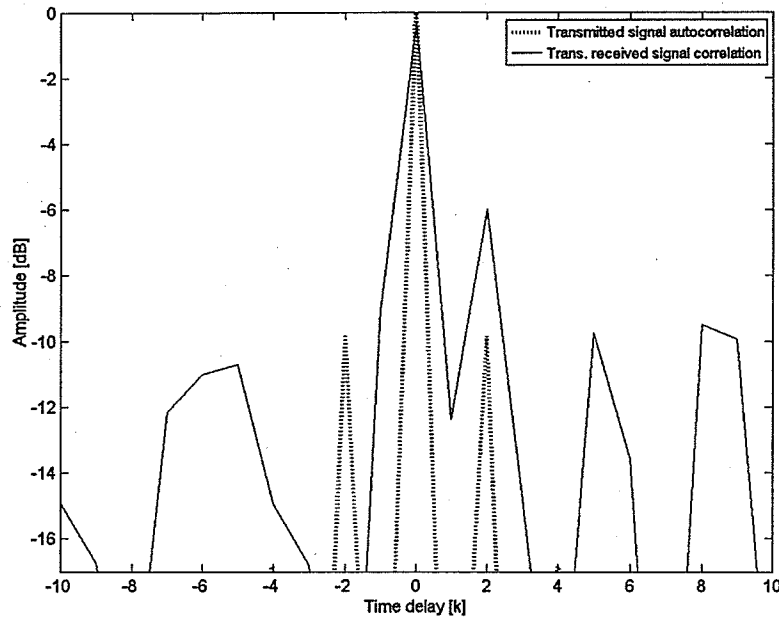


Fig. 4.7. Sample correlation between noise contaminated Bernoulli CBFM and original transmitted signal, compared with autocorrelation of the original signal.
 Simulated noise is Gaussian with a SNR of -10dB

The cross-correlation between reference and interfered signal is clearly polluted when compared with the autocorrelation obtained by processing the ideal noise-free signal. The location of the target is still determined without ambiguity, but sidelobes of considerable magnitude appear near the mainlobe. These lobes may mask weak reflections from real targets. To clarify the effect of deliberate or fortuitous interference in the imaging process, a radar image was constructed from a simulated target function. Figure 4.8 presents the comparative results of radar images generated by assembling range profiles into a two-dimensional image matrix. The figure shows the images obtained by an interference free Bernoulli CBFM waveform (Figure 4.8 *i*) and by the same signal when the interference signal has a Gaussian (Figure 4.8 *ii*), uniform (Figure 4.8 *iii*) and Rayleigh (Figure 4.8 *iv*) distribution at a -10 dB SNR. The deterioration of the images can be detected visually, however, a more objective measurement is preferred when comparing the results. To better assess the degradation of the images, the relative difference between the ideal interference-free and the received image was calculated as a percentage. The percentage was obtained by dividing the absolute differences between the received and expected images over the magnitude values of the expected or ideal

image. The pixels outside the area of the target (i. e. background clutter) were not considered for the calculation of the percentage. This percentage has not physical meaning other than a difference measurement between the images. The averaged difference percentage for fifty simulations of the Bernoulli CBFM at different SNR are shown in Table 4.1. For each simulation the initial condition for the Bernoulli CBFM was chosen randomly from a uniform distribution.

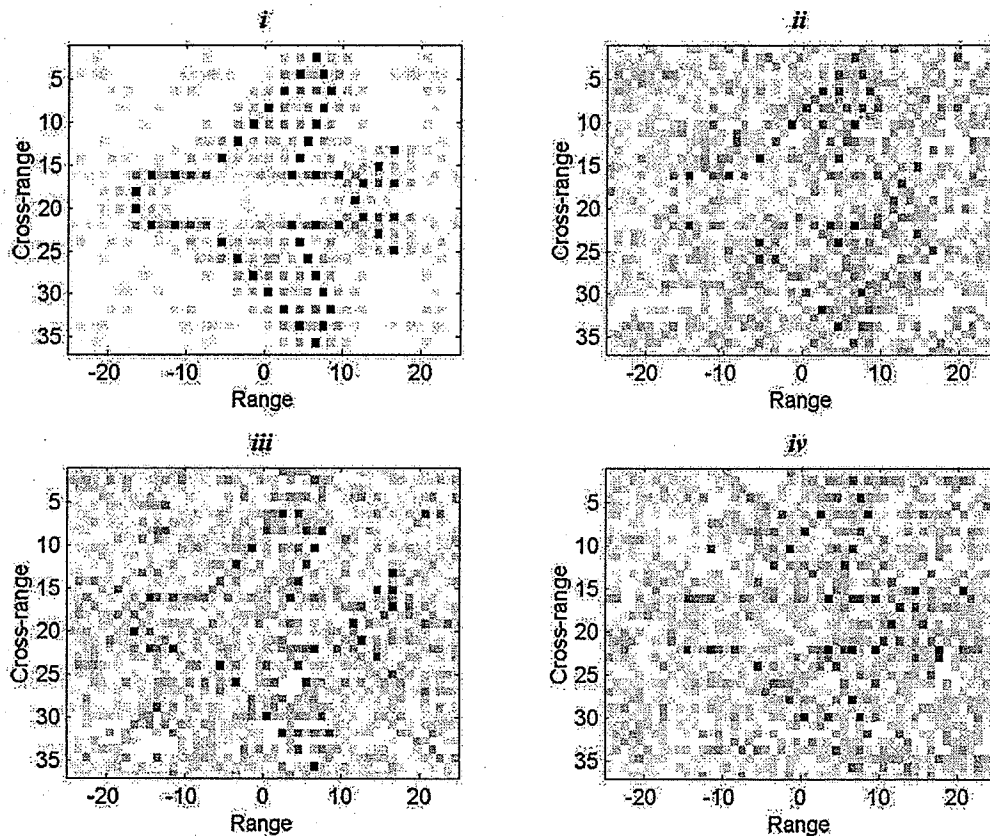


Fig. 4.8. Simulated radar images generated by ideal and noise contaminated Bernoulli CBFM signals.

- i)* Ideal noise-free image, SNR= ∞ dB; *ii)* with Gaussian interference signal, SNR= -10 dB, *iii)* with Uniform interference signal, SNR= -10 dB, *iv)* with Rayleigh interference signal, SNR= -10 dB.

TABLE 4.1
Interference induced difference percentage for various SNR and distributions in received Bernoulli CBFM signal.

SNR	Interference signal		
	Gaussian	Rayleigh	Uniform
5	14.5079	14.4081	14.3978
0	27.5045	27.3361	28.3246
-5	56.3006	57.9740	58.2528
-10	127.662	128.978	129.068
-12	191.359	188.254	182.807
-15	333.662	338.781	328.803
-20	955.445	951.473	952.651

From the percentages shown in the table, it can be inferred that the type of distribution followed by the interference signal has little effect in the final image, being the SNR the important parameter that determines the level of corruption in the image. The results for the Gaussian interference case in Table 4.1 were also plotted against the SNR in Figure 4.9. An exponential relationship between the error and the SNR was observed. Similar plots were obtained for the other two distributions. For all three cases, the target function was visually recognizable in the image when the SNR level is higher than -12 dB.

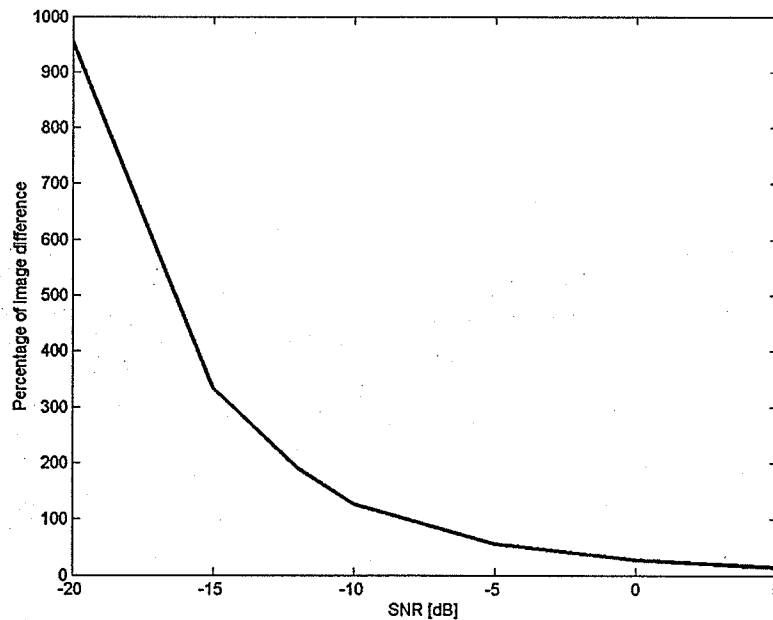


Fig. 4.9. Interference-induced difference percentage in received Bernoulli CBFM signal contaminated by Gaussian noise at various SNR.

4.4 Comparative study against FM chirp and random FM signals

The analysis, simulated experiments, and results presented in this thesis have demonstrated that the use of CBFM signals generated from Bernoulli sequences is not only viable but that it also presents desirable characteristics in terms of resolution, multipath propagation and ECCM. To further evaluate the advantages of the CBFM waveform a comparative study against commonly used linear FM (LFM) chirp and random modulated signal was performed in terms of resulting ambiguity functions, multipath propagation and interference robustness. The results obtained in this section allow better estimation of the superiority of one waveform over another, at least in the considered environments.

4.4.1 Ambiguity functions of FM chirp and random FM signal

The ambiguity function is the basic tool to evaluate and compare radar waveforms in terms of their capability to resolve target and clutter scatters in the range and velocity dimensions. The ambiguity function of a linear FM chirp described by

$$c(t) = \exp(j\alpha t^2) \text{ for } 0 < t < T, \quad (4-5)$$

is found by inserting Equation (4-5) into (2-9), which yields [17,p.35], [22]:

$$\chi(\tau, \nu) = \exp(-j\alpha\tau^2) \cdot \exp\left(-\frac{j(\nu + 2\alpha\tau) \cdot (T - |\tau|)}{2}\right) \cdot \left(\frac{2}{\nu + 2\alpha\tau}\right) \cdot \sin\left(\frac{\nu + 2\alpha\tau}{2}(T - |\tau|)\right), \quad \tau < |T|$$

$$\chi(\tau, \nu) = 0 \quad \text{elsewhere.}$$

(4-6)

The shape of the ambiguity diagram is a tilted ellipse, centered at the origin with a width of $1/\beta$ in the range plane and $1/T$ height in the Doppler axis. The general shape of the surface is shown in Figure 4.10. The narrower the width of the ambiguity function in

a given direction, the higher the accuracy and resolution of the range and Doppler measurements. The accuracy along the mayor axis of the ellipse, in a chirp ambiguity surface, is poor and can generate ambiguities along the diagonal of the delay-Doppler plane.

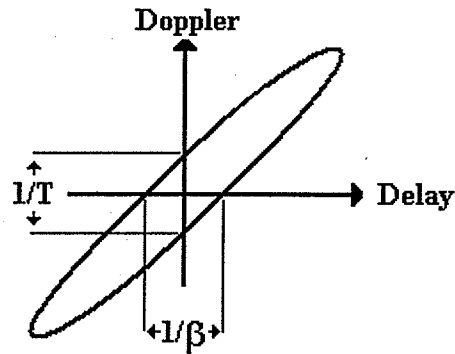


Fig. 4.10. Contour of the ambiguity surface of a linear FM chirp.

Figure 4.11 illustrates the computed surface of a LFM waveform, the image contrast the resolution and unambiguity with the one obtained by Bernoulli CBFM signals previously shown in Figure 4.2. The elliptical shape of the ambiguity surface can easily observed in the figure, notice that this shape does not guarantee the unambiguous determination of range and Doppler of two targets that lie in the diagonal of the delay-Doppler plane.

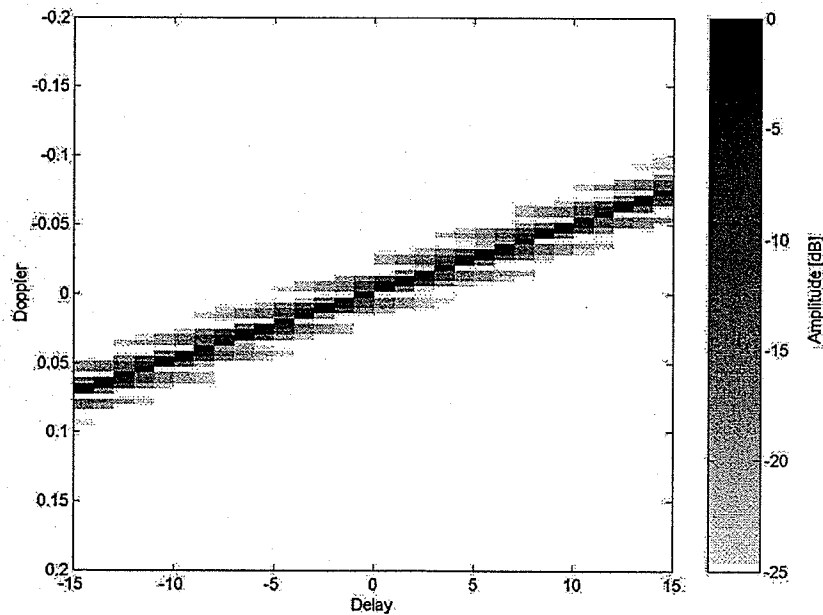


Fig. 4.11. Ambiguity surface of LFM chirp.

For comparison, the average ambiguity surface of the Bernoulli CBFM was also contrasted to that of the noise modulated Gaussian FM (GFM signal) in Figure 4.12. The ambiguity surface of the GFM signal was obtained by applying equation (4-1) for $M=100$ realizations of signals, this is the same procedure utilized when the CBFM ambiguity surface was calculated. During the generation of the GFM, the variance of the phase was set to match the power of the Bernoulli map. (With this choice, the requirement of $\sigma_x^2 < \frac{1}{2}$ is satisfied, and thus the Nyquist sampling rate obeyed) For GFM, sidelobes of the ambiguity surface along the range-delay axis fluctuated around $-10\log_{10}(N)$. The same observation applied to the Bernoulli CBFM case. Range delay resolution (defined by the -3dB points of the autocorrelation) was essentially the same for GFM and Bernoulli CBFM case, except for a wider mainlobe, result of the exponential decay of the autocorrelation function described by equation (3-28). Unlike the case of the LFM signal, the ambiguity diagram of the GFM signal allows the unambiguous determination of the target's range and velocity.

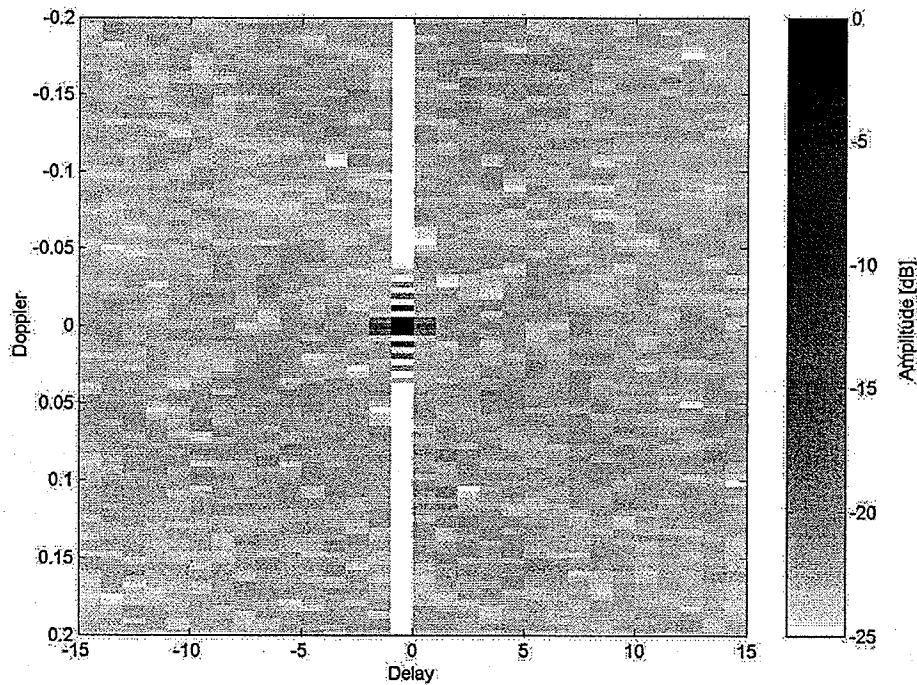


Fig. 4.12. Ambiguity surface of Gaussian FM waveform.

4.4.2 Multipath performance of linear FM chirp and noise modulated signal.

To evaluate the multipath performance of LFM and the noise modulated GFM, the simulations presented in section 4.2 were repeated for the two new signals, and the results compared to those obtained for the Bernoulli CBFM case.

Figure 4.13 presents the averaged cross-correlation function of the transmitted and received signal, when the originally transmitted signals are bandpass filtered at cut-off frequencies of 0.05 and 0.45 times the sampling frequency, and transmitted through a Rician fading channel. The figure presents the resulting averaged cross-correlations for the Bernoulli-based CBFM (denoted as BFM in the figures), the linear FM chirp signal (LFM) and the noise modulated Gaussian FM (GFM). The cross-correlation functions were obtained by first transmitting 100 different Bernoulli CBFM, LFM and GFM signals over 100 different Rician fading channels, calculating the cross-correlation with the received signals and then calculating the average of these correlations bin by bin. The cross-correlations in Figure 4.13 are shown for different length fading channels.

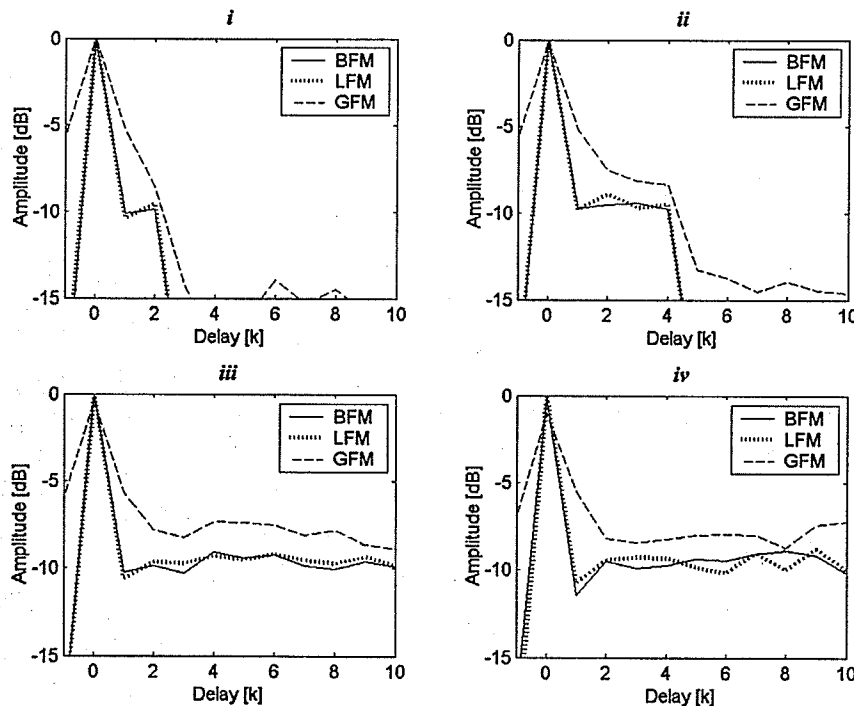


Fig. 4.13. Comparison of Bernoulli CBFM (BFM), linear FM (LFM) and Gaussian FM (GFM) performance in multipath environment. Average correlations between transmitted and received signals in a *i*) two paths; *ii*) four paths; *iii*) twelve paths; *iv*) twenty five paths scenario. Cut-off frequencies: [0.05 0.45] of f_s , Direct reflection coefficient: 0.7.

The effect caused by addition of signals traveling longer paths is clearly shown by the correlations in Figures 4.13. As for the case of the Bernoulli FM, the delayed replicas of the signal cause the correlation to present a main peak at zero delay and a relatively constant value during delay times equivalent to distinct number of paths present in the propagation environment. The results in Figure 4.13 demonstrated that Bernoulli CBFM and linear FM signals, perform equivalently and both are superior to Gaussian FM waveforms that present wider cross-correlation mainlobes and higher sidelobes.

Figure 4.14 compares the waveforms under study and present the effect the direct reflection coefficient has in a radar detector operating in a four paths environment.

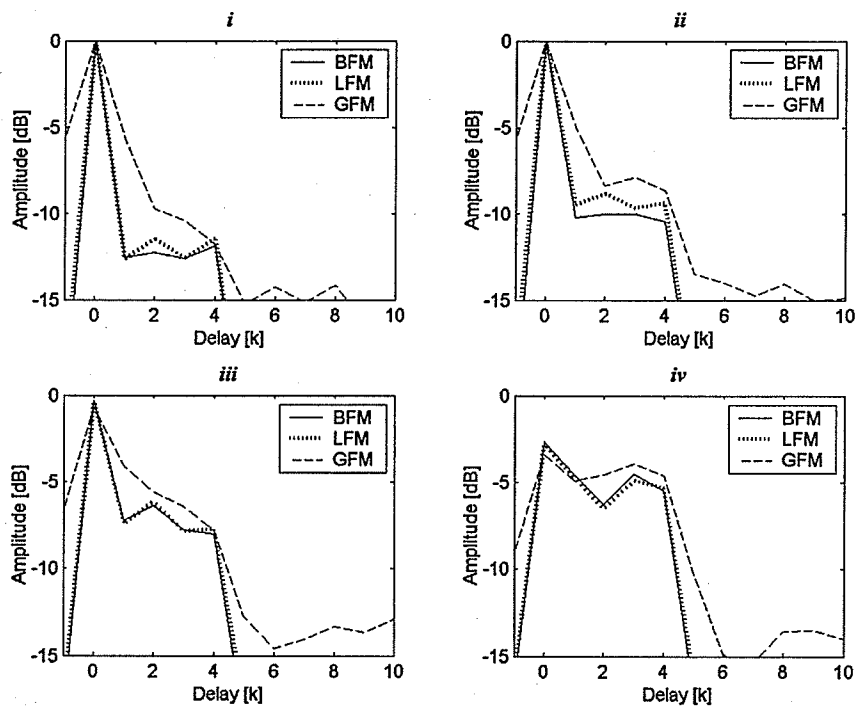


Fig. 4.14. Comparison of Bernoulli CBFM (BFM), linear FM (LFM) and Gaussian FM (GFM) performance in multipath environment with several reflection coefficients.

Average correlations between transmitted and received bandlimited signals in a four paths environment with direct reflection coefficient of *i*) 1; *ii*) 0.7; *iii*) 0.5; *iv*) 0.3. Cut-off frequencies: [0.05 0.45].

Once again, the trends observed for the Bernoulli CBFM in section 4.2, were followed by linear FM and the Gaussian FM signals. Similarly, the results obtained by linear FM signals are very close to those of the Bernoulli CBFM. The autocorrelations obtained for

the GFM case, indicate that there is a considerable interference by the superimposition of replicas of the transmitted signal traveling different paths.

Finally, the comparative results in Figure 4.15, present the effect that bandwidth reduction has on the transmitted signal operating in the multipath environment. The studied radar signals were filtered before transmission over the Rician fading channel, and the received echo cross-correlated with the replica stored in the receiver. Figure 4.15 presents the results obtained by setting bandwidths of 80%, 60%, 40% and 20% the original signal's bandwidth.

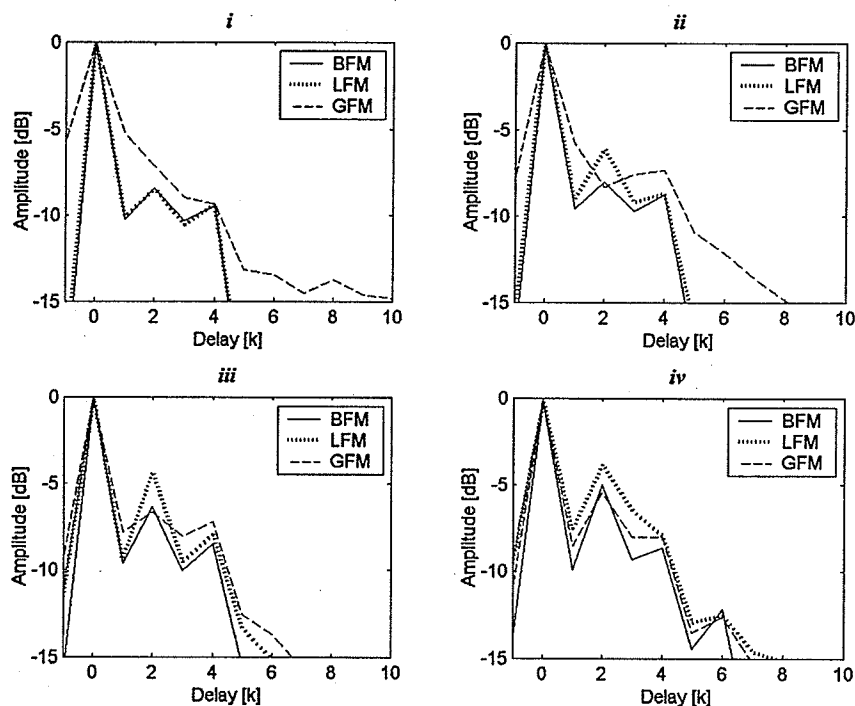


Fig. 4.15. Comparison of Bernoulli CBFM (BFM), linear FM (LFM) and Gaussian FM (GFM) performance when bandwidth is reduced.
 Averaged correlations between the transmitted and received different bandlimited signals in a four paths environment *i*) [0.05 0.45]; *ii*) [0.10 0.40]; *iii*) [0.15 0.35]; *iv*) [0.20 0.30] cut-off frequencies.
 Direct reflection coefficient: 0.7.

As the frequency content of the signal is reduced, the interaction of delayed signal replicas causes a stronger signal deformation. At the same time, as the bandwidth of the transmitted signals is reduced, the shapes of the cross-correlations approximate each other, independently of the originally transmitted signal. Indicating that a reduction of the signals bandwidth causes the performance of the Bernoulli, linear and Gaussian FM

signals to approximate. The result can be interpreted by relating the multipath performance of a signal to its bandwidth content. The Bernoulli CBFM and the linear FM signal have essentially the same frequency content (i.e. white spectrum in the filtered band), this results in similar cross-correlations in a multipath environment. When the signals are filtered around the central frequency, not only the spectrum of the Bernoulli CBFM and the linear FM remain similar, but also the spectrum of the Gaussian FM signal approximates a white spectrum in the passband. When the frequency content of the signals is reduced enough, like in the last plot of Figure 4.15, the cross-correlations, obtained by processing Bernoulli CBFM, linear FM and Gaussian FM signals, are similar. This result, however, is not desired, because the reduction of the bandwidth in the transmitted signal also deteriorates its performance in the multipath environment.

4.4.3 ECCM and noise performance of FM chirp and random FM signal

The different nature of linear and Gaussian FM signals results in different ECCM capabilities. While the inherent randomness in the noise modulated signal causes the Gaussian FM signal [44], [45] to be very hard to detect, identify and reproduce, the well defined oscillatory nature of a linearly modulated FM signal can be more easily detected and reproduced by a jammer system [43]. In terms of ECCM, the low probability of interception and identification offer the Gaussian FM, as well as the Bernoulli CBFM signal, a considerable advantage over the linear FM signal.

By considering a jammer system that attempts to interfere with the radar by transmitting a noise signal, not only the ECCM capabilities of the radar signal can be assessed, but also the effects noise produces in the signal. To characterize the effect produced by intentional or natural noise contamination in the linear FM and Gaussian FM signals, simulated echoes degraded by noise were generated using normal, Rayleigh and uniform distributions. The simulations were performed for several SNR as described in section 4.3. A radar image (illustrated in Figure 4.8 *i*) was constructed from a simulated target, the relative difference between the ideal interference-free and the received image was calculated as a percentage. The averaged difference percentage, for 50 simulations of

Bernoulli CBFM, linear FM and Gaussian FM signals at different SNR are shown in Table 4.2.

TABLE 4.2
Interference-induced difference errors for various distributions in received Bernoulli CBFM, Linear chirp FM and Gaussian FM signals.

SNR	BFM			LFM			GFM		
	Gaussian	Rayleigh	Uniform	Gaussian	Rayleigh	Uniform	Gaussian	Rayleigh	Uniform
5	14.5079	14.4081	14.3978	12.5128	12.3218	12.4817	18.7764	18.8022	18.7172
0	27.5045	27.3361	28.3246	23.8056	23.6370	23.7299	35.4122	35.5563	34.9591
-5	56.3006	57.9740	58.2528	49.3926	50.1740	50.3993	69.1281	69.7708	70.4239
-10	127.662	128.978	129.068	114.481	114.382	114.189	164.872	159.579	159.799
-12	191.359	188.254	182.807	166.492	161.701	158.691	218.446	215.166	220.677
-15	333.662	338.781	328.803	301.212	294.622	296.738	389.855	383.644	394.708
-20	955.445	951.473	952.651	857.780	862.521	832.423	1232.1	1228.4	1217.4

From the percentages shown in the table, it can be inferred that the type of distribution followed by the interference signal has little effect in the final image, being the SNR the important parameter that determines the level of corruption in the image. Figure 4.16 shows the plot of the difference percentage as a function of the SNR for the studied signals, when the interfering noise follows a Gaussian distribution. The plot reveals that the linear FM signal is less affected by interfering noise, followed by the CBFM signal; finally, the noise modulated waveform presented the maximum corruption by noise. Similar results were obtained for the other two distributions.

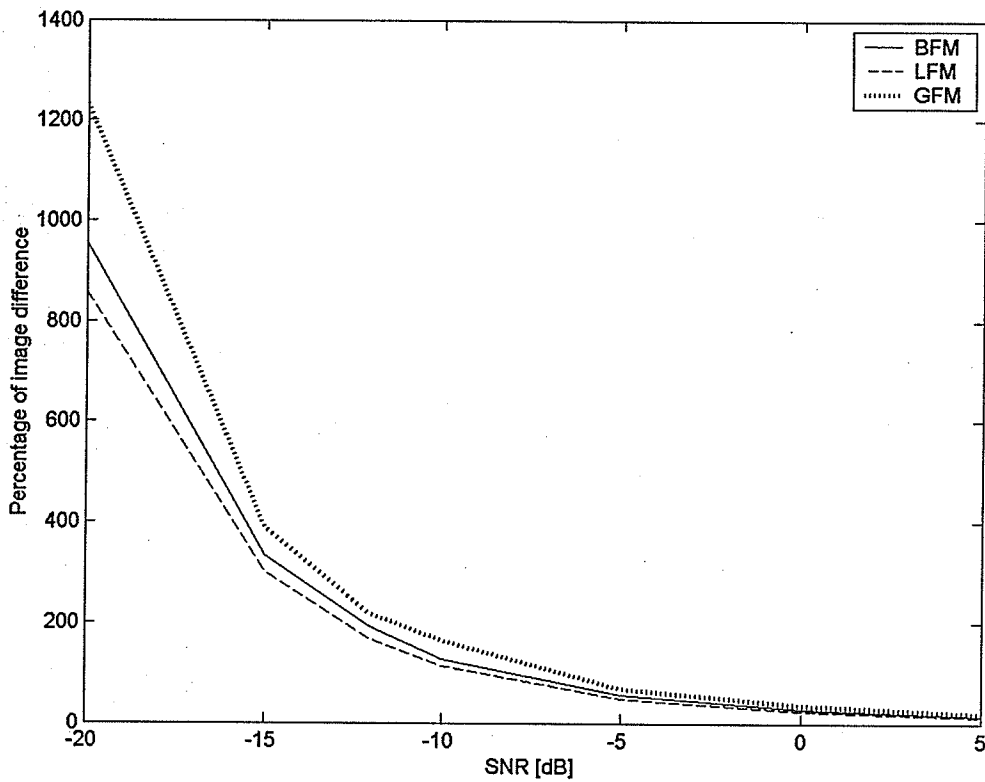


Fig. 4.16. Interference-induced difference percentage in received waveforms contaminated by Gaussian noise for various SNR.
 BFM, Bernoulli CBFM; LFM, linear FM; GFM Gaussian FM

Chapter 5

Conclusion

This thesis presented the analysis of a set of novel radar signals and investigated their favourable capabilities for high-resolution imaging. The work presented in this thesis offers a novel exploration in the area of radar signal design by utilizing the concept of chaos to improve the performance of radar systems. The main advantage of the proposed signals is that they combine the broad bandwidth of classical radar signals, required for high range resolution, with the noise-like appearance of random signals, needed for range-Doppler resolution and ECCM.

The chaotic and CBFM signals introduced in this investigation proved to be ergodic and demonstrated nearly optimal characteristics for their use in high-resolution radar. Broadband spectrums and narrow autocorrelation functions, required for high resolution ranging, were obtained for the chaotic and CBFM signal. The ambiguity surfaces of such signals resulted in thumbtack functions in the delay-Doppler plane, thus allowing unambiguous range and velocity estimation.

A comparative examination of the ambiguity surfaces showed that the Bernoulli CBFM signal outperformed the rest of the CBFM signals and that its ambiguity surface was comparable to the ones obtained from the non-modulated chaotic signals. An analysis based on the chaos detection and quantification demonstrated that the Bernoulli CBFM signal differs from the logistic, tent and quadratic CBFM cases by being the only modulated signal that preserved chaotic behaviour. The results from two chaotic metrics confirmed that the behaviour of the Bernoulli CBFM signal is unique among the four initially proposed CBFM signals.

A more detailed analysis of the Bernoulli CBFM signal revealed its satisfactory performance in multipath propagation and noise contaminated environments. The signal proved to be resistant to deterioration by additive noise and self-interference caused by delayed replicas. A comparative study demonstrated that the performance of the Bernoulli CBFM is comparable to that of the linear FM chirp, considering the two adverse environments. However, the ECCM characteristic of the Bernoulli CBFM are clearly superior to the ones obtained by an oscillatory signal like the linear FM chirp. The same study also showed that the Bernoulli CBFM signal is superior to the randomly modulated GFM signal in multipath and noise affected environments.

From the analysis and results presented in thesis, it can be said that the use of chaotic, CBFM, and specially the Bernoulli CBFM signal, is not only feasible but also advantageous in the field of high-resolution radar imaging. Further work will be required in the study of the CBFM signal and its complete characterization. The properties of the Bernoulli CBFM should be further studied and understood. The final goal of this research topic should be the complete design, implementation and final construction of a radar system based on the proposed signals.

References

- [1] M. Skolnik, *Introduction to radar systems*, New York, McGraw-Hill, 1962.
- [2] A. W. Rihaczek, *Principles of high resolution radar*, New York, McGraw-Hill, 1969.
- [3] H. Peilgen, H. Jürgen, and D. Saupe, *Chaos and fractal: New frontiers of science*, New York, Springer-Verlag, 1992.
- [4] A. Abel, W. Schwarz, M. Götz, "Noise performance of chaotic systems," *IEEE Trans. Circuits and Systems I: Fundamental Theory and Applications*, vol. 47, no. 12, pp. 1726-1732, Dec. 2000.
- [5] N. Wiener, "The homogeneous chaos," *American Journal of Mathematics*, vol. 60, no. 4, pp. 897-936, Oct. 1938.
- [6] E. N. Lorenz, "Deterministic nonperiodic flow," *Journal of Atmospheric Science*, vol. 20, pp. 130-142, 1963.
- [7] R. Hilborn, *Chaos and non-linear dynamics*, New York, Oxford University Press, 2000.

- [8] M. Delgado, A. Rodriguez, "Chaos-based noise generation in silicon," in *Chaotic Electronics in Telecommunications*, M.P. Kennedy, R. Rovatti, and G. Setti, Ed., Boca Raton, CRC Press, 2000.
- [9] R. Benjamin, *Modulation, resolution, and signal processing in radar, sonar and related systems*, London, Pergamon Press, 1966.
- [10] M. I. Sobhy, A. R. Shehata, "Chaotic radar systems," *IEEE Microwave Symposium Digest, MTT-S International*, vol. 3, pp.1701 –1704, June 2000
- [11] J. Myers and B. C. Flores, "Radar imaging via random FM correlations," *Algorithms for Synthetic Aperture Radar Imagery IV*, E. G. Zelnio, Ed., SPIE Proc. vol. 3721, pp. 130-139, 1999.
- [12] Y. Xu, R. M. Narayanan, Xiaojian Xu, J. O. Curtis, "Polarimetric processing of coherent random noise radar data for buried object detection," *IEEE Trans. Geosciences and Remote Sensing*, vol. 39, no. 3, pp. 467-478, Mar. 2001.
- [13] X. Wu, W. Liu, L. Zhao, J. Fu, "Chaotic phase code for radar pulse compression," *IEEE Proc. National Radar Conference*, pp. 279-283, 2001.
- [14] T. E. Sollenberg, "Multipath phase errors in CW-FM tracking systems," *Trans. IRE*, vol. 3, no. 4, pp 185-192, Oct. 1955.
- [15] P. M. Woodward, *Probability and information theory with applications to radar*, New York, McGraw-Hill, 1953.
- [16] J. S Son, G. Thomas, B. C. Flores, *Range-Doppler radar imaging motion compensation*, Artech House, 2001.
- [17] G. J. A. Bird, *Radar precision and resolution*, London, Pentech Press, 1974.

- [18] D. E. Vakman, *Sophisticated signals and the uncertainty principle in radar*, Springer-Verlag, New York, 1968.
- [19] B. M. Horton, "Noise-Modulated distance measuring system," *IRE Proc.*, vol. 47, no. 5, pp 133-144, May 1959.
- [20] P. M. Woodward, *Probability and information theory with applications to radar*, New York, McGraw-Hill, 1953.
- [21] T. Doka, R. Seller, I. Bozsoki, B. Farkas, E. Godor, S. Mihaly, "Role of the ambiguity function for comparing impulse and CW modulation in imaging radars," *Geosciences and Remote Sensing Symposium, IGARSS'93*, vol.1, pp. 276 -277, Aug. 1993.
- [22] A. J. Zejak, I. S. Simic, B. M. Zrnic, "Chirp radar ambiguity function shaping," *EUROCON'2001 Trends in Communications*, vol. 2, pp. 325-328, July 2001.
- [23] G. S. Gill, J. C. Huang "The ambiguity function of the step frequency radar signal processor," *CIE Proc. Radar International Conference*, pp. 375-380, Oct. 1996.
- [24] M, Dawood, R. M. Narayanan, "Ambiguity function of an ultrawideband random noise radar," *IEEE Antennas and Propagation Society International Symposium*, vol.4, pp. 2142-2145, July 2000.
- [25] J. C. Guey, M. R. Bell, "Diversity waveforms sets for delay-Doppler imaging," *IEEE Trans. Information Theory*, vol 44, no. 4, pp. 1504-1522, July 1998.
- [26] S.Ying, S. Weihua, L. Guosui, "Ambiguity function of chaotic phase modulated radar signals," *ICSP '98 Proc. Signal Processing*, 1998, vol. 2 , pp. 1574 -1577, Oct. 1998 .

- [27] J. L. McCauley, *Chaos, dynamics and fractals. An algorithmic approach to deterministic chaos*, New York, Cambridge university press, 1993.
- [28] S. N. Elaydi, *Discrete chaos*, Boca Raton, Chapman and Hall/CRC, 2000.
- [29] W. Kinsner, *Fractal and chaos engineering. Course notes*, Department of Electrical and Computer Engineering, University of Manitoba, Winnipeg, 2003.
- [30] G. P. Williams, *Chaos theory tamed*, Joseph Henry, Washington, 1997.
- [31] L. M. Berliner, "Statistics, probability, and chaos," *Statistical Science*, vol. 7, no. 1, pp. 69-90, Feb. 1992.
- [32] S. M. Kay, *Modern spectral estimation: theory and application*, New York, Prentice Hall, 1987.
- [33] S. L. Marple, *Digital spectral analysis: with applications*, New York, Prentice Hall, 1987.
- [34] A. Papoulis, *Probability, random variables, and stochastic processes*, New York, McGraw-Hill, 1984.
- [35] A. Papoulis, "Random modulation: A review," *IEEE Trans. Acoustics, Speech, and Signal Processing*, vol. 31, no. 1, pp. 96-105, Feb. 1983.
- [36] B. C. Flores, E. A. Solis, G. Thomas, "Assessment of chaotic FM signals for range-Doppler imaging," *IEE Proc. Radar, Sonar and Navigation. Special Issue in Time-Frequency Analysis for Synthetic Aperture Radar and Feature Extraction*, vol. 150, no. 4, 2003.
- [37] A. Whalen, *Detection of signals in noise*, Academic Press, 1971.

[38] N. M. Blachman, G. A. McApline, "The spectrum of a high-Index FM waveform: Woodward's theorem revisited," *IEEE Trans. Communications Technology*, vol. 17, no. 2, pp. 201-208, Apr. 1969.

[39] B. Boashash, *Time-frequency signal analysis. Methods and applications*, Melbourne, Wiley, 1992.

[40] S. Haykin, *Communications systems*, New York, John Wiley and Sons, 2001.

[41] T. S. Rappaport. *Wireless communications: Principles and practice*, New York, Prentice-Hall, 1996.

[42] L. Guosui, G. Hong, S. Wemin, Z. Jianhui, "Random radar signal- A winner in both the military and the civilian operating environments," *IEEE Trans. Aerospace and Electronic Systems*. vol. 39, no. 2, pp. 489-499, Apr. 2003.

[43] D. S. Garmatyuk, R. Narayanan, "ECCM Capabilities of an ultrawideband bandlimited random noise imaging radar," *IEEE Trans. Aerospace and Electronic Systems*. vol. 38, no. 4, pp. 1243-1255, Oct. 2002.

[44] L. Guosui, G. Hong, S. Wemin, "Development of random signal radar," *IEEE Trans. Aerospace and Electronic Systems*. vol. 35, no. 3, pp. 770-777, July 1999.

[45] L. Guosui, S. Xiangquan, L. Jinhui, Y. Guoyu, S. Yaoliang, "Design of noise FM-CW radar and its implementation," *IEE Proc.*, vol. 138, no. 5, pp. 420-426, Oct. 1991.

Appendix A

List of acronyms

AF	Ambiguity function
BFM	Bernoulli frequency modulated
CBFM	Chaotic-based frequency modulated
DFT	Discrete Fourier transform
ECCM	Electronic counter-counter-measures
ECM	Electronic counter measures
EMC	Electromagnetic compatibility
FM	Frequency modulated or frequency modulation
GFM	Gaussian-based frequency modulated
GPR	Ground penetrating radar
IF	Instantaneous frequency
LFM	Linear frequency modulated or modulation
LPI	Low probability of interception
LPId	Low probability of identification
RADAR	Radio detection and range
SLL	Sidelobe level
SNR	Signal to noise ratio
VEL	Volume element

Appendix B

List of symbols

*	Complex conjugate
O_{rms}	Root mean squared value
$\langle \rangle$	Time average
α	Slope of linear FM instantaneous frequency
β	Bandwidth
χ	Ambiguity function
Δ	Difference
ΔR	Range resolution
ε	Distance between two points in a sequence (Error)
$\delta(t)$	Dirac delta
ϕ	Phase value
η	Additive noise
λ	Wavelength
λ_1	Lyapunov exponent, first Lyapunov exponent, largest Lyapunov exponent
ν	Doppler frequency
ω	Frequency (rad/s)
ω_c	Carrier frequency (rad/s)
Θ	The Heaviside function
π	Pi number

ρ	Amplitude value of reflection coefficient
σ	Standard deviation
τ	Time delay
ξ	Angle between the ground and target
ψ	Phase value of the reflection coefficient
c	Speed of light
dB	Decibel
d_0	Initial separation between two points in a sequence
d_n	Separation between two points in a sequence at a given time
D	Control parameter in chaotic iterated maps
$E\{ \}$	Expectation operator
f	A non-linear function
f_1	Instantaneous lowest frequency
f_2	Instantaneous maximum frequency
f_c	Carrier frequency
f_s	Sampling frequency
$\tilde{h}(t)$	Complex envelope of channel impulse response
i	Index number
j	The imaginary unit.
J_0	Bessel function of the zero th order
k	Discrete delay time
K	Modulation index
m	Discrete delay time
M	Total number of signal realizations
n	Discrete time
N	Total number of samples in discrete signal
$N(t)$	Noise signal
R	Range
$r(t)$	Received radar signal
$\tilde{r}(t)$	Complex envelope of the received signal

$R(\tau)$	Correlation function
R_k	Radio of the volume element at the present scale
$\text{Re}\{\}$	Real value
$s(t)$	Transmitted radar signal
$s_M(t)$	Output of the radar receiver, cross correlation between the received and transmitted radar signals
$\tilde{s}(t)$	Complex envelope of the transmitted signal
t	Time
T_t	Time at which the target is detected
v_r	Relative velocity between the radar and the target
x_0	Initial condition
x_n	Discrete signal at present discrete time
x_{n+1}	Discrete signal at next discrete time
X	Cumulative of discrete signal

Appendix C

MATLAB© Simulations code

1.

```
%-----  
%      Chaotic sequences and CBFM signals generator  
%      Logistic, Bernulli, Tent, Quadratic,  
%-----  
% [fmlogis, fmbernu, fnten, fmqua, fmcong, fmran]=  
% Chaos(B,m,P,K) generates length m chaotic sequences and  
% FM signals using the modulation index B.  
%      Xn=cos(2*pi*B*cumsum(MAP(2:m)*Dt)+2*pi*B*MAP(1)*Dt);  
%  
% If P=1 the sequences are plotted.  
  
function [fmlogis, fmbernu, fnten, fmqua, fmran, fs]=chaos(B,m,P,K)  
  
    if m<2  
        error('The length of the sequence (m) has to be greater than  
1')  
    end  
  
    n=[0:m-1];           %Sequences length  
    logis=zeros(1,m);    %Matrix initialization  
    bernu=logis;        %Matrix initialization  
    ten=logis;          %Matrix initialization  
    qua=logis;          %Matrix initialization  
    ran=logis;  
  
%-----  
%      Logistic Map generator  
%      logis(1)=rand(1)-1/2;           %logis(0) (- [-1/2,1/2]  
for i=2:m  
    logis(i)=(4-1e-7)*((1/2)^2-logis(i-1)^2)-1/2;  
end  
%logis      (- [-1/2,1/2]  
%-----
```

```

% -----
%
%           Bernulli Map generator

bernu(1)=rand(1)-1/2;           %bernu(0) (- [-1/2,1/2]
for i=2:m
    if bernu(i-1)<0
        bernu(i)=(2-1e-9)*bernu(i-1)+1/2;
    else
        bernu(i)=(2-1e-9)*bernu(i-1)-1/2;
    end
end                               %bernu    (- [-1/2,1/2]

% -----
%
%           Tent Map generator

ten(1)=rand(1)-1/2;           %ten(0) (- [-1/2,1/2]
for i=2:m
    ten(i)=1/2-(2-1e-7)*abs(ten(i-1));
end                               %ten    (- [-1/2,1/2]

% -----
%
%           Quadratic Map generator

qua(1)=rand(1)-1/2;           %qua(0) (- [-1/2,1/2]
for i=2:m
    qua(i)=(.5-1e-7)-4*qua(i-1)^2;
end                               %qua    (- [-1/2,1/2]

% -----
%
%           Random Map generator

ran=rand(1,m)-1/2;           %ran    (- [-1/2,1/2]

% -----
%
%           Plotting the last 100 samples of the Generated Signals

% -----
%
%           FM Signals
%
%           Xn=cos(2*pi*B*cumsum(MAP(2:m)*Dt)+2*pi*B*MAP(1));
%           B= modulation index

fc=0;
fs=K*(B*(1/2)+fc);           %Sampling rate >=2*B*max(MAP)
Dt=1/fs;

fmlogis=exp(j*2*pi*B*cumsum(logis*Dt));           %Logistic FM signal
fmbernu=exp(j*2*pi*B*cumsum(bernu*Dt));           %Bernoulli FM signal
fmten=exp(j*2*pi*B*cumsum(ten*Dt));               %Tent FM signal
fmqua=exp(j*2*pi*B*cumsum(qua*Dt));               %Quadratic FM signal
fmran=exp(j*2*pi*B*cumsum(ran*Dt));               %Random FM signal

```

2.

```
% Bifurcation diagrams of the Logistic, Bernoulli, tent, quadratic
```

```
% Input: none
```

```
##### Logistic #####
```

```
figure(1)
```

```
Npre = 2000; %Preiterations(to avoid transients)
Nplot = 500; % Ploted points
Resolution=0.002; % R-Resolution
```

```
x = zeros(Nplot,1);
```

```
for r = 0:Resolution/2:4.0,
    x(1) = rand(1)-1/2;
    for n = 1:Npre,
        x(1) = r*x(1)*(1-x(1));%-x(1)^2);%-.5;
    end,
    for n = 1:Nplot-1,
        x(n+1) = r*x(n)*(1-x(n));%-x(1)^2);%-.5;
    end,
    plot(r*ones(Nplot,1), x, 'k.', 'markersize', 2);
    hold on;
end,
```

```
title('Bifurcation diagram of the logistic map');
xlabel('D','FontAngle','Italic'); ylabel('x_n');
set(gca, 'xlim', [2.5 4.0]);
hold off;
```

```
##### Bernoulli
```

```
figure(2)
```

```
x = zeros(Nplot,1);
for r = 1:Resolution:2,
    x(1) = rand(1)-.5;
    for n = 1:Npre,
        if x(1)<0
            x(1)=r*x(1)+1/2;
        else
            x(1)=r*x(1)-1/2;
        end
    end,
    for n = 1:Nplot-1,
        if x(n)<0
            x(n+1)=r*x(n)+1/2;
        else
            x(n+1)=r*x(n)-1/2;
        end
    end,
    plot(r*ones(Nplot,1), x, 'k.', 'markersize', 2);
    hold on;
```

```

end,
title('Bifurcation diagram of the Bernoulli map');
xlabel('r'); ylabel('x_n');
%set(gca, 'xlim', [1 2]);
hold off;

%%% Tent

figure(3)
x = zeros(Nplot,1);
for r = 1:Resolution:2,
    x(1) = rand(1)-.5;
    for n = 1:Npre,
        x(1)=1/2-r*abs(x(1));
    end,
    for n = 1:Nplot-1,
        x(n+1)=1/2-r*abs(x(n));
    end,
    plot(r*ones(Nplot,1), x, 'k.', 'markersize', 2);
    hold on;
end,
title('Bifurcation diagram of the tent map');
xlabel('r'); ylabel('x_n');
%set(gca, 'xlim', [1 2]);
hold off;

```

```

%%% Quadratic

```

```

figure(4)
x =zeros(Nplot,1);
for r = 0:Resolution/5:0.5,
    x(1) = rand(1)-.5;
    for n = 1:Npre,
        x(1)=r-4*x(1)^2;
    end,
    for n = 1:Nplot-1,
        x(n+1)=r-4*x(n)^2;
    end,
    plot(r*ones(Nplot,1), x, 'k.', 'markersize', 2);
    hold on;
end,
title('Bifurcation diagram of the quadratic map');
xlabel('r'); ylabel('x_n');
%set(gca, 'xlim', [1 2]);
hold off;

```

3.

```

% Chaotic signals ensemble autocorrelations

```

```

% Input: MM= number of signals
%       mm= length of the signals
%       uses maps.m to generate the chaotic signals
% Output: Plot of the ensemble and averaged signals autocorrelation

```

```

MM=50;          % Number of signals
mm=30;         % Length of signal

mlogis=zeros(MM,59);
mbernu=mlogis;
mten=mlogis;
mqua=mlogis;
msine=mlogis;

for kk=1:MM

% [fmlogis, fmbernu, fnten, fmqua]=chaosmaps(2,501+m,0);
maps

    fml=logis(501:501+mm);
    fmb=bernu(501:501+mm);
    fmt=tent(501:501+mm);
    fmq=qua(501:501+mm);
    fms=sine(501:501+mm);

    xcl=fftshift(iff(fft(fml,2*mm-1).*conj(fft(fml,2*mm-1))));
    xcb=fftshift(iff(fft(fmb,2*mm-1).*conj(fft(fmb,2*mm-1))));
    xct=fftshift(iff(fft(fmt,2*mm-1).*conj(fft(fmt,2*mm-1))));
    xcq=fftshift(iff(fft(fmq,2*mm-1).*conj(fft(fmq,2*mm-1))));
    xcs=fftshift(iff(fft(fms,2*mm-1).*conj(fft(fms,2*mm-1))));

    mlogis(kk,:)=abs(xcl)';%/max(abs(xcl));
    mbernu(kk,:)=abs(xcb)';%/max(abs(xcb));
    mten(kk,:)=abs(xct)';%/max(abs(xct));
    mqua(kk,:)=abs(xcq)';%/max(abs(xcq));
    msine(kk,:)=abs(xcs)';

end

mlogis=mean(mlogis);
mbernu=mean(mbernu);
mten=mean(mten);
mqua=mean(mqua);
msine=mean(msine);

figure(1)
subplot(221)
plot(-mm+1:mm-1,20*log10(mlogis/max(mlogis)),'k','LineWidth',2)
title('i_a','FontName','times new
roman','FontAngle','Italic','FontWeight','Bold','FontSize',12)
% xlabel('Delay')
ylabel('Amplitude [dB]')
axis([-10 10 -15 0])

subplot(222)
plot(-mm+1:mm-1,20*log10(mbernu/max(mbernu)),'k','LineWidth',2)
title('ii_a','FontName','times new
roman','FontAngle','Italic','FontWeight','Bold','FontSize',12)
xlabel('Delay')
ylabel('Amplitude [dB]')
axis([-10 10 -15 0])

```

```

figure(1)
  subplot(223)
  plot(-mm+1:mm-1,20*log10(mten/max(mten)),'k','LineWidth',2)
  title('iii_a','FontName','times new
roman','FontAngle','Italic','FontWeight','Bold','FontSize',12)
% xlabel('Delay')
  ylabel('Amplitude [dB]')
  axis([-10 10 -15 0])

```

```

  subplot(224)
  plot(-mm+1:mm-1,20*log10(mqua/max(mqua)),'k','LineWidth',2)
  title('iv_a','FontName','times new
roman','FontAngle','Italic','FontWeight','Bold','FontSize',12)
% xlabel('Delay')
  ylabel('Amplitude [dB]')
  axis([-10 10 -15 0])

```

4.

% Autocorrelation for the chaotic signals.

% Uses function chaos() to generate the signal, the signals are segmented

% and a averaged autocorrelation is obtained from the segments autocorrelations

% Output: Autocorrelation plots

```
[fmlogis, fmbernu, fmten, fmqua, fmcong, fmran, fs]=chaos(2,1500,0,2);
```

```
h=floor(length(fmlogis)/30);
```

%Number of posible averages

```
corrlogis=zeros(1,59);
```

%Correlation matrix initialization

```
corrbernus=zeros(1,59);
```

%Correlation matrix initialization

```
corrten=zeros(1,59);
```

%Correlation matrix initialization

```
corrqua=zeros(1,59);
```

%Correlation matrix initialization

```
for g=1:h
```

%For each posible average

```
  if g*30+31>length(fmlogis)
```

%For the final average of 60 ambiguity functions

```
    break
```

%End cycle

```
  end
```

```
    corrlogistempx=xcorr([zeros(1,30) (fmlogis(30*(g-1)+1:30*(g-1)+30)) zeros(1,30) ],'unbiased'); %Calculate autocorelation function of the next 30 samples (Logistic)
```

```
    corrbernutemp=xcorr([zeros(1,30) fmbernu(30*(g-1)+1:30*(g-1)+30) zeros(1,30) ],'unbiased'); %Calculate autocorelation function of the next 30 samples (Bernulli)
```

```
    corrtentemp=xcorr([zeros(1,30) fmten(30*(g-1)+1:30*(g-1)+30) zeros(1,30) ],'unbiased'); %Calculate autocorelation function of the next 30 samples (Tent)
```

```

        corrquatempxcorr([zeros(1,30) fmqua(30*(g-1)+1:30*(g-1)+30)
zeros(1,30) ], 'unbiased');          %Calculate autocorelation
function of the next 30 samples (Quadratic)

```

```

        corrlogis=corrlogis+(corrlogistemp(61:119));
%Add the new values to the previous ones
        corrbernu=corrbernu+(corrbernutemp(61:119));
%Add the new values to the previous ones
        corrtten=corrtten+(corrttentemp(61:119));
%Add the new values to the previous ones
        corrqua=corrqua+(corrquatempx(61:119));
%Add the new values to the previous ones

end
subplot(221)
plot(20*log10(abs(corrlogis)/max(abs(corrlogis))))
subplot(222)
plot(20*log10(abs(corrbernu)/max(abs(corrbernu))))
subplot(223)
plot(20*log10(abs(corrtten)/max(abs(corrtten))))
subplot(224)
plot(20*log10(abs(corrqua)/max(abs(corrqua))), 'LineWidth', 2)

```

5.

```

% Chaotic based FM signal Spectral estimation
% by autocorrelation averaging and Fourier transform

```

```

% Input: None
% Output: Plot of the signal's power spectrums

```

```

M=500;          % number of signals
m=128;          % length

```

```

for k=1:M

```

```

    [fmlogis, fmbernu, fmtten, fmqua, fmsine]=chaos(2, 501+m, 0, 2);

```

```

    fml=fmlogis(501:501+m);
    fmb=fmbernu(501:501+m);
    fmt=fmtten(501:501+m);
    fmq=fmqua(501:501+m);
    fms=fmsine(501:501+m);

```

```

    xcl=fftshift(fft(fml));
    xcb=fftshift(fft(fmb));
    xct=fftshift(fft(fmt));
    xcq=fftshift(fft(fmq));
    xcs=fftshift(fft(fms));

```

```

    logis(k, :)=abs(xcl)/max(abs(xcl));
    bernu(k, :)=abs(xcb)/max(abs(xcb));

```

```

    ten(k,:)=abs(xct);%/max(abs(xct));
    qua(k,:)=abs(xcq);%/max(abs(xcq));
    sine(k,:)=abs(xcs);%/max(abs(xcq));

end

logis=mean(logis);
bernu=mean(bernu);
ten=mean(ten);
qua=mean(qua);
sine=mean(sine);

plot(-.5:1/128:.5,20*log10(logis/max(logis)),'k','LineWidth',2)
title('i','FontName','times new
roman','FontAngle','Italic','FontWeight','Bold','FontSize',12)
xlabel('Normalized frequency')
ylabel('Amplitude [dB]')
axis([-0.5 0.5 -15 0])
set(gca,'xtick',[-.5:.2:5])
%print(1, '-djpeg', 'fig10a');close

6.

% Lyapunov exponent calculation

% Input: Input signal should be save in the variable x (as vector)
% Output: Plot of the distance Dn with respect to n (Slope
calculation)

N=30;           % Number of initial points
n=25;          % Maxim length to dispaly

i=zeros(N,n);
d=i;
i(:,1)=1+ceil(rand(1,N)*100)';

for m=1:N
    [d0,index]=min(abs([x(1:i(m,1)-2)           inf           inf           inf
x(i(m,1)+2:length(x))] - x(i(m,1))));
    j=index(1)-i(m,1);
    i(m,1:n)=i(m,1):i(m,1)+(n-1);
    d(m,:)=abs(x(i(m,:)+j)-x(i(m,:)));
    ly(m,:)=log(d(m,:));%/d(m,1) );
end

LY=sum(ly,1)/m;

range=[2:10];           % Slope calculation range
X=1:n;

a= [ones(size((range))) ; (range)]' \ (LY(range))';
% Linear regression
Y=[ones(size(X)) ; X]'*a;           % Linear fit

```

```

plot(X,LY,'ko')
title('Lyapunov exponent','FontWeight','Bold')
xlabel('Iteration number [n]')
ylabel('Log(d_n)')
axis tight % LogLog Plot

```

```

hold on
plot(X,(Y),'k:') % Fitted line
legend(['m = ',num2str(a(2))],4)
plot((range),(Y(range)),'k-')
hold off

```

7.

```

% Correlation fractal dimension calculation

```

```

% Input: Input signal should be save in the variable x (as vector)
% Output: Plot of the correlation sum CR with respect to R (Slope
calculation)

```

```

xRange=max(x)-min(x);
N=length(x);
k=0:20;
R=xRange./1.5.^k;
NiR=zeros(length(k),N);

```

```

for k=1:length(k)
    for i=1:N
        j=[1:i-1 i+1:N];
        NiR(k,i)=length(find(R(k)>=abs(x(i)-x(j))))+NiR(k,i);
    end
end

```

```

piR=NiR/(N-1);
CR=1/N*sum(piR,2);

```

```

range=[4:20]; % Slope calculation range

```

```

X=log(R); % X values for regression
a= [ones(size(X(range))) ; X(range)]' \ (log(CR(range)))';
% Linear regression
Y=[ones(size(X)) ; X]'*a; % Linear fit

```

```

loglog(R,CR,'ko')
title('Correlation Dimension D_C plot','FontWeight','Bold')
xlabel('Vel size [r_k]')
ylabel('Correlation [C_k]')
axis tight % LogLog Plot

```

```

hold on
loglog(exp(X),exp(Y),'k:') % Fitted line
legend(['m = ',num2str(1+a(2))],2)
loglog(exp(X(range)),exp(Y(range)),'k-')
hold off

```

```

8.
% Chaotic FM signals ensemble ambiguity functions

% Input: M= number of signals
%      m= length of the signals
%      K= Doppler stpes
%      uses chaos.m to generate the chaotic FM signals
% Output: The averaged signals ambiguity function in the varibales
ambi[map]
%      use plotting.m to plot

M=30;
m=128;
K=256;

[x, tau, xi]=ambi(ones(m,1), -m/2:.5:m/2, K);

mlogis=zeros(size(x));
mbernu=mlogis;
mten=mlogis;
mqua=mlogis;
msine=mlogis;
gaus=mlogis;
sigma=1/sqrt(12);

for k=1:M

    [fmlogis, fmbernu, fmten, fmqua, fmsine]=chaos(2, 501+m, 0, 2);

    fml=fmlogis(501:501+m);
    fmb=fmbernu(501:501+m);
    fmt=fmten(501:501+m);
    fmq=fmqua(501:501+m);
    fms=fmsine(501:501+m);
    fmgau=exp(j*2*pi*cumsum(sigma*randn(1,m)));

    xcl=ambi(fml', -m/2:.5:m/2, K);
    xcb=ambi(fmb', -m/2:.5:m/2, K);
    xct=ambi(fmt', -m/2:.5:m/2, K);
    xcq=ambi(fmq', -m/2:.5:m/2, K);
    xcs=ambi(fms', -m/2:.5:m/2, K);
    xgs=ambi(fmgau', -m/2:.5:m/2, K);

    mlogis=mlogis+abs(xcl)/max(max(abs(xcl)));
    mbernu=mbernu+abs(xcb)/max(max(abs(xcb)));
    mten=mten+abs(xct)/max(max(abs(xct)));
    mqua=mqua+abs(xcq)/max(max(abs(xcq)));
    msine=msine+abs(xcs)/max(max(abs(xcs)));
    gaus=gaus+abs(xgs)/max(max(abs(xgs)));

end

mlogis=(mlogis)/M;
mbernu=(mbernu)/M;
mten=(mten)/M;

```

```

mqua=(mqua)/M;
msine=(msine)/M;
gaus=gaus/M;

```

```

ambilogis=abs(mlogis).^2;
ambibernu=abs(mbernu).^2;
ambiten=abs(mten).^2;
ambiqua=abs(mqua).^2;
ambisine=abs(msine).^2;
ambigaus=abs(gaus).^2;

```

9.

```

% Multipath propagation environment

```

```

% Input: m Length of the signal, delays Number of replicas
%        coef Value of direct reflection coefficient
%        [f0 f1] Cut off frequencies
%        M Number of realization
% Output: Plot of the cross correlation function

```

```

function [] = multipath(m,delays,coef,f0,f1,M)

```

```

    for (k=1:M),

```

```

        [fmlogis, fmbernu, fmten, fmqua, fmran, fs]=chaos(2,m,0,2);
        n=1:m;

```

```

        beta = (f1-f0).*(m.^(-1));
        ch = exp(j*2*pi * ( beta./(2).*(n.^2)) + f0.*n );    %Chirp
                    generation

```

```

        [B,A]=cheby2(6,20,[f0 f1]+.5);                %Bandpass filter
        [H,F]=freqz(B,A,'twosided');

```

```

        filfm=filter(B,A,fmbernu);
        filch=filter(B,A,ch);
        filran=filter(B,A,fmran);                    %Filtered signals

```

```

        h=[coef normrnd(0,1,1,delays)/5+j*normrnd(0,1,1,delays)/5];
                    %Rician channel

```

```

        X=conv(filfm,h)/2;
        X(m+1:end)=[];
        Y=conv(filch,h)/2;
        Y(m+1:end)=[];
        Z=conv(filran,h)/2;
        Z(m+1:end)=[];                                %recieved signals

```

```

        autofm=abs(xcorr(X,filfm));
        %ifft(conj(fft(filfm)).*fft(X));
        autoch=abs(xcorr(Y,filch));
        autoran=abs(xcorr(Z,filran));                % Signals

```

crosscorrelations

```
fm(k,:)=20*log10(autofm/max(autofm));
chi(k,:)=20*log10(autoch/max(autoch));
rando(k,:)=20*log10(autoran/max(autoran));      % Correlation
                                                absolute value
```

end

```
plot(-length(X)+1:length(X)-1,mean(fm,1),'k')
hold on
plot(-length(Y)+1:length(Y)-1,mean(chi,1),':k','Linewidth',2)
plot(-length(Z)+1:length(Z)-1,mean(rando,1),'--k')
legend('BFM','LFM','GFM',1)
axis([-1 10 -15 0])
xlabel('Delay [k]')
ylabel('Amplitude [dB]')
hold off
```

return

10.

% Noisy propagation environment

```
% Input: m Length of the signal, SNR Signal to noise ratio
%         [f0 f1]      Cut off frequencies
%         M Number of realization
% Output: Difference percentage in image
```

```
function [fm] = noisy(m,SNR,f0,f1,M)
```

```
for (k=1:M),
```

```
    [fmlogis, fmbernu, fnten, fmqua, fmran, fs]=chaos(2,m,0,2);
    n=1:m;
```

```
    beta = (f1-f0).*(m.^(-1));
    ch = exp(j*2*pi * ( beta./(2).*(n.^2)) + f0.*n )); %Chirp
                                                    generation
```

```
    [B,A]=cheby2(6,20,[f0 f1]+.5);
    [H,F]=freqz(B,A,'twosided'); %Bandpass filter
```

```
    filfm=real(filter(B,A,fmbernu));
    filch=real(filter(B,A,ch));
    filran=real(filter(B,A,fmran)); %Filtered signals
```

```
    noisyfm1=awgn(filfm,SNR,'measured'); %Gaussian
    noisyfm2=adduniform(filfm,SNR); %Uniform
    noisyfm3=addrayl(filfm,SNR); %and Rayleigh
    addition to CBFM
```

```

noisych1=awgn(filch,SNR,'measured');           %Gaussian
noisych2=adduniform(filch,SNR);               %Uniform
noisych3=addrayl(filch,SNR);                 %and Rayleigh
                                              addition LFM

noisyran1=awgn(filran,SNR,'measured');       %Gaussian
noisyran2=adduniform(filran,SNR);           %Uniform
noisyran3=addrayl(filran,SNR);             %and Rayleigh
                                              addition GFM

autofm=abs(xcorr(filfm))/max(abs(xcorr(filfm)));
autoch=abs(xcorr(filch))/max(abs(xcorr(filch)));
autoran=abs(xcorr(filran))/max(abs(xcorr(filran)));
%Signals autocorrelations

autofm1=abs(xcorr(filfm,noisyfm1))/max(abs(xcorr(filfm)));
autofm2=abs(xcorr(filfm,noisyfm2))/max(abs(xcorr(filfm)));
autofm3=abs(xcorr(filfm,noisyfm3))/max(abs(xcorr(filfm)));
%CBFM xcorrelations

autoch1=abs(xcorr(filch,noisych1))/max(abs(xcorr(filch)));
autoch2=abs(xcorr(filch,noisych2))/max(abs(xcorr(filch)));
autoch3=abs(xcorr(filch,noisych3))/max(abs(xcorr(filch)));
%LFM xcorrelations

autoran1=abs(xcorr(filran,noisyran1))/max(abs(xcorr(filran)));
autoran2=abs(xcorr(filran,noisyran2))/max(abs(xcorr(filran)));
autoran3=abs(xcorr(filran,noisyran3))/max(abs(xcorr(filran)));
%GFM xcorrelations

fm1(k,:)=sum(abs(autofm1(190:210)-autofm(190:210)))/sum(autofm);
fm2(k,:)=sum(abs(autofm2(190:210)-autofm(190:210)))/sum(autofm);
fm3(k,:)=sum(abs(autofm3(190:210)-autofm(190:210)))/sum(autofm);

%CBFM diff. percentage

ch1(k,:)=sum(abs(autoch1(190:210)-autoch(190:210)))/sum(autoch);
ch2(k,:)=sum(abs(autoch2(190:210)-autoch(190:210)))/sum(autoch);
ch3(k,:)=sum(abs(autoch3(190:210)-autoch(190:210)))/sum(autoch);

%LFM diff. percentage

ran1(k,:)=sum(abs(autoran1(190:210)-
autoran(190:210)))/sum(autoran);
ran2(k,:)=sum(abs(autoran2(190:210)-
autoran(190:210)))/sum(autoran);
ran3(k,:)=sum(abs(autoran3(190:210)-
autoran(190:210)))/sum(autoran);

%GFM diff. percentage

end

```